

Important Notice

This copy may be used only for the purposes of research and private study, and any use of the copy for a purpose other than research or private study may require the authorization of the copyright owner of the work in question. Responsibility regarding questions of copyright that may arise in the use of this copy is assumed by the recipient.

MODAL SEPARATION, MAPPING AND INVERTING THREE-COMPONENT VSP DATA

by

Stéphane Labonté

M.Sc. Thesis
The University of Calgary
Department of Geology and Geophysics
February, 1990



Consortium for Research in Elastic Wave Exploration Seismology

THE UNIVERSITY OF CALGARY

**MODAL SEPARATION, MAPPING, AND INVERTING THREE-
COMPONENT VSP DATA**

by

Stéphane Labonté

A THESIS

SUBMITTED TO THE FACULTY OF GRADUATE STUDIES
IN PARTIAL FULFILLMENT OF THE REQUIREMENTS FOR THE
DEGREE OF MASTER OF SCIENCE

DEPARTMENT OF GEOLOGY AND GEOPHYSICS

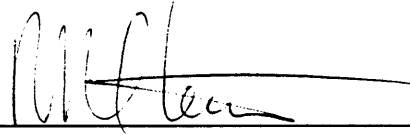
CALGARY, ALBERTA
FEBRUARY, 1990

© Stéphane Labonté 1990

THE UNIVERSITY OF CALGARY

FACULTY OF GRADUATE STUDIES

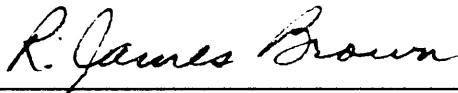
The undersigned certify that they have read, and recommend to the Faculty of Graduate Studies for acceptance, a thesis entitled "Modal separation, mapping, and inverting three-component VSP data" submitted by Stéphane Labonté in partial fulfillment of the requirements for the degree of Master of Science.



Supervisor, Dr. R. R. Stewart,
Department of Geology and Geophysics



Dr. D. C. Lawton,
Department of Geology and Geophysics



Dr. R. J. Brown,
Department of Geology and Geophysics



Dr. R. M. Rangayyan
Department of Electrical Engineering

Date: December 19, 1989

Abstract

In offset vertical seismic profiling (VSP), the large variation in angles of incidence at the geophone's location and the presence of considerable amounts of compressional (P) and shear (S) waves in the propagating wavefield necessitate the use of three-component geophones for full wavefield understanding. In this study, the vertical and radial components are used to recover the full amplitudes of P and vertical-shear (SV) waves, to map the P and SV waves to their respective reflection points, and to perform a reflectivity inversion on the converted-wave map in an attempt to recover shear-wave velocity information. Algorithms are derived and applied to two different data sets; a synthetic data set and a real three-component data set from the Rolling Hills area of southern Alberta, Canada. First the data are prepared for modal separation by applying a series of processes including rotation of horizontal components, trace equalization, downgoing wavefield removal, deconvolution and time-variant gain.

For the separation of P and S waves, filter coefficients are derived by considering the particle displacement of downgoing P and SV waves at the geophone's location. The separation process requires an estimate of P and S velocities along the borehole and uses several other simplifying assumptions. The filter coefficients are not all stable for vertical slownesses larger than $1/V_s$ and are tapered to zero by a cosine function to account for this instability. The filtering process is attempted in the f-k and localized p-t domains, and the results obtained through each method are compared. It is found that the results obtained through the p-t decomposition method do not contain the 'ringing' and the smearing of the wavelet in time and in depth that result when the f-k transform is used as a means of slowness decomposition.

The total P- and SV-wave sections are then used to map the upgoing wavefields to their respective reflection points. The synthetic results show that the mapping algorithms map the P or SV reflections within 7% of their correct offset locations and within 4% of their correct time position. The SV-wave map of the synthetic data is used to test a velocity inversion algorithm that attempts to recover the S-wave velocities from the mapped traces. The inversion is found to give results that are within 1% of the actual velocities for the synthetic data case. For the real VSP data case, however, the inversion must be given constraints to perform adequately. The wavelet effect, caused by input data that is not spiked appropriately, is present in the inversion results of both the synthetic and the real data sets.

Acknowledgements

I would like to acknowledge a few people that have made a difference in the realization of this work. Mr. Malcolm Bertram has played a major role in assisting me with the Perkin-Elmer operating system; his help, patience, impatience, sense of humor and cynicism were well appreciated. Many thanks to Dr. Scott Cheadle who agreed to let me use his p-t decomposition algorithm and helped me adapt it to the VSP case. Acknowledgements also go to my thesis supervisor, Dr. Robert Stewart, who has been supportive throughout the two years. His many thought-provoking arguments have helped me extend my understanding of geophysics.

Mr. Richard Spiteri has helped 'working out' the details of living in Geology and Geophysics. Warm thoughts coming from Silvia were always present even when needed. And last but not least, words can never hope to depict the now twenty odd years of positive influence that my parents, Yves and Mariette Labonté, have had on me. Their support, care and assistance, both physical and moral, was always well beyond the call of duty. Many more outstanding and successful endeavors remain to be accomplished on their behalf before I can ever hope to return even a fraction of what they have given.

Table of Contents

Abstract.....	iii
Acknowledgements	iv
Table of Contents.....	v
List of Tables	vii
List of Figures	viii
Chapter 1 - Introduction	1
1.1 Definitions.....	1
1.2 The need for three-component recording in VSP	2
1.3 Thesis objective.....	3
1.4 Data sets used in the thesis	3
1.4.1 Synthetic VSP	3
1.4.2 Field VSP	5
1.5 Hardware and software used.....	6
Chapter 2 - Three-component VSP Processing.....	7
2.1 Introduction	7
2.2 Rotation of horizontal components	7
2.2.1 Theory	9
2.2.2 Rolling Hills application.....	10
2.3 Trace equalization on first breaks.....	10
2.4 The p-t decomposition	16
2.4.1 Theory	16
2.4.2 Semblance weighting	19
2.5 Downgoing wavefield removal	20
2.5.1 Synthetic case.....	22
2.5.2 Rolling Hills case.....	29
2.6 Velocity analysis.....	32
2.8 Time-variant exponential gain.....	35
Chapter 3 - P-S wave mode separation	37
3.1 Introduction	37
3.2 Theory	37
3.3 Filter coefficients	40
3.3.1 Raw filter coefficients.....	40
3.3.2 Instabilities.....	43
3.3.3 Tapered filter coefficients.....	43

3.3.4	Polarity consideration.....	46
3.4	Assumptions	47
3.5	Generalized application possibilities.....	48
3.5.1	Application in the z-t domain.....	49
3.5.2	Application in the τ -p domain.....	49
3.5.3	Application in the f-k domain	51
3.5.4	Application in the f-p domain	52
3.6	Application in the p-t domain.....	53
3.6.1	Synthetic application	54
3.6.2	Rolling Hills application.....	58
3.7	Application in the f-k domain	59
3.7.1	Synthetic application	60
3.7.2	Rolling Hills application.....	61
3.8	Discussion.....	63
Chapter 4 -	Subsurface mapping of VSP data	65
4.1	P-P wave case.....	65
4.2	P-SV wave case.....	69
4.3	Discussion.....	78
Chapter 5 -	Reflectivity inversion of P-SV converted waves	83
Chapter 6 -	Conclusions.....	90
Chapter 7 -	Future work.....	92
References.....		93

List of Tables

Table 4.1	Values of the true reflection point offsets as calculated by the ray-tracing program and the center of mapped bin location obtained by inspection of the synthetic maps for each of the P-P and P-SV reflections. The reflector identifiers are as in Figures 4.7 and 4.8.....	81
Table 4.2	Values of the arrival times for the three reflectors of the synthetic data as observed on the P-P and P-SV maps of the synthetic data. The reflector identifiers are as in Figures 4.7 and 4.8. Note that the P-SV reflections were mapped to two-way normal incidence P-wave times.	81

List of Figures

Figure 1.1	Offset VSP geometry.	2
Figure 1.2	Flow chart of the processes implemented in the thesis. The sections in parentheses indicate where the processes are discussed in the thesis.....	4
Figure 1.3	Synthetic model used throughout the thesis.....	5
Figure 2.1	VSP geometry exemplifying the downhole geophone orientation problem. The large arrows point to the two small inset which are enlarged views of the two depth levels (modified from DiSiena et al., 1984).....	8
Figure 2.2	Geophone orientation before (x - y) and after (x' - y') the removal of the random orientation problem.....	8
Figure 2.3	Raw vertical component of Rolling Hills data set plotted with Automatic Gain Control (AGC) using a window length of 0.3 s.....	11
Figure 2.4	Raw horizontal component (X) of Rolling Hills data set plotted with an AGC window length of 0.3 s.	11
Figure 2.5	Raw horizontal component (Y) of Rolling Hills data set plotted with an AGC window length of 0.3 s.	12
Figure 2.6	Raw radial component of Rolling Hills data set plotted with an AGC window length of 0.3 s.....	12
Figure 2.7	Raw transverse component of Rolling Hills data set plotted with an AGC window length of 0.3 s.....	13
Figure 2.8	Raw vertical component of Rolling Hills data set plotted as true relative amplitudes.....	14
Figure 2.9	Raw radial component of Rolling Hills data set plotted as true relative amplitudes.....	14

Figure 2.10	Trace-equalized vertical component of Rolling Hills data set plotted as true relative amplitudes.	15
Figure 2.11	Trace-equalized radial component of Rolling Hills data set plotted as true relative amplitudes.	15
Figure 2.12	Raw vertical component of synthetic data set.	18
Figure 2.13	p-t decomposition of the 9-trace local window centered on the 980-meter trace for the vertical component of the synthetic data.	18
Figure 2.14	VSP section reconstructed from stacking the raw decompositions across the range of all slownesses for each 9-trace local window of the raw vertical component of the synthetic data set.....	19
Figure 2.15	Semblance-weighted p-t decomposition of the 9-trace local window centered on the 980-meter trace for the vertical component of the synthetic data.....	21
Figure 2.16	VSP section reconstructed from stacking the semblance-weighted decompositions across the range of all slownesses for each local window of the raw vertical component of the synthetic data set.....	21
Figure 2.17	Raw vertical component of synthetic data set.	22
Figure 2.18	Raw radial component of synthetic data set.	23
Figure 2.19	Vertical component of synthetic data set with first breaks muted.....	23
Figure 2.20	Radial component of synthetic data set with first breaks muted.	24
Figure 2.21	Notation for possible reflection/transmission coefficients at a welded interface between two different solid half-spaces. Short arrows show the direction of particle motion . The arrows only show the general particle motion of the reflected/transmitted wavefield, i.e. P versus S waves (after Aki and Richards, 1980).	25
Figure 2.22	Amplitude (a) and phase advance (b) of P-P and P-SV reflection coefficients plotted as a function of angle of incidence of an	

	incoming P wave. The parameters used in generating the plot are $\alpha_1 = 4000$ m/s, $\beta_1 = 2500$ m/s, $\rho_1 = 2200$ kg/m ³ , $\alpha_2 = 4300$ m/s, $\beta_2 = 2700$ m/s, $\rho_2 = 2200$ kg/m ³ . The converted wave reflection angles corresponding to the P-wave incidence angles are also shown on the top horizontal axis.....	26
Figure 2.23	Amplitude (a) and phase advance (b) of P-P and P-SV reflection coefficients plotted as a function of angle of incidence of an incoming P wave. The parameters used in generating the plot are $\alpha_1 = 4300$ m/s, $\beta_1 = 2700$ m/s, $\rho_1 = 2200$ kg/m ³ , $\alpha_2 = 4000$ m/s, $\beta_2 = 2500$ m/s, $\rho_2 = 2200$ kg/m ³ . The converted wave reflection angles corresponding to the P-wave incidence angles are also shown on the top horizontal axis.....	27
Figure 2.24	Geometry of synthetic model for P-P reflections at the 1400 m interface.....	28
Figure 2.25	Vertical component of the downgoing wavefield for the Rolling Hills data set obtained through the p-t decomposition method.....	30
Figure 2.26	Radial component of the downgoing wavefield for the Rolling Hills data set obtained through the p-t decomposition method.	30
Figure 2.27	Vertical component of the upgoing wavefield for the Rolling Hills data set obtained by subtracting the downgoing wavefield in Figure 2.25 from the total wavefield on Figure 2.10.....	31
Figure 2.28	Radial component of the upgoing wavefield for the Rolling Hills data set obtained by subtracting the downgoing wavefield in Figure 2.26 from the total wavefield on Figure 2.11.....	31
Figure 2.29	Interval velocities obtained from logs and through least-square inversions on the first P and S downgoing events on the Rolling Hills data set. Formations and lithologies are noted (from Geis et al., 1989).....	32
Figure 2.30	Deconvolved vertical component of the upgoing wavefield for the Rolling Hills data set.....	34

Figure 2.31	Deconvolved radial component of the upgoing wavefield for the Rolling Hills data set.....	34
Figure 2.32	Deconvolved vertical component for the Rolling Hills data set (Figure 2.30) with time-variant gain applied.....	36
Figure 2.33	Deconvolved radial component for the Rolling Hills data set (Figure 2.31) with time-variant gain applied.	36
Figure 3.1	Particle displacement of an incident P or S wave (after Dankbaar, 1987).....	37
Figure 3.2	Plane wave incident upon a borehole.	38
Figure 3.3	Filter coefficient for pass-P mode, vertical component.	41
Figure 3.4	Filter coefficient for pass-P mode, radial component.	41
Figure 3.5	Filter coefficient for pass-S mode, vertical component.	42
Figure 3.6	Filter coefficient for pass-S mode, radial component.	42
Figure 3.7	Tapered filter coefficient for pass-P mode, vertical component.....	44
Figure 3.8	Tapered filter coefficient for pass-P mode, radial component.....	44
Figure 3.9	Tapered filter coefficient for pass-S mode, vertical component.....	45
Figure 3.10	Tapered filter coefficient for pass-S mode, radial component.....	45
Figure 3.11	Raw p-t decomposition of the 9-trace local window centered on the 980-meter trace of the vertical component of the upgoing wavefield for the synthetic data set shown in Figure 2.19.....	54
Figure 3.12	Raw p-t decomposition of the 9-trace local window centered on the 980-meter trace of the radial component of the upgoing wavefield for the synthetic data set shown in Figure 2.20.....	55

Figure 3.13	Semblance-weighted p-t decomposition of the 9-trace local window centered on the 980-meter trace of the vertical component of the upgoing wavefield for the synthetic data set shown in Figure 2.19.....	55
Figure 3.14	Semblance-weighted p-t decomposition of the 9-trace local window centered on the 980-meter trace of the radial component of the upgoing wavefield for the synthetic data set shown in Figure 2.20.....	56
Figure 3.15	Pass-P wavefield for the synthetic data set.....	57
Figure 3.16	Pass-S wavefield for the synthetic data set.....	57
Figure 3.17	Pass-P wavefield for the Rolling Hills data set.....	58
Figure 3.18	Pass-S wavefield for the Rolling Hills data set.....	59
Figure 3.19	Pass-P wavefield for the synthetic data set obtained through the application of the P-S separation process in the f-k domain.....	60
Figure 3.20	Pass-S wavefield for the synthetic data set obtained through the application of the P-S separation process in the f-k domain.....	61
Figure 3.21	Pass-P wavefield for the Rolling Hills data set obtained through the application of the P-S separation process in the f-k domain.....	62
Figure 3.22	Pass-S wavefield for the Rolling Hills data set obtained through the application of the P-S separation process in the f-k domain.....	62
Figure 4.1	VSP ray geometry for a flat multilayered medium.....	66
Figure 4.2	P-wave CRP map for the synthetic data.....	70
Figure 4.3	P-wave CRP map for the Rolling Hills data.....	71
Figure 4.4	VSP ray geometry for P-SV reflections in a flat multilayered medium.....	72
Figure 4.5	Converted SV-wave CCP map for the synthetic data.....	76
Figure 4.6	Converted SV-wave CCP map for the Rolling Hills data.....	77

Figure 4.7	Mapped region (shaded area) for P-P reflections of the synthetic as calculated by the ray tracer. The points 1a, 1b, 2a, 2b, 3a and 3b point to the outer limits of the mapped area at the three reflectors' depths.....	79
Figure 4.8	Mapped region (shaded area) for P-SV reflections of the synthetic as calculated by the ray tracer. The points 1a, 1b, 2a, 2b, 3a and 3b point to the outer limits of the mapped area at the three reflectors' depths.....	80
Figure 5.1	Converted wave reflectivity geometry.	83
Figure 5.2	Traces belonging to the 240 to 360 m range of the P-SV map of the synthetic data of Figure 4.5 inverted using equation 5.13.....	88
Figure 5.3	(a) Integrated S-wave velocity from Geis et al. (1989). (b) 0/0 - 10/15 Hz trapezoidal bandpass filtered version of (a). (c) 45 to 90 m offset traces from the P-SV map of Figure 4.6 inverted using equation 5.13. (d) Final inverted traces obtained by adding (b) with a 10/15 - 60/75 Hz trapezoidal bandpass filtered version of (c).	89

Chapter 1 - Introduction

1.1 Definitions

Vertical seismic profiling (VSP) is an in-situ seismic wave measurement method which records seismic waves in a borehole (Balch et al., 1982; Gal'perin, 1974; Hardage, 1985; Oristaglio, 1985; Toksöz and Stewart, 1984). A geophone is usually lowered to the bottom of the borehole and a source is excited (shot) at the surface, a certain distance (offset) away from the borehole. Several shots are often repeated for a given depth level and then stacked together to produce one seismic trace. This process is repeated as the geophone is moved up the hole. The resulting VSP section consists of a group of traces recorded in time, each trace having been recorded at a different depth in the borehole.

Both downgoing and upgoing waves are present in a VSP section; this is in contrast with the surface seismic case where the geophones are located at the surface and only upgoing waves, surface waves and direct body waves can be recorded. The downgoing waves have a positive slope on the VSP section, that is, as the depth of the geophone increases, the time of arrival of a given downgoing wave also increases. On the other hand, the upgoing waves which have been reflected from geological interfaces below the depth of the geophone have a negative slope on the VSP section; their arrival time decreases as the depth of the geophone increases.

Generally, three-component geophones have been used in VSP recording. Three-component geophones record displacement along three orthogonal axes, one vertical (conventional) and two horizontal. Three-component recording has been initiated to improve conventional compressional (P) wave sections and to make an attempt at extracting and using the conventionally ignored shear (S) waves. Since the advent of three-component recording, mode-converted (P-S) waves have been observed in many offset VSP surveys (Toksöz and Stewart, 1984; Dankbaar, 1987). In this context, a P-S mode-converted wave is a P wave that converts to an S wave either at a geological interface in the downgoing mode or at the reflection point in the upgoing mode. When such a conversion occurs, the S wave that is generated is polarized in the plane that contains the P-wave propagation vector - the sagittal plane (Aki and Richards, 1980). In the case of a homogeneous, isotropic, flat-layered earth, the P-S converted wave is polarized in the vertical source-receiver plane, hence the name P-SV wave. In contrast, an S wave that is polarized perpendicular to the sagittal plane is called an SH wave.

1.2 The need for three-component recording in VSP

Figure 1.1 shows a cross-sectional view of an offset-VSP ray geometry. Although this scenario is made rather simple by assuming the source energy to be entirely of the P-wave type, one can see that the propagating wavefield can become quite complex. Downgoing P waves convert to downgoing S waves at geological interfaces. Furthermore, P-SV conversion occurs at the reflection point (Aki and Richards, 1980) generating an arrival time at the geophone's location that is composed of the time of P-wave travel in the downgoing mode and the time of S-wave travel in the upgoing mode. An example is shown in Chapter 2 where real three-component VSP sections are displayed.

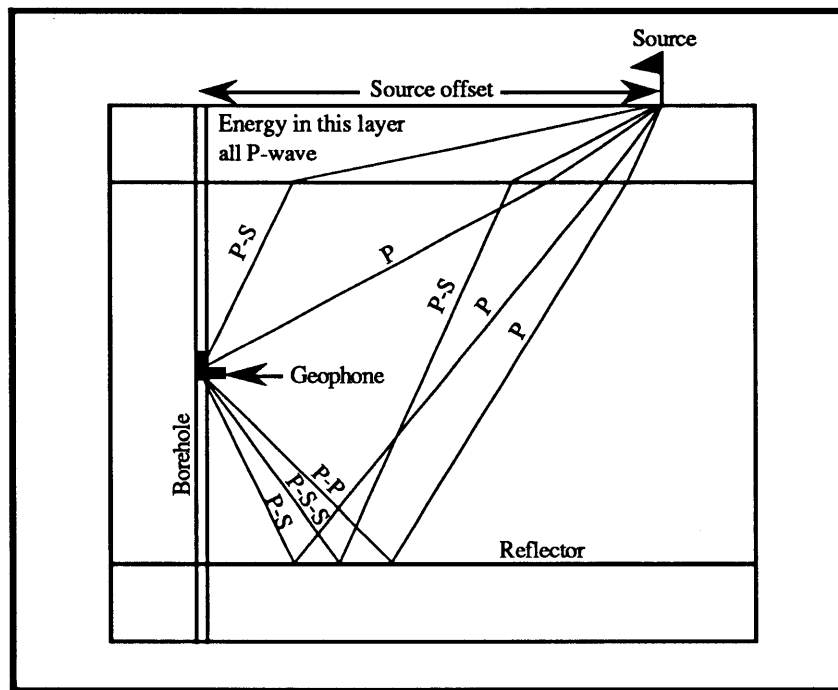


Figure 1.1 Offset VSP geometry.

Also evident in Figure 1 is the variation in angles of incidence for downgoing and upgoing P and S waves. At shallow receiver locations, the angle of incidence of a downgoing P or S wave at the borehole is closer to the horizontal than when the geophone is located deeper in the hole where its angle of incidence at the borehole is closer to the vertical. A similar argument can be followed for an upgoing P or S wave at the receiver: at shallow receiver locations for a given reflector, a reflected wave has an angle of incidence closer to the vertical than at deeper locations where its angle of incidence is further away from the vertical. Because of the variation in angles of incidence of the downgoing and

upgoing wavefields, P waves are recorded partially on the horizontal channel and this part of the signal would not be recorded without a horizontal geophone. Similarly, shear waves are recorded partly on the vertical geophone and cannot be unambiguously separated without other components. In order to record the full wavefield, a vertical and horizontal in-line geophone (in line with the source-receiver direction) are needed to record the vertical and radial components of the propagating wavefield. By doing so, the P-wave section can be improved over the conventional method of vertical component recording, and an attempt can be made at reconstructing the S wavefield.

1.3 Thesis objective

The objective of this thesis is to develop processing algorithms that use both the vertical and radial components of an offset VSP to image the structure and lithology of the subsurface. Chapter 2 deals with the general processing of the two components from the raw field data up to the point where P and P-SV waves are to be separated. The details of the separation of P and P-SV waves from the vertical and radial components are presented in Chapter 3. In Chapter 4, the total P- and P-SV-wave sections are used to map the subsurface reflection points while Chapter 5 deals with inverting the P-SV map to provide an estimate of the S-wave velocity. Figure 1.2 shows a processing flow of the processes implemented in the thesis along with the sections where these processes are discussed.

1.4 Data sets used in the thesis

All the algorithms that are derived in the thesis are applied to two different data sets; namely, a synthetic data set and a real three-component data set.

1.4.1 Synthetic VSP

The synthetic data set was generated using the Uniseis ray-tracing program on the Landmark workstation made available to the CREWES Project at The University of Calgary. The model used in the ray-tracing is made of three layers on top of a half-space with P- and S-wave velocities (V_P and V_S) as shown in Figure 1.3. The density was kept constant at 2200 kg/m^3 . Both vertical and radial components were generated using the following parameters:

Number of traces (depth levels): 75

Geophone depths: 500 - 1980 m

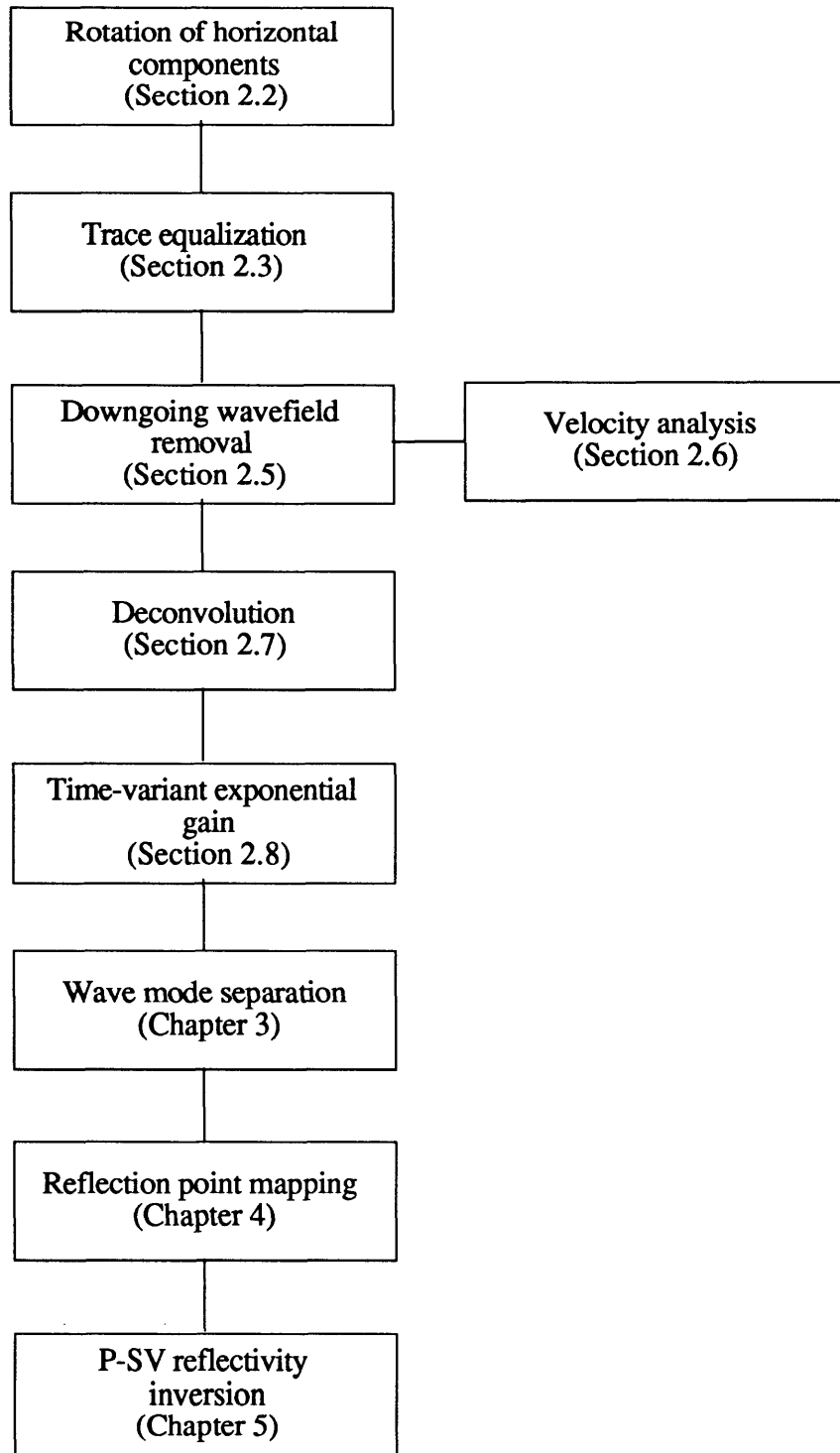


Figure 1.2 Flow chart of the processes implemented in the thesis. The sections in parentheses indicate where the processes are discussed in the thesis.

Geophone spacing: 20 m
 Source offset: 1200 m
 Sampling interval: 0.002 s
 Wavelet: Zero-phase Ricker (30 Hz)

A source generating P-waves only was used and both P-P and P-SV reflections were generated at each interface by the ray-tracing program. Downgoing mode conversion and multiples were not generated in the ray-tracing so that the resulting calculated wavefield consists of a downgoing P wave and upgoing P-P and P-SV reflections. The VSP sections generated in the ray-tracing are shown in Chapter 2 as part of the processing flow.

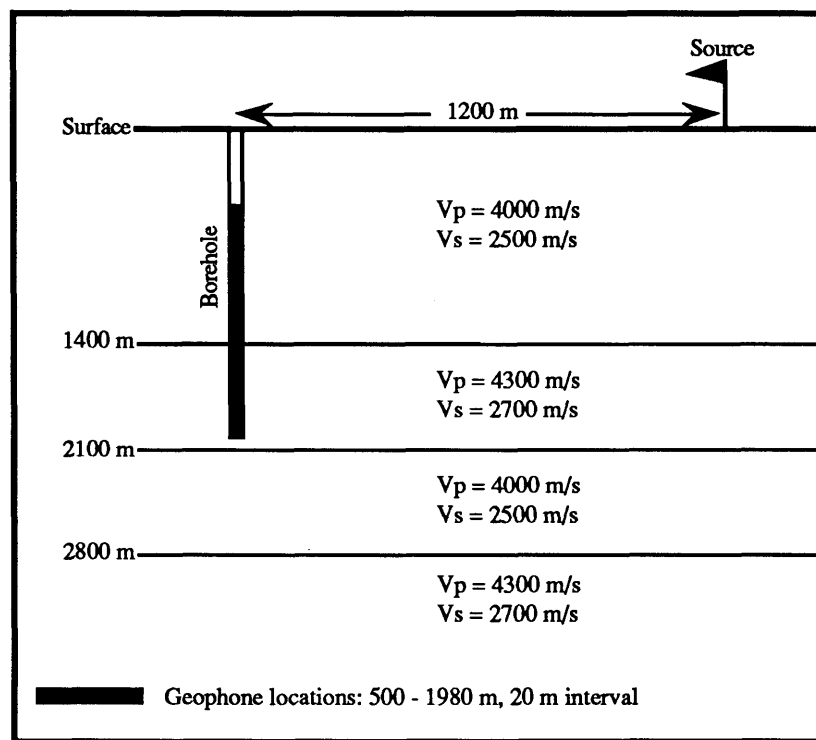


Figure 1.3 Synthetic model used throughout the thesis.

1.4.2 Field VSP

The real three-component data set was recorded in the fall of 1987 by PanCanadian Petroleum Ltd. with the following parameters:

Number of traces (depth levels): 67
 Geophone depths: 520 - 1840 m
 Geophone spacing: 20 m
 Source: P-wave vibrator (Mertz Model-16)

Sweep: 8 - 100 Hertz

Source offset: 325 m

Sampling interval: 0.002 s

The wavefield generated by the vibrator was recorded using three-component geophones. The resulting VSP sections are shown in chapter 2 as part of the processing flow.

1.5 Hardware and software used

All the processes implemented in this thesis were written in FORTRAN and compiled on the Perkin-Elmer computer in the department of Geology and Geophysics of The University of Calgary except for the p-t decompositions and their associated reconstructions which were implemented on the CYBER 205 super computer. All the seismic plots presented in this thesis were generated using the Benson plotter powered by the Perkin-Elmer. The other figures and tables were created using graphics software such as Mathematica, Cricket Graph, Claris CAD and MacDraw on a Macintosh IICx computer. The text was written on the same Macintosh computer with Microsoft Word while the mathematical equations were generated using Expressionist.

Chapter 2 - Three-component VSP Processing

2.1 Introduction

So far, only the vertical and radial components of the recorded seismic wavefield have been considered. The transverse component, the recording channel that is oriented perpendicular to the sagittal plane, has been assumed to contain no valuable information about the P and SV waves. This is only true if the earth is idealized to be horizontally layered and isotropic. If the geological layers present in the subsurface are dipping in a direction that is not the same as the source-receiver direction, then the P and SV waves would have a component on the transverse channel. Furthermore, shear-wave anisotropy in the earth would cause a given shear wave to split into two shear waves, one shear wave being polarized in the direction of the fastest shear-wave velocity while the other would be polarized in the direction of slowest shear-wave velocity (Martin and Davis, 1987). Now, if the direction of fastest or slowest shear-wave velocity is not in line with the source-receiver direction, then the split shear wave would have a component on the transverse channel.

Throughout this thesis, the earth is assumed to be horizontally layered and isotropic. For this reason, only the vertical and radial components are considered. This is not a problem in the synthetic data case as the ray-tracing program calculates the angle of incidence of each ray at the geophone locations and can calculate the vertical and radial components of the seismic wavefield displacements at each time point for every depth level. In the acquisition stage of real VSP data, however, there is a problem that makes the two horizontal components indistinguishable. The problem lies in the fact that most three-component downhole geophones do not have systems to measure downhole orientation. As the geophone is moved up the hole, it rotates and randomly orients the two horizontal components (Figure 2.1). Before any further processing can be done on the real VSP data, the effect of random orientation of the horizontal components between depths must be removed by orienting them to a fixed reference frame.

2.2 Rotation of horizontal components

Without any information about the orientation of the geophone at each depth level, a reference frame inherent in a VSP trace is required to remove the random orientation of the geophone. The most obvious and consistent reference event in a VSP trace is the first

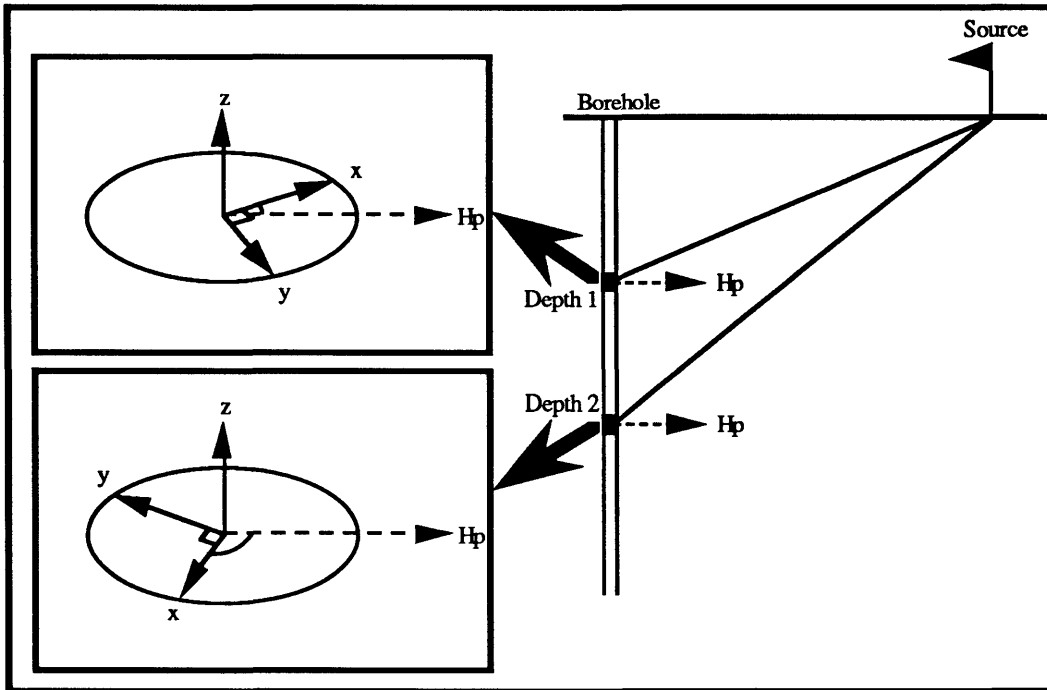


Figure 2.1 VSP geometry exemplifying the downhole geophone orientation problem. The large arrows point to the two small inset which are enlarged views of the two depth levels (modified from DiSiena et al., 1984).

arrival - the downgoing P wave (first break). For a horizontally layered, isotropic earth, the displacement vector of a downgoing P wave lies in the sagittal plane, and the horizontal projection of the downgoing P wave (H_p in Figures 2.1 and 2.2) will be in the same direction as the source-receiver direction. Therefore, the direction of polarization of the downgoing P wave is used as a fixed reference frame since it should be consistent from

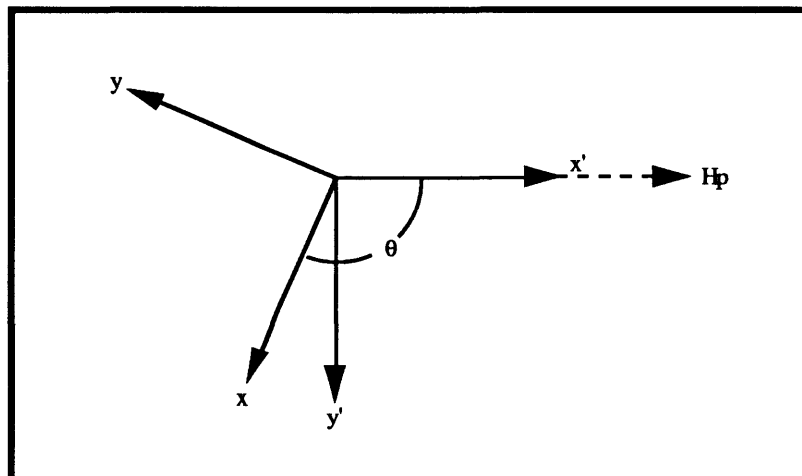


Figure 2.2 Geophone orientation before ($x - y$) and after ($x' - y'$) the removal of the random orientation problem.

depth to depth (DiSiena et al.,1984).

2.2.1 Theory

Mathematically, as derived by DiSiena et al. (1984), the removal of the random orientation is done by performing a coordinate transformation from the $x - y$ axes, the randomly oriented horizontal components, to the $x' - y'$ axes where x' is in line with the H_p direction. That is,

$$X' = X \cos \theta + Y \sin \theta, \quad 2.1a$$

$$Y' = -X \sin \theta + Y \cos \theta, \quad 2.1b$$

where θ is the angle between x and x' (H_p) and X , Y , X' and Y' are the time series recorded along the x , y , x' and y' axes respectively. The idea is to maximize the energy $E(\theta)$ on one of the two horizontal components inside a window centered on the first breaks

$$E(\theta) = \sum_{t=a}^b X'(t)^2, \quad 2.2$$

where a and b are the lower and upper limits of the time window that contains the first breaks. Substituting 2.1a into 2.2

$$E(\theta) = \sum_{t=a}^b (X(t) \cos \theta + Y(t) \sin \theta)^2, \quad 2.3$$

and maximizing $E(\theta)$ by setting

$$\frac{\partial E(\theta)}{\partial \theta} = 0, \quad 2.4$$

we get

$$\frac{2 \sin \theta \cos \theta}{\cos^2 \theta - \sin^2 \theta} = \sum_{t=a}^b \frac{2 X(t) Y(t)}{X(t)^2 - Y(t)^2}. \quad 2.5$$

Equation 2.5 can be simplified to yield the final result

$$\tan 2\theta = \frac{2 X \cdot Y}{X \cdot X - Y \cdot Y} , \quad 2.6$$

where $X \cdot Y$ is the zero-lag crosscorrelation between the two horizontal channels,
 $X \cdot X$ is the zero-lag autocorrelation of the X horizontal channel,
 $Y \cdot Y$ is the zero-lag autocorrelation of the Y horizontal channel, the correlations being calculated inside a time window centered on the first P breaks.

2.2.2 Rolling Hills application

This rotation algorithm was applied to the Rolling Hills data set. First, the first downgoing P-wave arrivals were picked from the vertical component shown in Figure 2.3. The travel-times for the first breaks increase with depth as expected of a downgoing wave. Figures 2.4 and 2.5 depict the two horizontal components, X and Y, as they were originally recorded. The first downgoing P arrival is randomly distributed on the two raw horizontal components as evidenced by its polarity change between depth levels. The rotation algorithm was performed on each set of traces using a time window of 0.1 second centered on the first breaks; this gives rise to one horizontal component consistently oriented in the sagittal plane - the radial component - and one horizontal component consistently oriented and perpendicular to the radial component - the transverse component. The radial component is shown in Figure 2.6 while the transverse component is depicted in Figure 2.7. The first downgoing P-wave break has been maximized on the radial component and minimized on the transverse component as expected.

2.3 Trace equalization on first breaks

The displacement amplitude of the seismic wavefield decreases exponentially in time for a number of reasons including refractive spreading (Newman, 1973). The first step in amplitude recovery of the seismic wavefield in VSP is to equalize the traces with respect to each other. This is done also to assure that there will not be any strong amplitude variations between adjacent traces in the VSP section caused by variations in geophone coupling at different depth levels or variations in source amplitude for different shots. The first downgoing P-wave break is used as a reference event to equalize the trace energy. The idea is to calculate the energy inside a time window centered on the first P breaks and

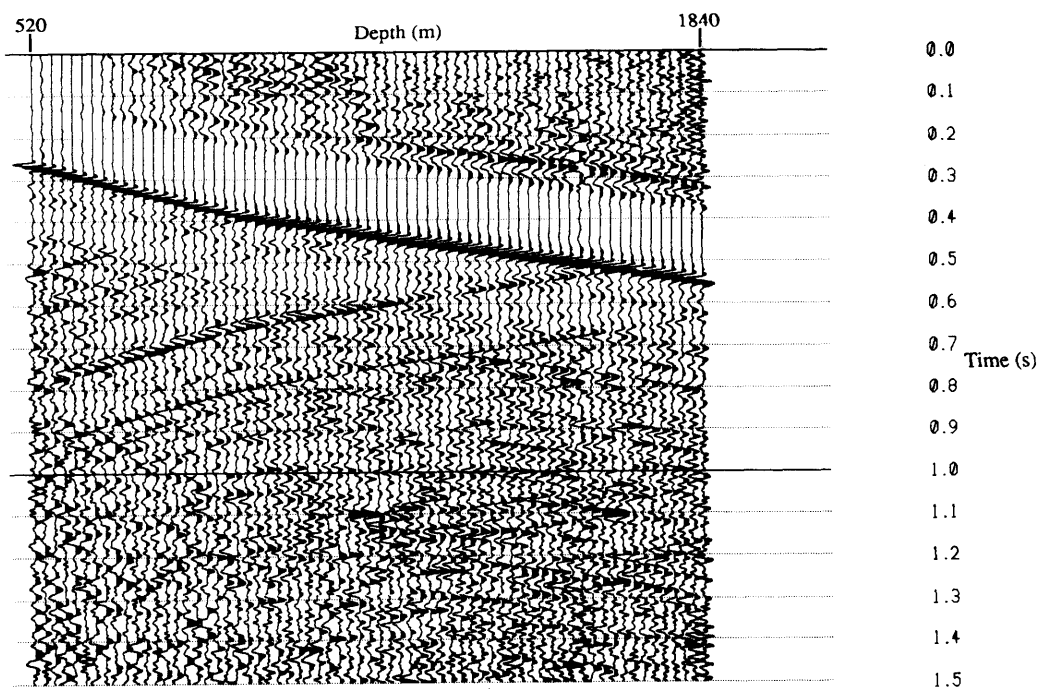


Figure 2.3 Raw vertical component of Rolling Hills data set plotted with Automatic Gain Control (AGC) using a window length of 0.3 s.

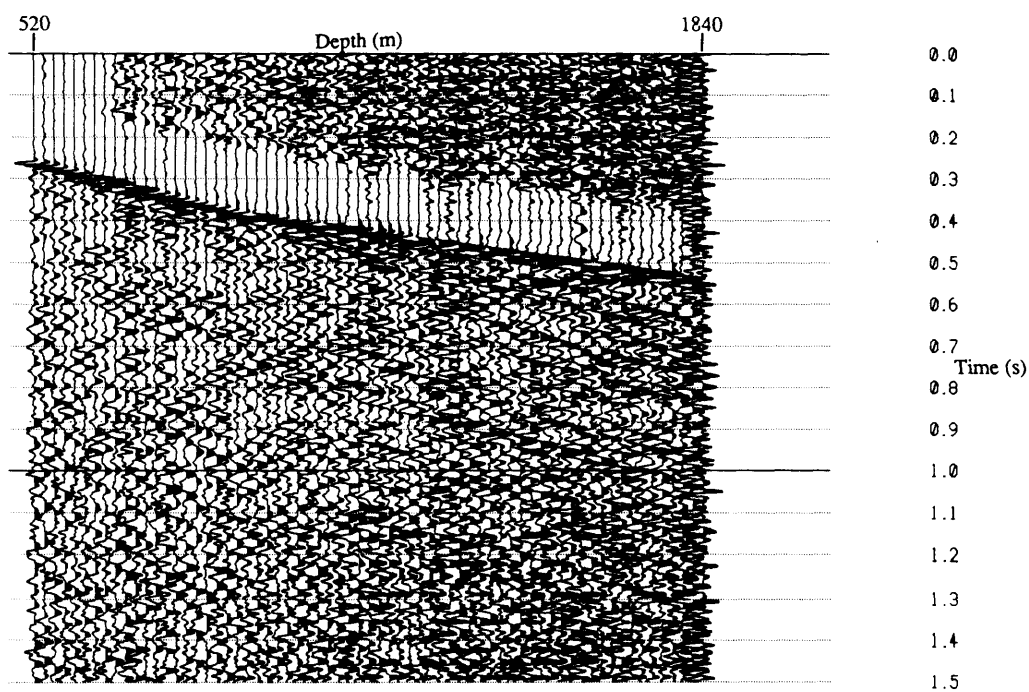


Figure 2.4 Raw horizontal component (X) of Rolling Hills data set plotted with an AGC window length of 0.3 s.

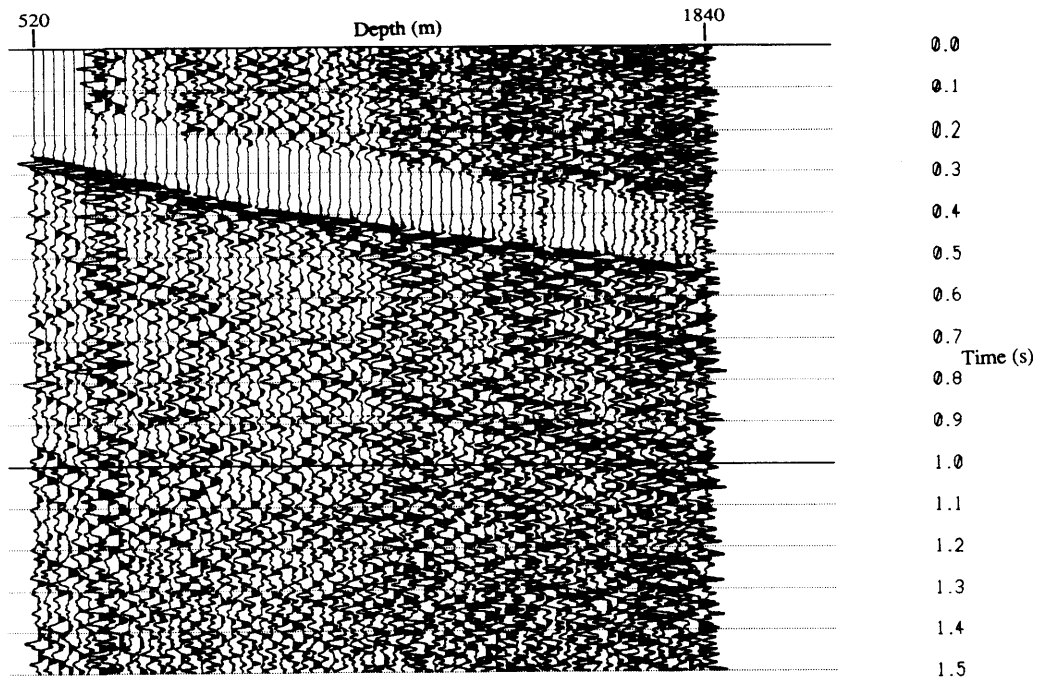


Figure 2.5 Raw horizontal component (Y) of Rolling Hills data set plotted with an AGC window length of 0.3 s.

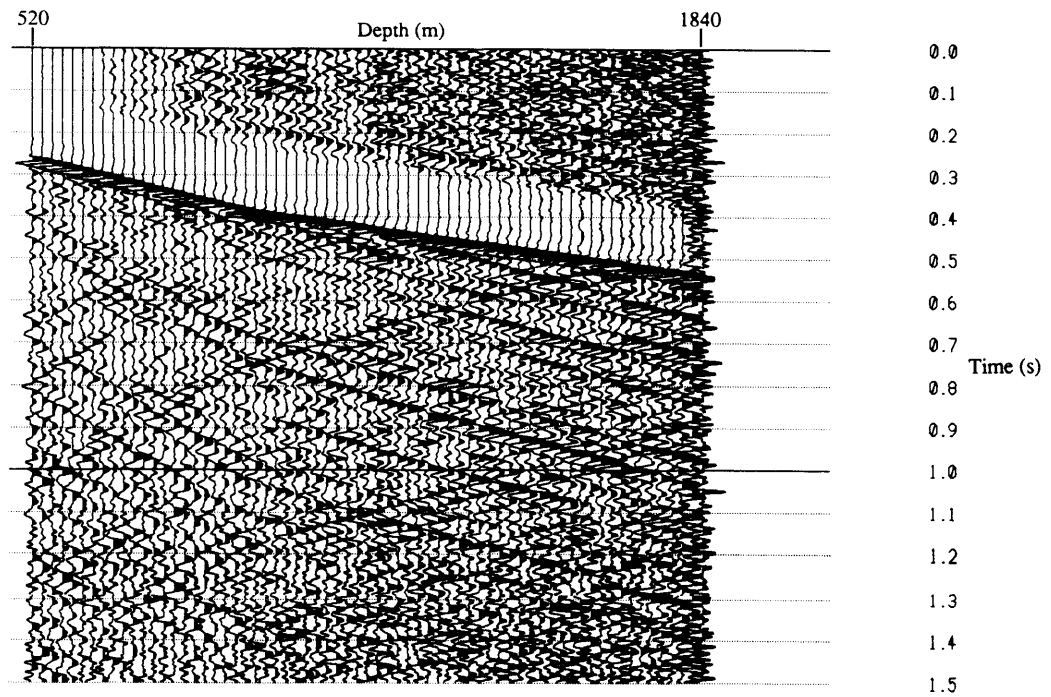


Figure 2.6 Raw radial component of Rolling Hills data set plotted with an AGC window length of 0.3 s.

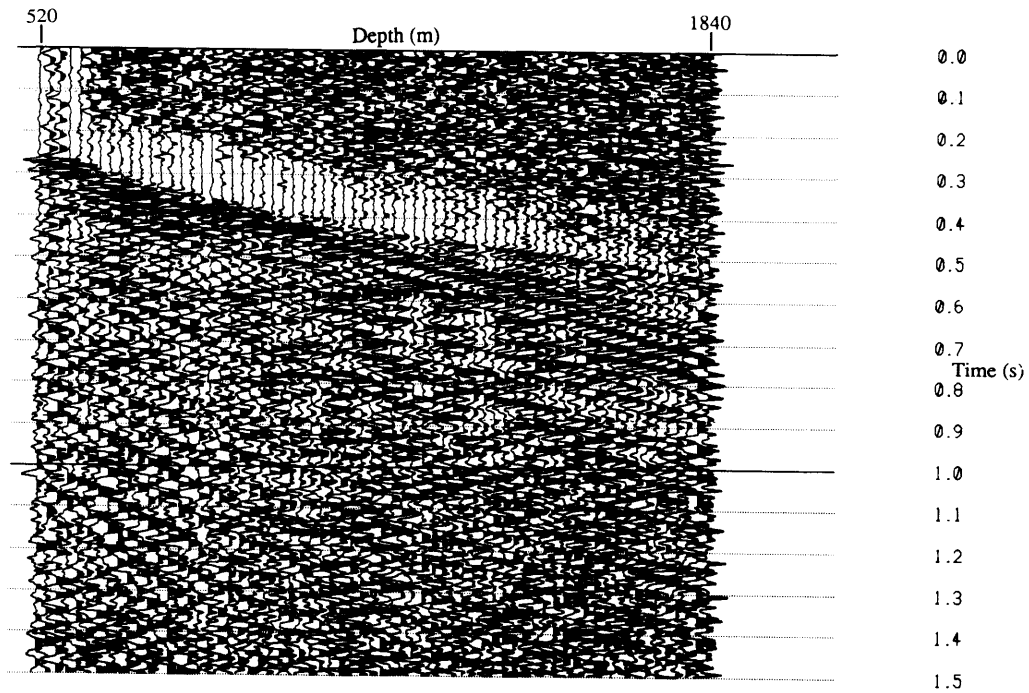


Figure 2.7 Raw transverse component of Rolling Hills data set plotted with an AGC window length of 0.3 s.

multiply each trace by a constant factor such that the energy level is the same (a constant C) on each trace. In order to preserve the spatial similarity and polarization orientations of the seismic events, the same factor must be applied to the vertical (V) and radial (R) components for a given trace. Therefore, the total energy at a given depth level z , $E(z)$, has to be calculated such that

$$E(z) = \sum_{i=a}^b (V_i^2 + R_i^2) = C, \quad 2.7$$

where a and b are the upper and lower limits of the time window centered on the first breaks. This algorithm does not need to be applied to the synthetic data since the ray-tracing program does not take into account amplitude losses due to spherical divergence. Figure 2.8 and 2.9 show the vertical and radial components of the Rolling Hills data plotted as true relative amplitudes, that is, with the same relative gain applied to all the traces in both figures before plotting, as all the seismic plots shown from now on in this thesis will be unless otherwise stated. The amplitudes of the events decay rapidly from the shallow traces. A window length of 0.1 second was used so that $b-a=50$ samples. Figure 2.10 and

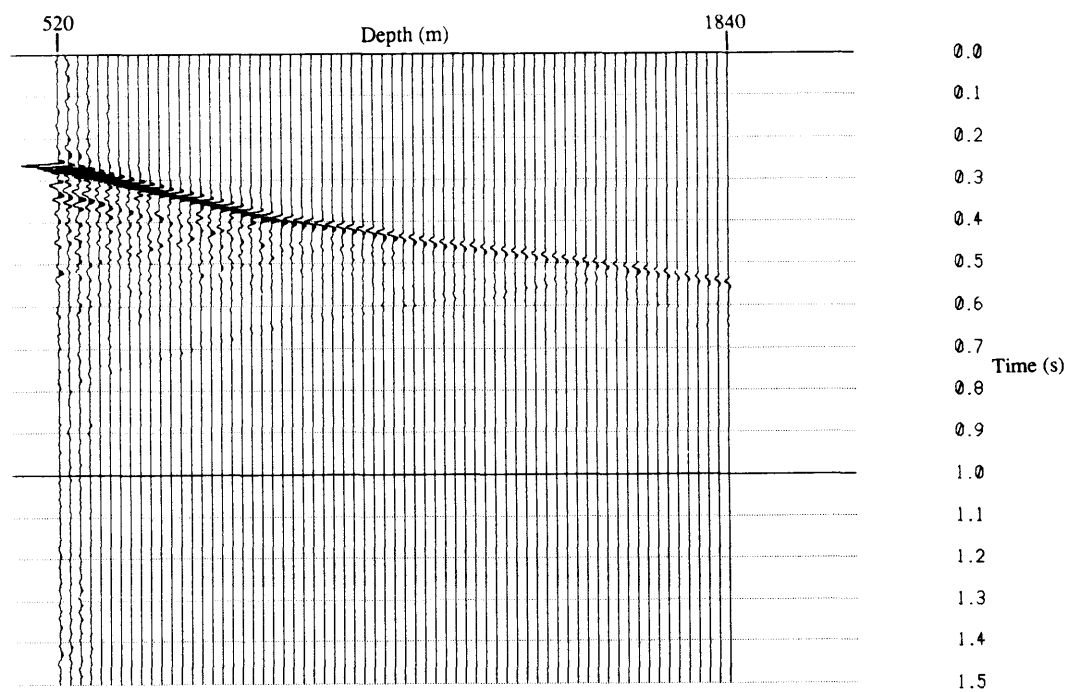


Figure 2.8 Raw vertical component of Rolling Hills data set plotted as true relative amplitudes.

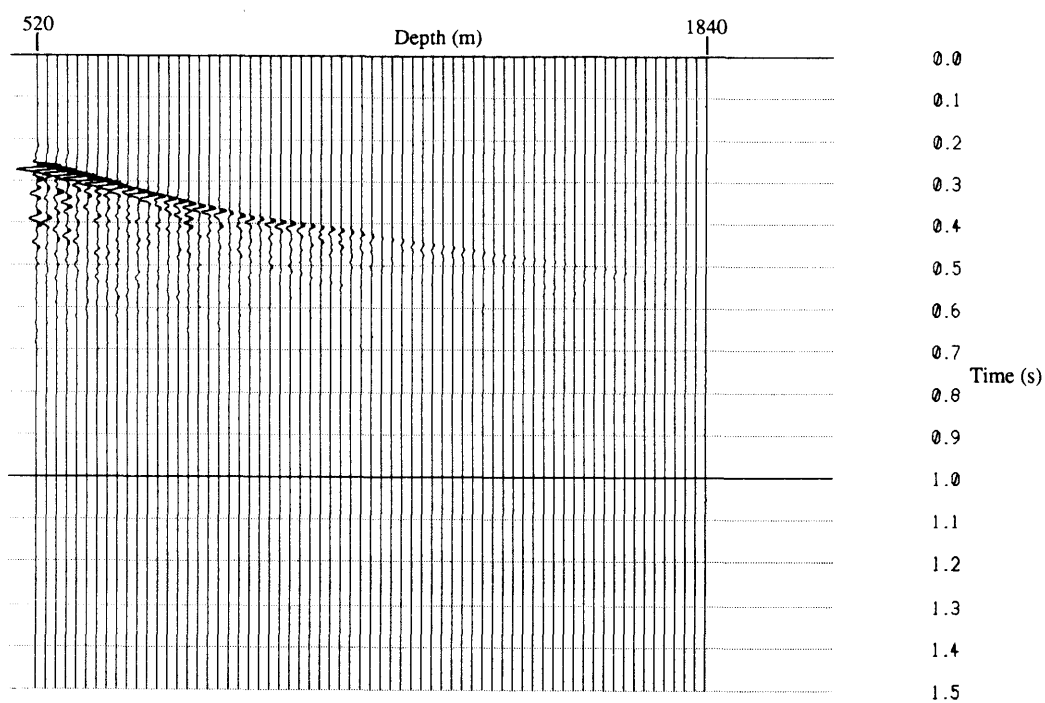


Figure 2.9 Raw radial component of Rolling Hills data set plotted as true relative amplitudes.

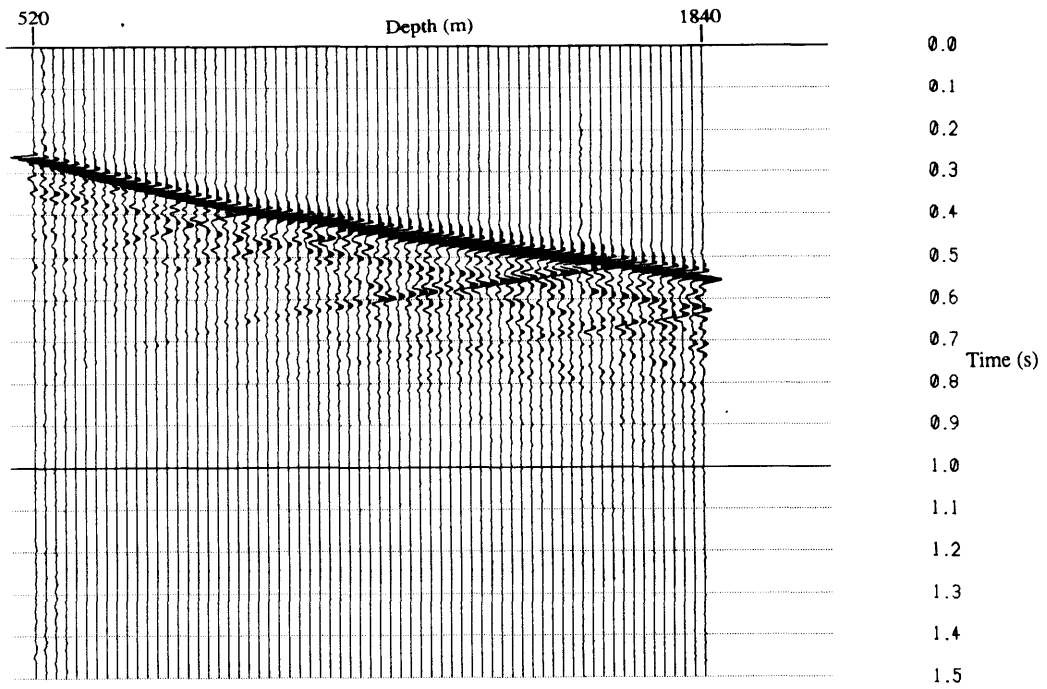


Figure 2.10 Trace-equalized vertical component of Rolling Hills data set plotted as true relative amplitudes.

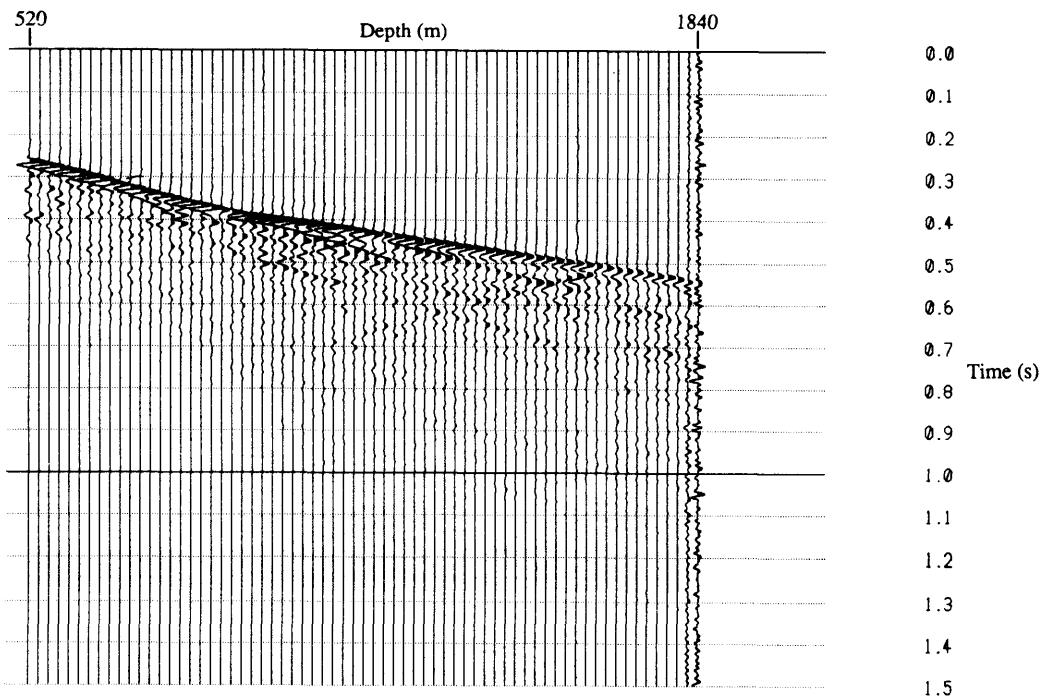


Figure 2.11 Trace-equalized radial component of Rolling Hills data set plotted as true relative amplitudes.

2.11 show the trace-equalized equivalents of Figure 2.8 and 2.9. The amplitudes of the first-break events are more equalized with depth as expected from the algorithm.

2.4 The p-t decomposition

A little digression from the main processing flow is now taken to introduce the slowness decomposition method, the p-t decomposition, that will later be used in the downgoing wavefield removal (Section 2.5) and the P-S separation (Chapter 3). The p-t decomposition is an algorithm developed by Cheadle (1988) at The University of Calgary. This program runs on the CYBER 205 and was adapted to perform dip filtering and modal separation of VSP data.

2.4.1 Theory

The filtering operation is performed by partitioning the data into panels, each containing an odd number of traces equal to the window length used in the filtering process. The center of each panel corresponds to the output trace position and there are as many panels as there are input traces. A given panel in the depth-time (z-t) domain $U(z,t)$ is transformed into the p-t space by slant-stacking (Claerbout, 1985) or amplitude summing over a range of slownesses, and then projecting these slant stacks onto the center trace of the window (Cheadle, 1988). Thus we have:

$$U'(p,t) = \int_{z_0}^{z_1} U(z,t+zp) dz, \quad 2.8$$

where p corresponds to the horizontal slowness (p_x) in the surface seismic case and the vertical slowness (p_z) in the VSP case, and t corresponds to the time on the trace at the center of the local window that has z_0 and z_1 as its depth boundaries. The exact inverse transform of equation 2.8 has the form (Foster and Gaiser, 1986)

$$U(z,t) = \int_{p_0}^{p_1} \frac{d}{dt} H \{U'(t-pz,p)\} dp, \quad 2.9$$

where H is the Hilbert transform, $\frac{d}{dt}$ is a time derivative and p_0 and p_1 are the lower and upper bounds of the range of slownesses used in the reconstruction of $U(z,t)$. This exact inverse transform process, however, is a time-consuming operation, especially if it has to be done for every local window. As an alternative to the exact inverse transform, the data can be inverse-transformed to an estimate of the center trace by integrating over the range of slownesses p

$$\tilde{U}(t) = \int_{p_0}^{p_1} U'(p,t) dp, \quad 2.10$$

where $\tilde{U}(t)$ is the reconstructed estimate of the center trace of the local window and p_0 and p_1 are as in equation 2.9 (Cheadle, 1988). Equation 2.10 is similar to the backprojection methods used in tomography (Stewart, 1989a). This backprojection is not the inverse of the forward p - t decomposition, although it is a rough approximation of the exact inverse of equation 2.9.

The vertical component of the downgoing P arrivals for the synthetic model shown in Figure 2.12 was used to test this simple concept of the forward decomposition using equation 2.8 and the inverse reconstruction estimate of equation 2.10. Figure 2.13 shows the p - t decomposition for the local window centered on the 980-meter trace. A local window length of 9-traces was used in the forward decomposition. The panels at or near the edges of the VSP section are padded with traces of zeroes to accommodate the filter window. The p values range from 0 to 750×10^{-6} s/m with a 5×10^{-6} s/m trace interval resulting in 151 traces in each decomposition.

The 980-meter depth level lies well within the first layer of the model with $V_P = 4000$ m/s. The apparent velocity of the downgoing P wave at that depth will be $V_{ap} = V_P/\sin \theta$ where $\tan \theta = \text{depth}/\text{offset} = 980\text{m} / 1200\text{m}$. This gives $V_{ap} = 6324$ m/s which translates to a slowness of $p = 1/6324 = 158 \times 10^{-6}$ s/m which is marked as 0.155×10^{-3} s/m on Figure 2.13. The time of arrival of the downgoing P wave at the 980-meter depth is approximately 0.380 second and the event can be seen at that same time on the p - t decomposition. The event, however, is badly smeared over a large range of slownesses so that, when the 980-meter trace is reconstructed by stacking across all slownesses ($0 - 750 \times 10^{-6}$ s/m), the downgoing P wave gets smeared in time giving rise to unwanted smeared

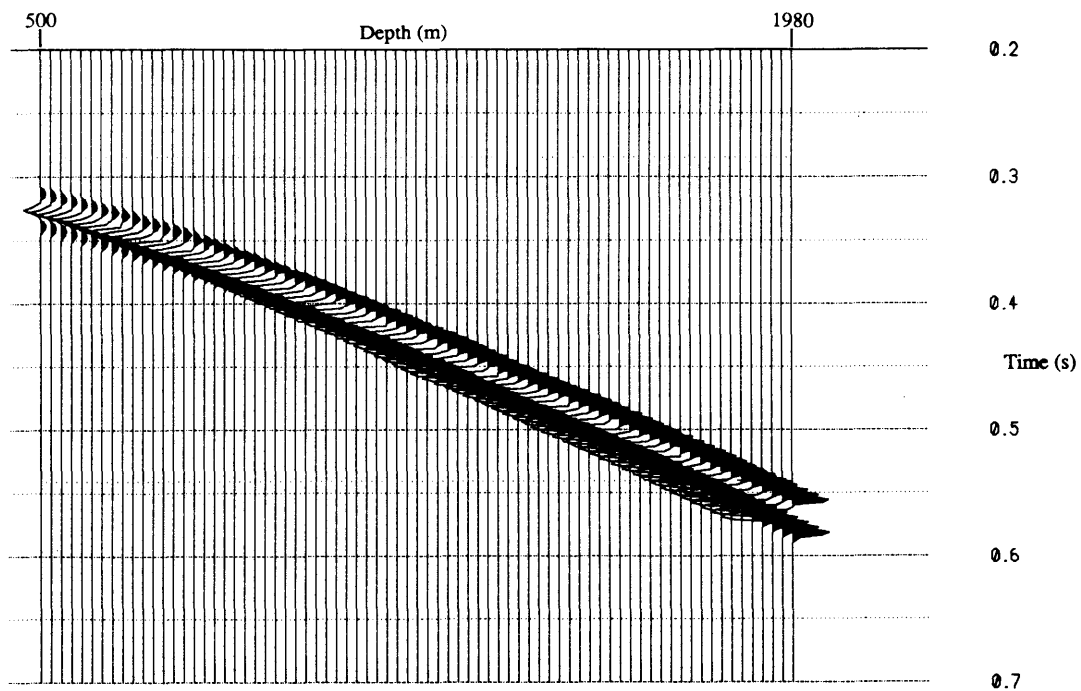


Figure 2.12 Raw vertical component of synthetic data set.

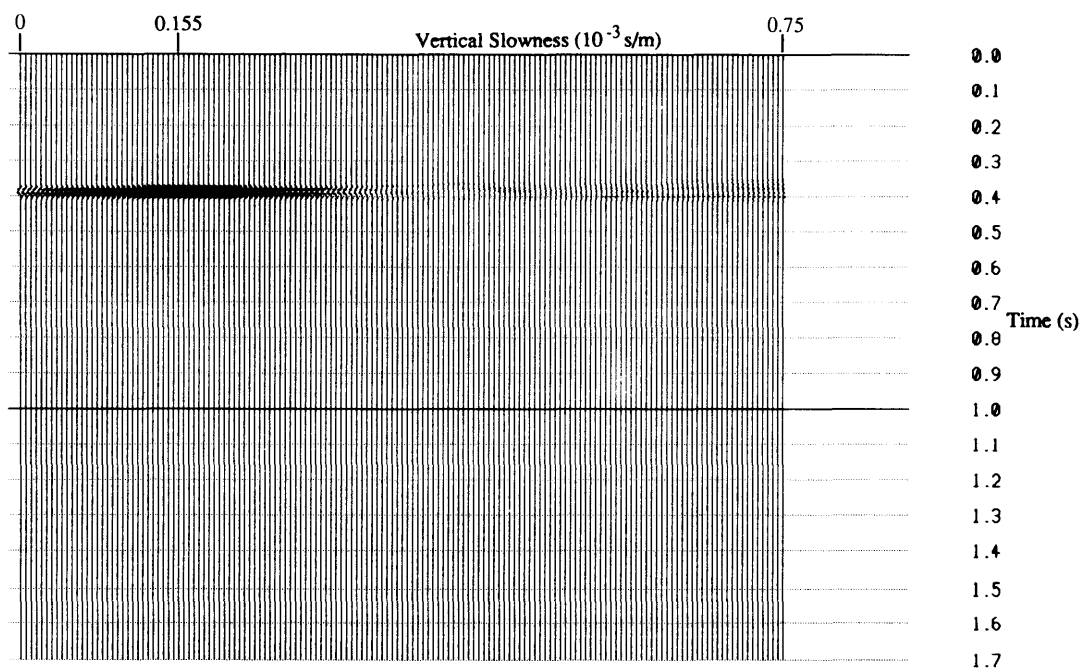


Figure 2.13 p-t decomposition of the 9-trace local window centered on the 980-meter trace for the vertical component of the synthetic data.

energy in the reconstructed trace. Figure 2.14 shows the resulting downgoing P-wave section after each trace was decomposed in the p-t domain using a local window length of 9-traces and reconstructed by stacking across all slownesses. The smearing of the downgoing P wave in time can clearly be observed. This smearing problem occurs because equation 2.10 is not an exact inverse, rather, it is similar to a backprojection. The smearing effect is lessened by applying a semblance weighting at each time point in the p-t decomposition.

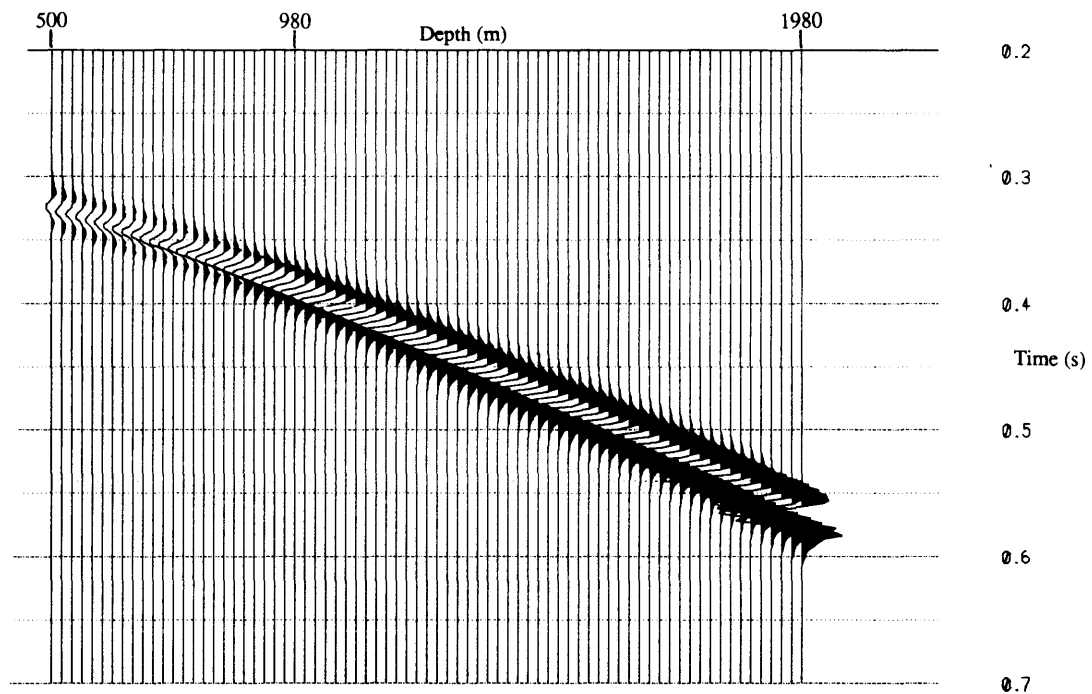


Figure 2.14 VSP section reconstructed from stacking the raw decompositions across the range of all slownesses for each 9-trace local window of the raw vertical component of the synthetic data set.

2.4.2 Semblance weighting

A semblance, S , can be calculated for a given p-t pair as $U(z,t)$ is being decomposed:

$$S = \frac{\left[\sum_{z=b1}^{b2} U(z,t+zp) \right]^2}{N \sum_{z=b1}^{b2} (U(z,t+zp))^2} \quad 2.11$$

(Cheadle, 1988). This semblance represents the normalized ratio of energy of sum to sum of energies of a stack of N trace values along a slope p and a center-trace time t in the local window being decomposed. In this case $N = b2 - b1 + 1$, where $b1$ and $b2$ are the upper and lower depth limits of the local window being decomposed. The semblance is high where the coherency of the signal is high in the local window. In this fashion, as each local window is being decomposed, a semblance value is calculated for each p - t pair. Problems arise, however, when a given series of $U(z,t)$ values, for a given p - t pair, happens to fall on a series of near zero-crossings of coherent events. In this case the calculated semblance value is very small and can actually be undefined if the series of $U(z,t)$ values at a given p - t pair are all zeroes; in the latter case the semblance value is set to zero. The low-semblance problem near zero-crossings of coherent events is solved by averaging the semblance values for a given p over a time range equal to at least one half of the longest wavelength in the data (Cheadle, 1988). By simply multiplying each point on the p - t decomposition by its averaged semblance value, the regions with high semblance will be enhanced with respect to the regions with low semblance.

The semblance weighting was applied to the p - t decomposition with an averaging time-window length of 0.04 second (20 samples) and the results are shown in Figure 2.15. The downgoing P wave is no longer smeared over a large range of slownesses, but, rather, it is localized to a small range of slownesses centered at $p = 158 \times 10^{-6}$ s/m (0.155×10^{-3} shown on the plot). Applying the semblance weighting to every decomposition and reconstructing each trace results in the VSP section shown in Figure 2.16. Comparing this with Figure 2.14, the P-wave event is no longer smeared in time as the original wavefield has been recovered.

2.5 Downgoing wavefield removal

It has been mentioned that the VSP section contains both upgoing and downgoing waves. The downgoing wavefield now needs to be removed to yield the upgoing reflected events which are more important to imaging (Hardage, 1985). They will later be mapped

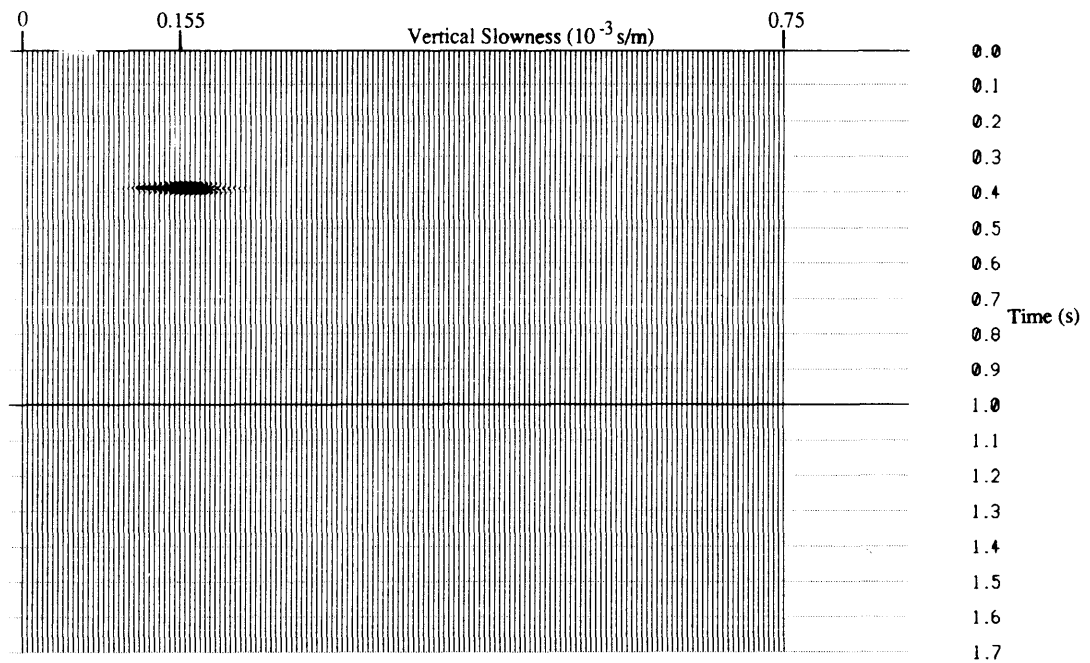


Figure 2.15 Semblance-weighted p-t decomposition of the 9-trace local window centered on the 980-meter trace for the vertical component of the synthetic data.

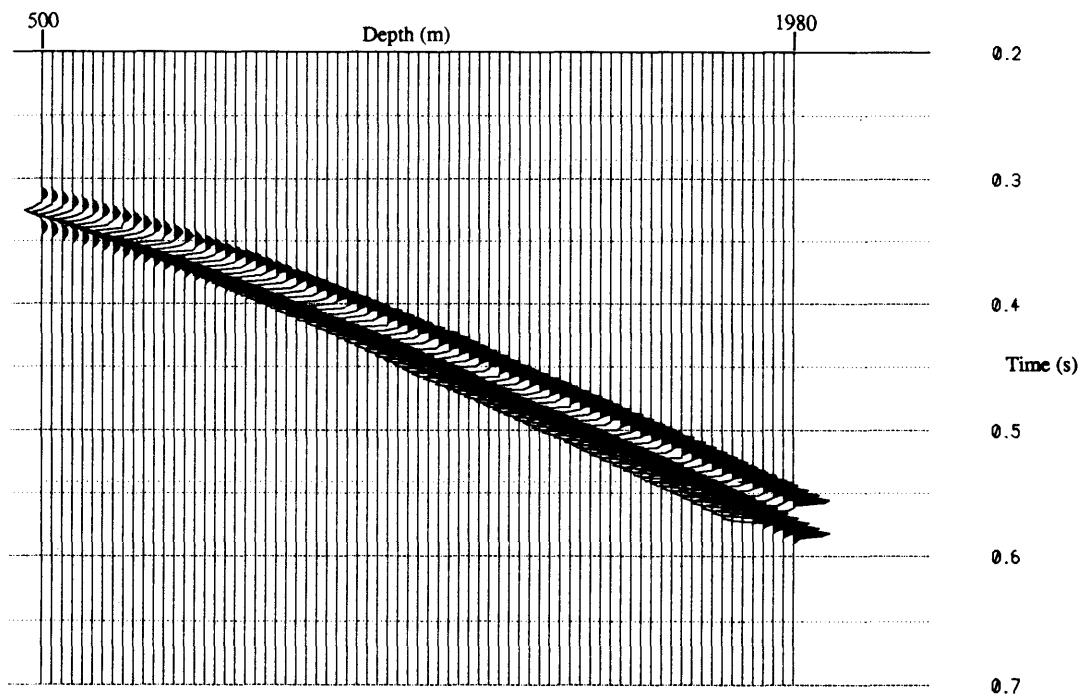


Figure 2.16 VSP section reconstructed from stacking the semblance-weighted decompositions across the range of all slownesses for each local window of the raw vertical component of the synthetic data set.

to their reflection points.

2.5.1 Synthetic case

In the synthetic case, since there are no downgoing S waves nor any downgoing multiples, the downgoing wavefield is removed simply by muting the first P breaks. The raw vertical and radial components for the synthetic data are shown in Figures 2.17 and 2.18 respectively. The downgoing P wave is observed to have a radial component at shallow depths that is larger than the vertical component; similarly, the downgoing P wave is seen to have a vertical component that is larger than the radial component at deeper depths. On the other hand, the amplitude of the downgoing P wave on both the radial and vertical components is so high that it completely overshadows the presence of P-P and P-SV reflections on the true relative-amplitude plots. The muted vertical and radial components are shown in Figures 2.19 and 2.20, respectively. The upgoing wavefield plots have been scaled up by a factor of 1000 with respect to the downgoing wavefield plots. Three P-wave (PP1, PP2, PP3) and three converted S-wave (PS1, PS2, PS3) reflection events corresponding to the three geological interfaces of the model can clearly be

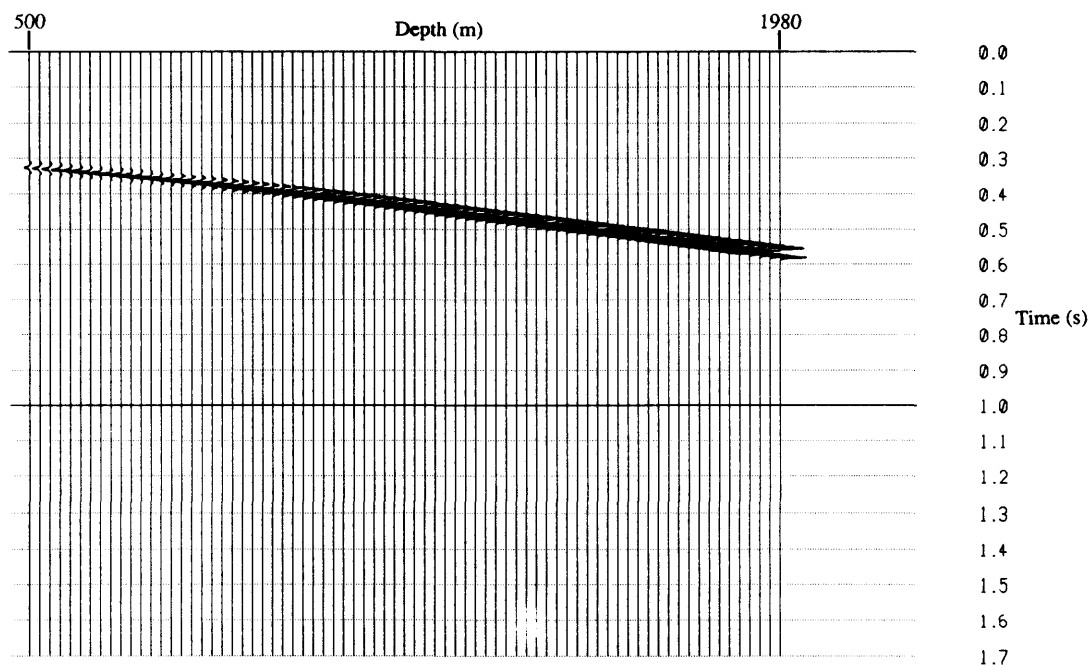


Figure 2.17 Raw vertical component of synthetic data set.

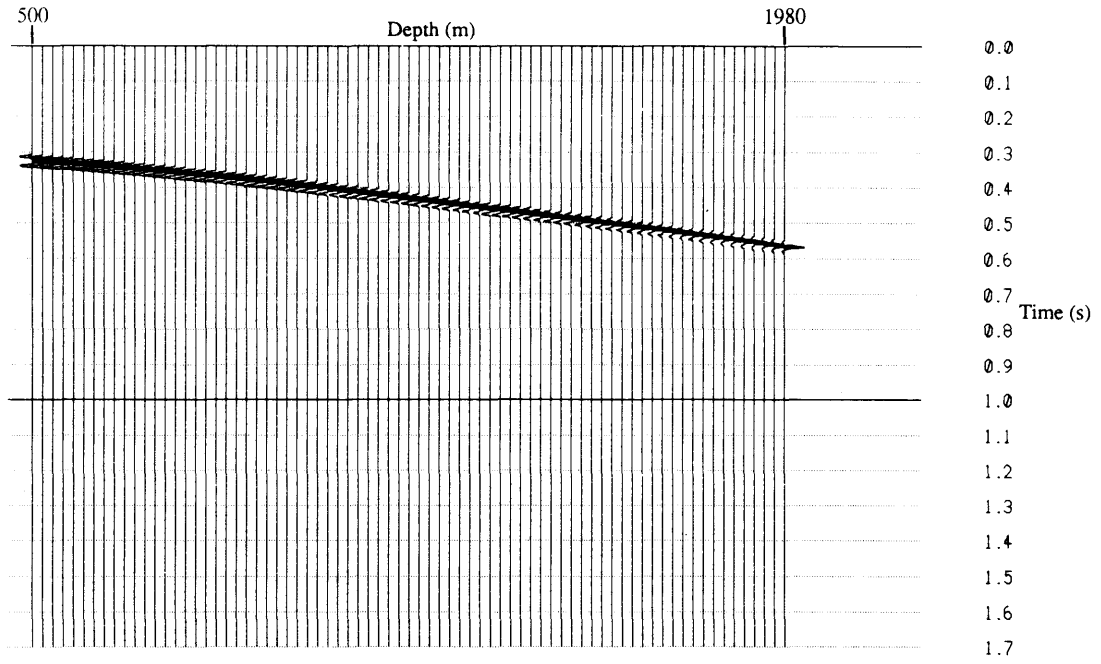


Figure 2.18 Raw radial component of synthetic data set.

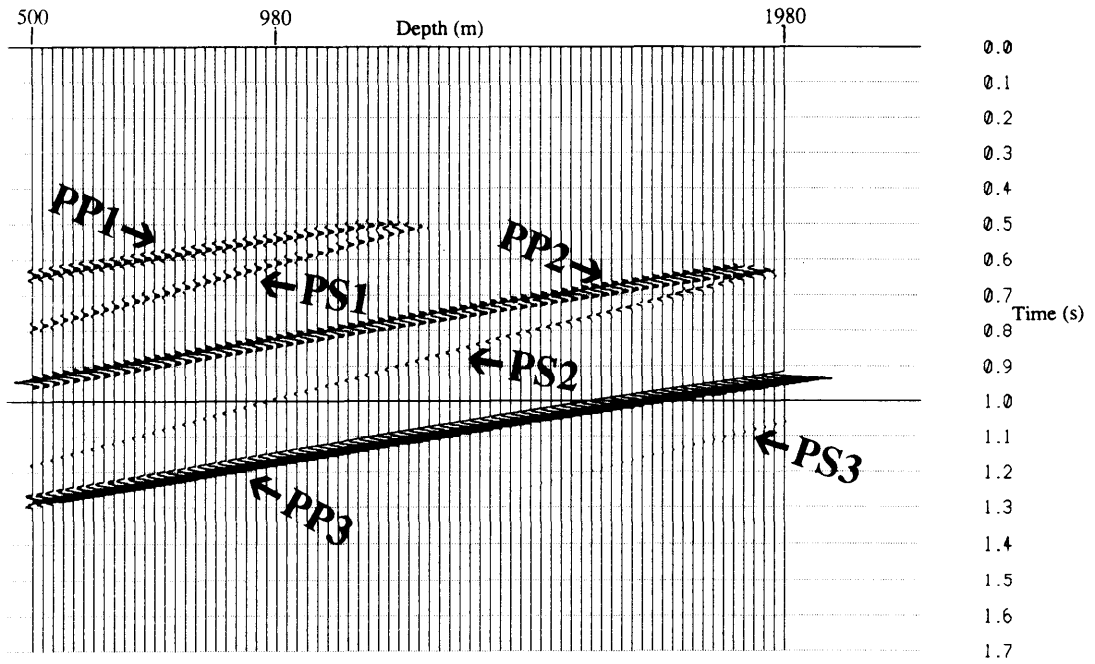


Figure 2.19 Vertical component of synthetic data set with first breaks muted.

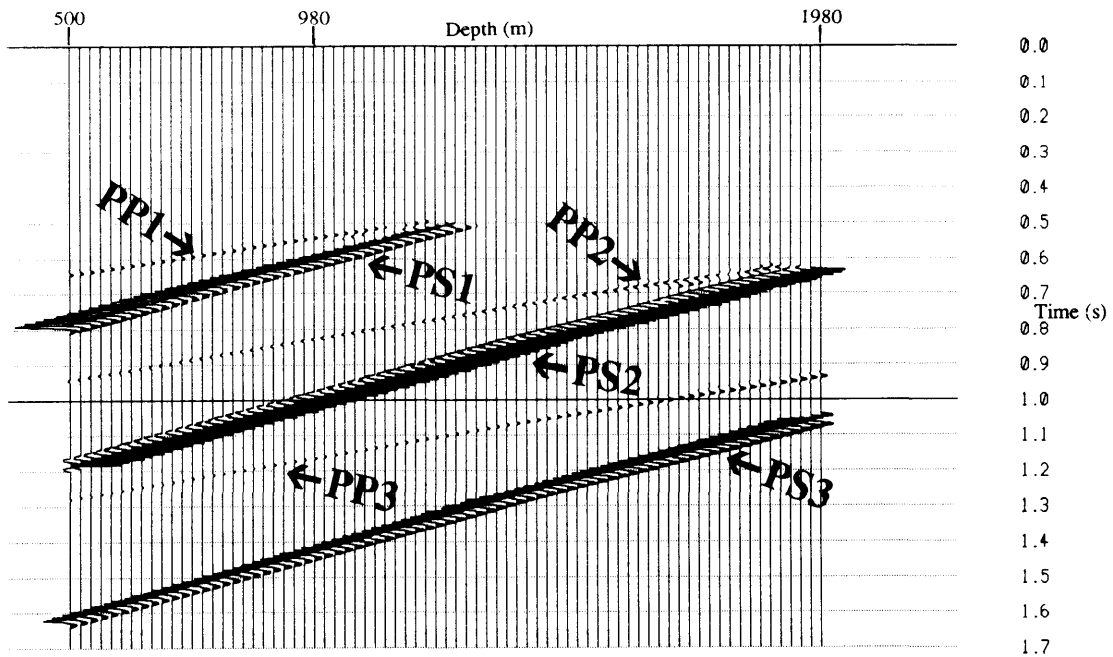


Figure 2.20 Radial component of synthetic data set with first breaks muted.

seen on both the vertical and the radial components. The total particle displacement of the converted S-wave reflections, deduced from the vector addition of the vertical and radial components, is much larger than the total P-wave amplitudes. This unexpected observation can be explained by looking at the reflection coefficients for each interface.

The P-P and P-SV reflection coefficients (R_{pp} and R_{ps}) at a welded interface between two homogeneous, isotropic half-spaces with physical parameters as shown in Figure 2.21 are defined by Aki and Richards (1980) as

$$R_{pp} = \frac{\left(b \frac{\cos \theta_1}{\alpha_1} - c \frac{\cos \theta_2}{\alpha_2}\right) F - \left(a + d \frac{\cos \theta_1}{\alpha_1} \frac{\cos \varphi_2}{\beta_2}\right) K p^2}{D} \quad 2.12$$

$$R_{ps} = \frac{-2 \frac{\cos \theta_1}{\alpha_1} \left(a b + c d \frac{\cos \theta_2}{\alpha_2} \frac{\cos \varphi_2}{\beta_2}\right) p \alpha_1}{\beta_1 D},$$

where $a = \rho_2 (1 - 2 \beta_2^2 p^2) - \rho_1 (1 - 2 \beta_1^2 p^2)$, $b = \rho_2 (1 - 2 \beta_2^2 p^2) + 2 \rho_1 \beta_1^2 p^2$,

$$c = \rho_1 (1 - 2 \beta_1^2 p^2) + 2 \rho_2 \beta_2^2 p^2, \quad d = 2 (\rho_2 \beta_2^2 - \rho_1 \beta_1^2),$$

$$E = b \frac{\cos \theta_1}{\alpha_1} + c \frac{\cos \theta_2}{\alpha_2}, \quad F = b \frac{\cos \varphi_1}{\beta_1} + c \frac{\cos \varphi_2}{\beta_2},$$

$$G = a - d \frac{\cos \theta_1}{\alpha_1} \frac{\cos \varphi_2}{\beta_2}, \quad K = a - d \frac{\cos \theta_2}{\alpha_2} \frac{\cos \varphi_1}{\beta_1}, \quad \text{and } D = E F + G K p^2.$$

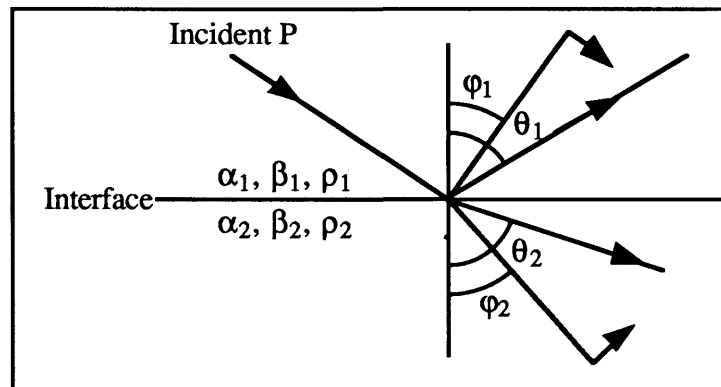
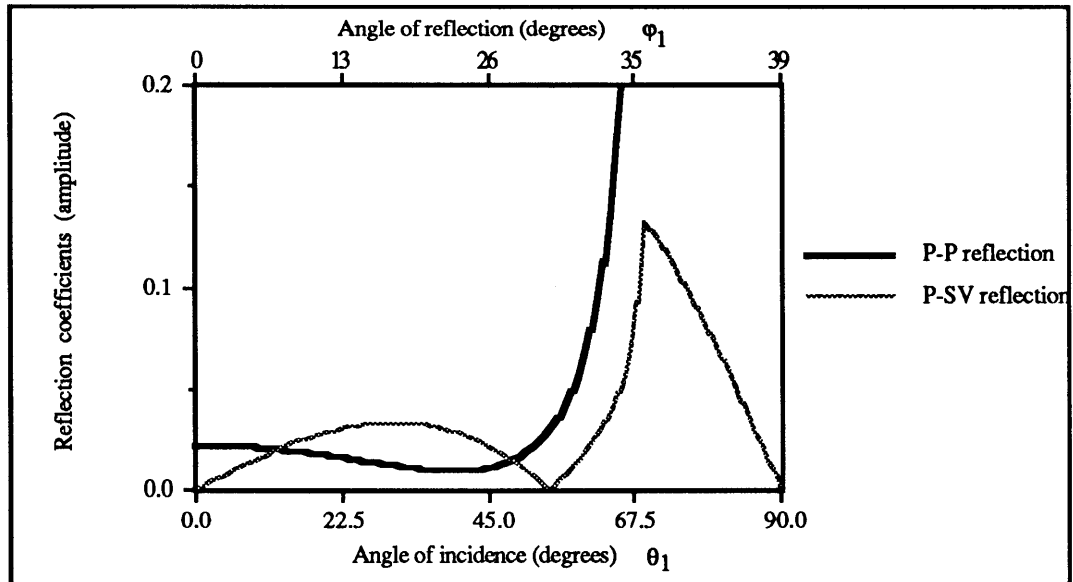
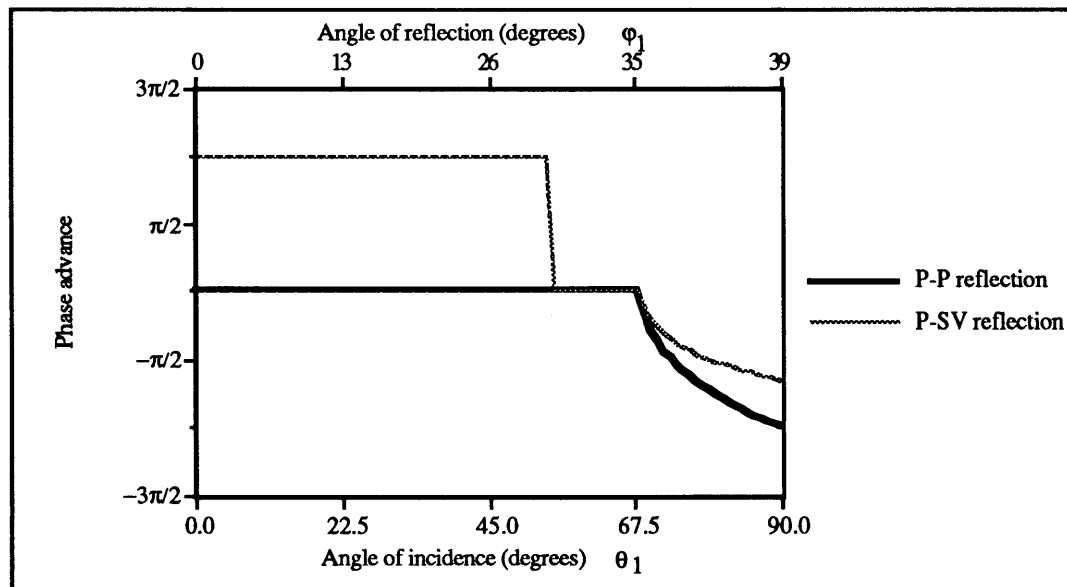


Figure 2.21 Notation for possible reflection/transmission coefficients at a welded interface between two different solid half-spaces. Short arrows show the direction of particle motion. The arrows only show the general particle motion of the reflected/transmitted wavefield, i.e. P versus S waves (after Aki and Richards, 1980).

In this case, the horizontal slowness, $p \equiv p_x$, is related to the angles of transmission and reflection as governed by Snell's law, namely $p_x = \frac{\sin \theta_1}{\alpha_1} = \frac{\sin \theta_2}{\alpha_2} = \frac{\sin \varphi_1}{\beta_1} = \frac{\sin \varphi_2}{\beta_2}$. In the equations above, α and β denote P- and S-wave velocities, and θ and φ denote P- and S-wave angles of incidence respectively. Equations 2.12 were programmed into a microcomputer and the reflection coefficients R_{pp} and R_{ps} were calculated as a function of angle of incidence for the two types of interfaces present in the model. The results of these calculations are plotted in Figures 2.22 and 2.23. Figure 2.22 (a) depicts the P-P and P-SV reflection coefficient amplitudes (the moduli of the complex numbers) as a function of angle of incidence of the incoming P wave for the first and third reflector in the synthetic model, while Figure 2.22 (b) shows the relative phase (the principal value of the argument of the complex numbers) of the two events as a function of angle of incidence of the downgoing P wave. Figures 2.23 depict the same pair of plots for the second reflector present in the synthetic model. The phase advance plots for the P-SV reflection cases show nearly vertical lines at angles of incidence of 55 degrees on Figure 2.22b and at 62 degrees on Figure 2.23b; these angles are the critical angles (Sheriff and Geldart, 1983). These lines should show as exactly vertical lines; they show as nearly vertical lines because the

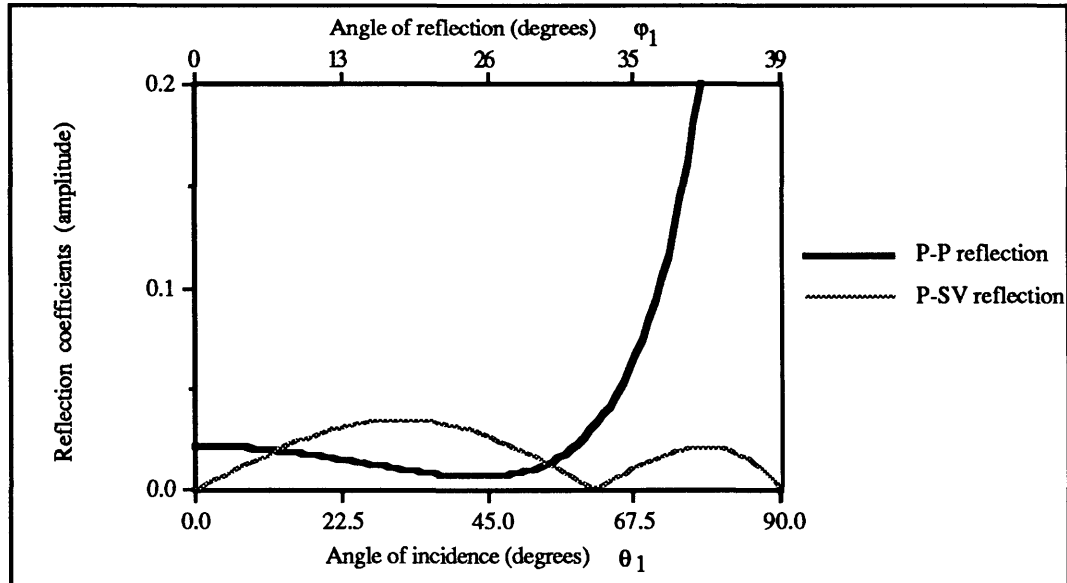


(a)

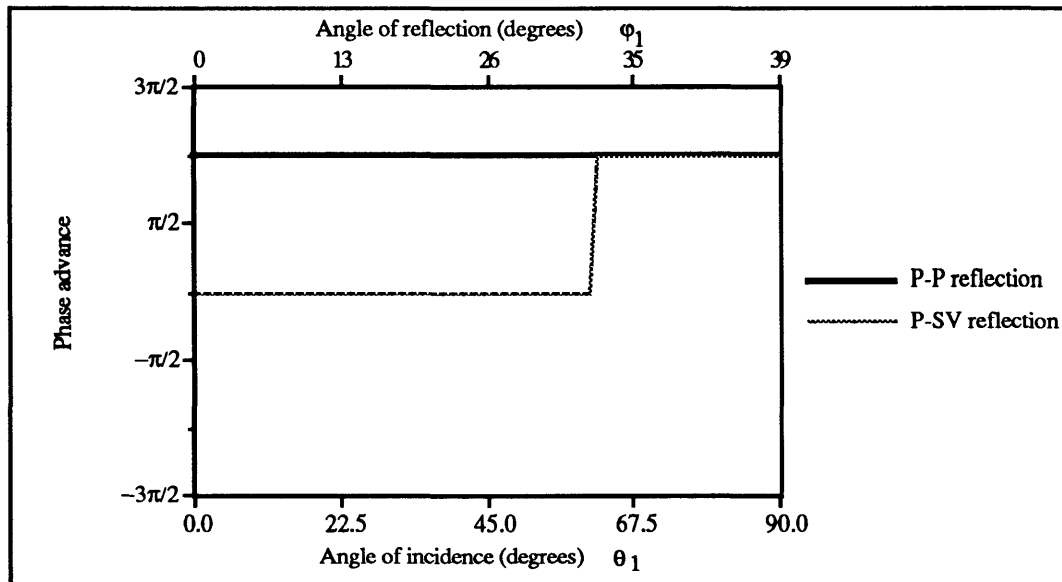


(b)

Figure 2.22 Amplitude (a) and phase advance (b) of P-P and P-SV reflection coefficients plotted as a function of angle of incidence of an incoming P wave. The parameters used in generating the plot are $\alpha_1 = 4000$ m/s, $\beta_1 = 2500$ m/s, $\rho_1 = 2200$ kg/m³, $\alpha_2 = 4300$ m/s, $\beta_2 = 2700$ m/s, $\rho_2 = 2200$ kg/m³. The converted wave reflection angles corresponding to the P-wave incidence angles are also shown on the top horizontal axis.



(a)



(b)

Figure 2.23 Amplitude (a) and phase advance (b) of P-P and P-SV reflection coefficients plotted as a function of angle of incidence of an incoming P wave. The parameters used in generating the plot are $\alpha_1 = 4300$ m/s, $\beta_1 = 2700$ m/s, $\rho_1 = 2200$ kg/m³, $\alpha_2 = 4000$ m/s, $\beta_2 = 2500$ m/s, $\rho_2 = 2200$ kg/m³. The converted wave reflection angles corresponding to the P-wave incidence angles are also shown on the top horizontal axis.

numbers used in plotting Figures 2.22 and 2.23 were generated at one degree intervals.

In order to use Figures 2.22 and 2.23, an estimate of the angles of incidence is needed. Figure 2.24 shows the geometry of the ray paths for P-P reflections from the 1400 m interface recorded at the 500 m and 1400 m depths. For the 500 m depth case,

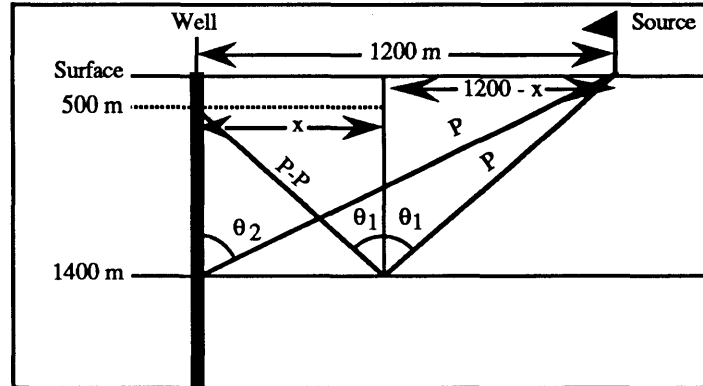


Figure 2.24 Geometry of synthetic model for P-P reflections at the 1400 m interface.

from Figure 2.24

$$\tan \theta_1 = \frac{1200 - x}{1400}, \quad 2.13$$

$$\tan \theta_1 = \frac{x}{900},$$

where x is the distance away from the borehole of the reflection point. Solving for θ_1 in equations 2.13, we get $x = 469$ m and $\theta_1 = 27.5^\circ$. At 1400 m depth, $\theta_2 = \tan^{-1} \frac{1200}{1400} = 41^\circ$. So, for P-P reflections at the first interface, the angle of incidence of the incoming P wave ranges between 27.5° and 41° . For the P-SV case, since the P-wave velocity is greater than the S-wave velocity, one would expect, according to Snell's law (Sheriff and Geldart, 1983), a larger angle for the 500 m receiver and 41° at the 1400 m receiver. Therefore, the angles of incidence for both P-P and P-SV reflections at the first interface range between 27.5° and 41° . In that range of angles of incidence in Figure 2.22, the reflection coefficients for P-SV reflections are two to three times larger than for the P-P reflections. This explains why the total amplitudes of the converted waves are much larger than the total amplitudes of the P-P reflections for the first reflector on the synthetic VSP sections. Similar arguments could be followed to explain the same phenomenon for the second interface (Figure 2.23) and the third interface (Figure 2.22).

2.5.2 Rolling Hills case

In the real data case, the presence of downgoing P and S waves and their associated multiples requires the implementation of a more sophisticated method of downgoing wavefield removal. Several methods have been proposed for the separation of downgoing and upgoing waves in VSP data including velocity filtering in the f-k (Embree et al., 1963; Christie et al., 1983) and τ -p domains (Moon et al., 1986; Mammo, 1987). The subtraction method of downgoing wavefield removal (Hardage, 1985) has been the most popular in the literature. In this scheme, the downgoing waves are enhanced and subtracted from the total wavefield to reveal the upgoing wavefield. The enhancement of the downgoing wavefield has been done in the past mostly by median filtering (Hardage, 1985; Stewart, 1985). In this thesis, the subtraction method is used to separate the downgoing and upgoing wavefields and the p-t decomposition method is used to enhance the downgoing wavefield.

The downgoing wavefield of the Rolling Hills data was enhanced using the p-t decomposition. After testing for the local window length which best decomposes the data at depths where the velocities change abruptly, a local window of 9-traces was used to decompose each panel into a range of slownesses from 0 to 1000×10^{-6} s/m which include all the downgoing waves. The semblance weighting was then applied to each of these decompositions and the middle trace in each panel was reconstructed by stacking across the range of positive slownesses yielding the downgoing wavefield. This was done for the vertical and radial components as shown in Figures 2.25 and 2.26. The downgoing wavefield has been enhanced while the upgoing wavefield has been suppressed. These downgoing wavefield sections were then subtracted from their respective total wavefield equivalents to yield the upgoing wavefields for the vertical and radial components shown in Figures 2.27 and 2.28. A muting has also been performed on Figures 2.25 to 2.28 so that all the sample points 0.08 second above the first breaks were set equal to zero. All the plots following and including Figure 2.27 have been scaled up to reveal the upgoing reflections which have lower amplitudes than the downgoing waves.

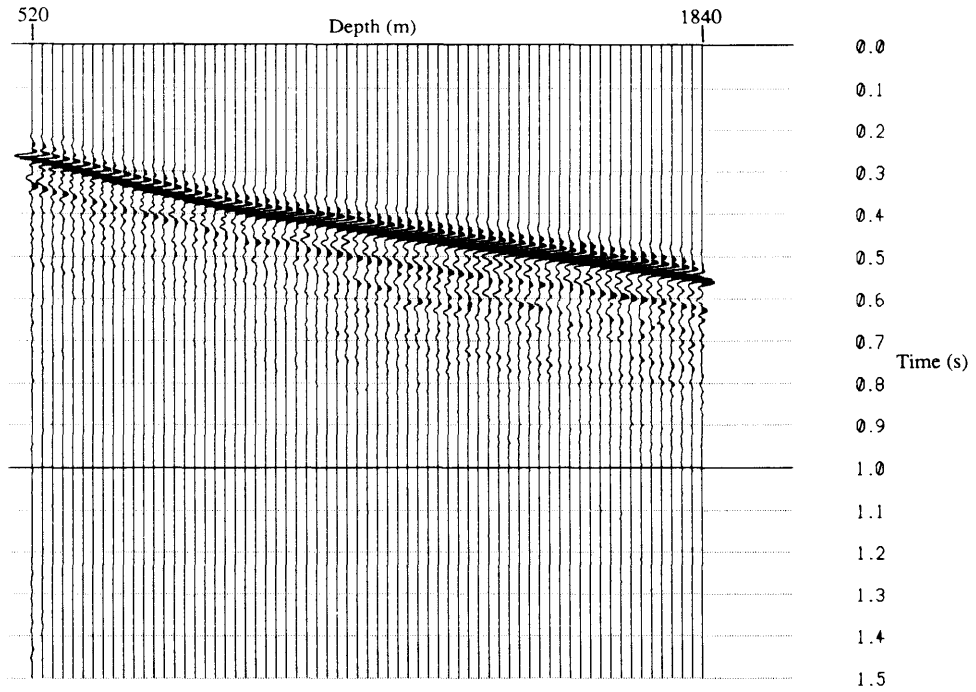


Figure 2.25 Vertical component of the downgoing wavefield for the Rolling Hills data set obtained through the p-t decomposition method.

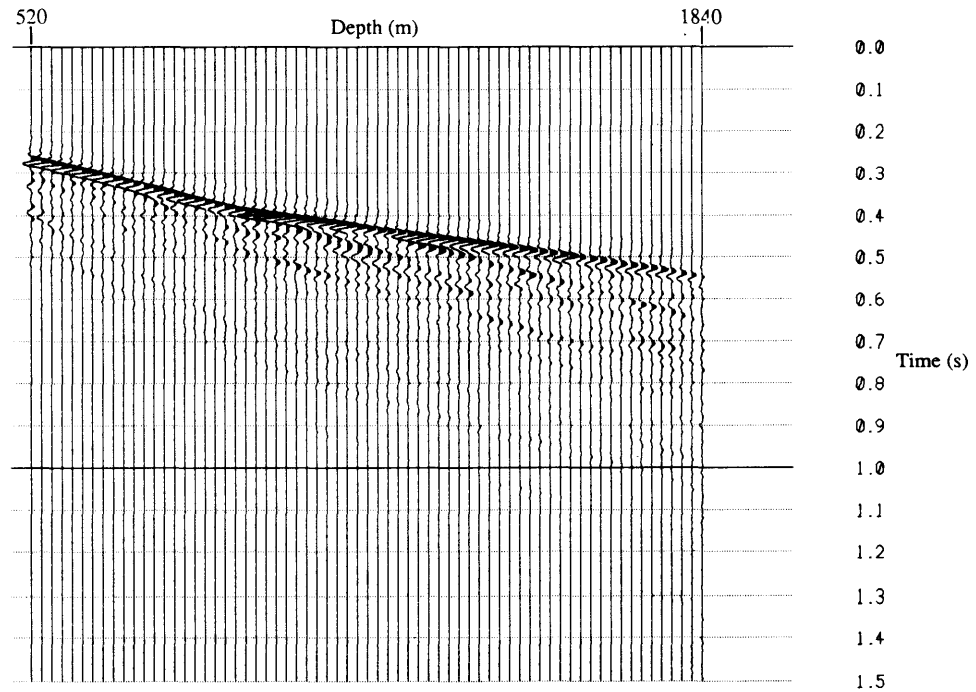


Figure 2.26 Radial component of the downgoing wavefield for the Rolling Hills data set obtained through the p-t decomposition method.

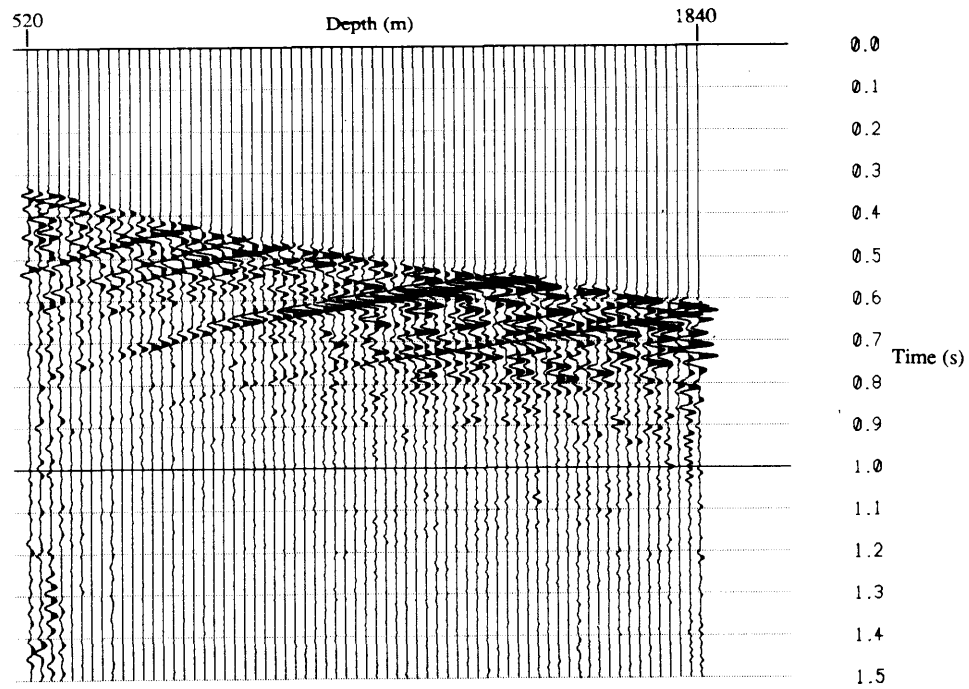


Figure 2.27 Vertical component of the upgoing wavefield for the Rolling Hills data set obtained by subtracting the downgoing wavefield in Figure 2.25 from the total wavefield on Figure 2.10.

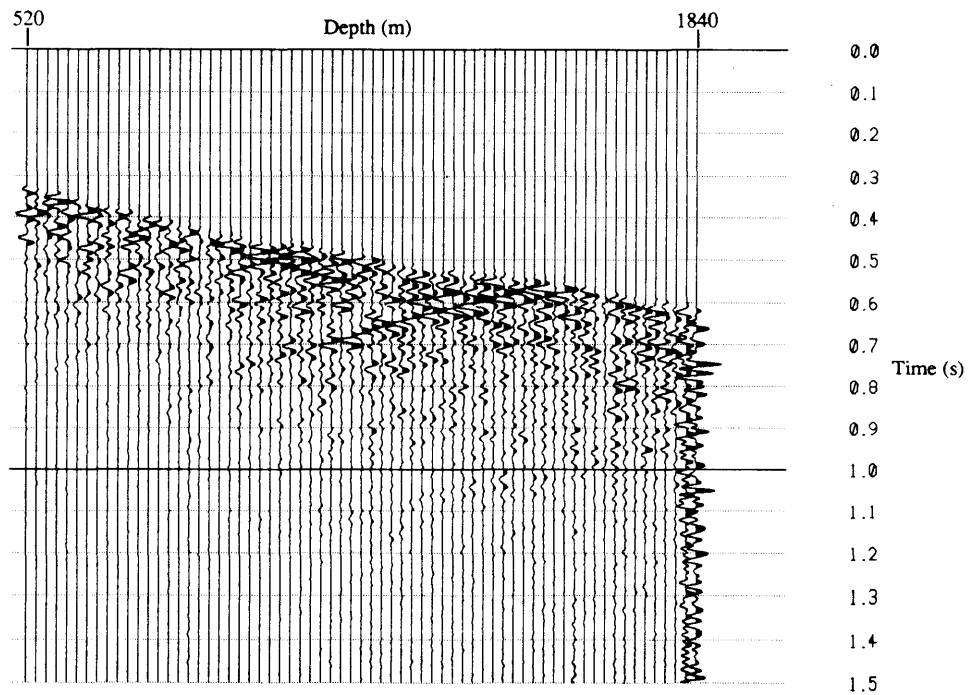


Figure 2.28 Radial component of the upgoing wavefield for the Rolling Hills data set obtained by subtracting the downgoing wavefield in Figure 2.26 from the total wavefield on Figure 2.11.

2.6 Velocity analysis

P- and S-wave velocities are needed later to separate the P and S waves and also to map the P-P and P-SV reflected waves to their reflection points. The first P breaks are used to perform a least-square inversion that yields the P-wave interval velocities in a manner similar to that of Stewart (1984). Similarly, if a direct downgoing S wave can be picked on the VSP data, it can be used to perform the same process to yield S-wave interval velocities as a function of depth. This was previously done on the Rolling Hills data set (Geis et al., 1989) and the resulting P- and S-wave velocities are shown in Figure 2.29. These velocities will be used later in the separation, mapping and inversion stages.

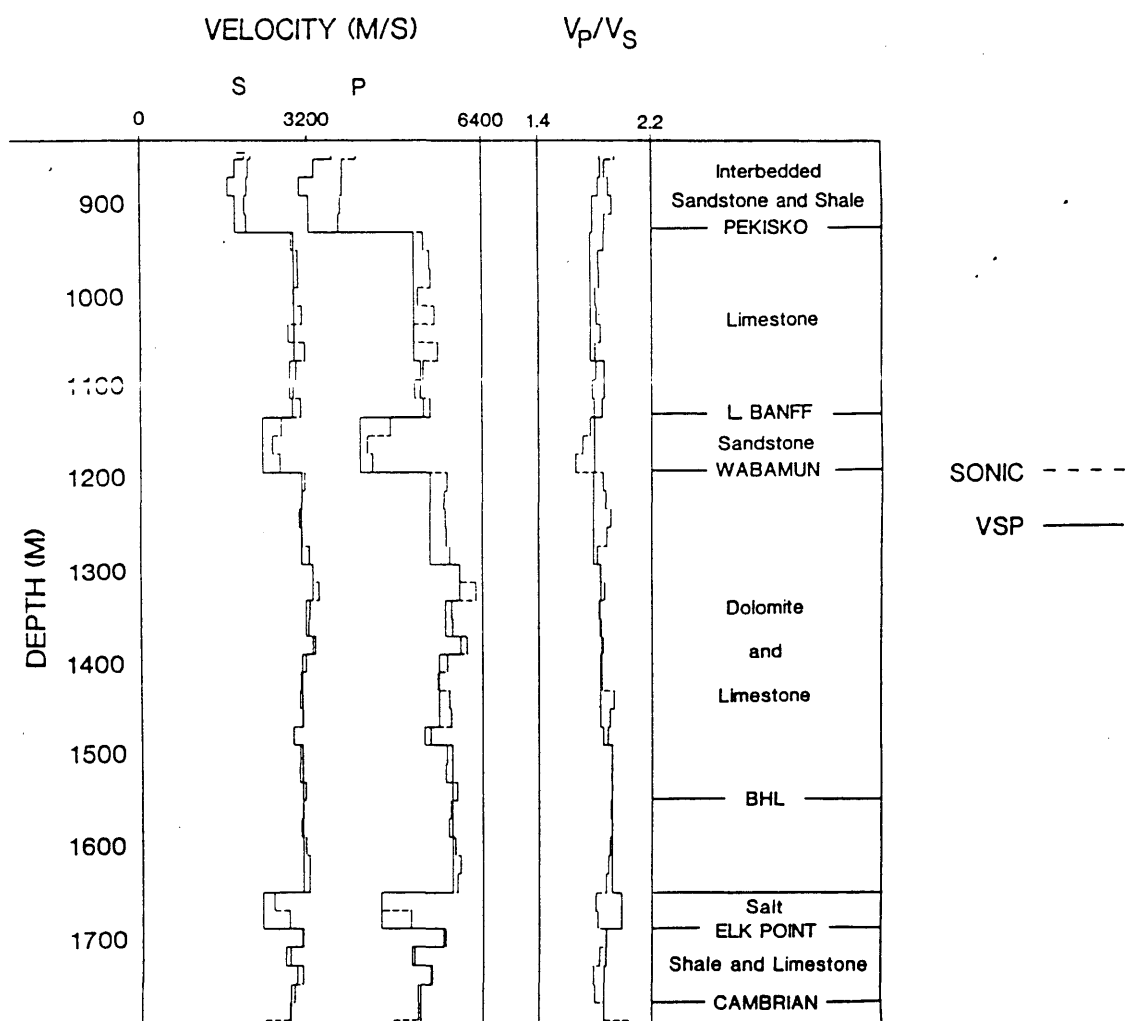


Figure 2.29 Interval velocities obtained from logs and through least-square inversions on the first P and S downgoing events on the Rolling Hills data set. Formations and lithologies are noted (from Geis et al., 1989).

2.7 Deconvolution

In VSP, the enhanced downgoing wavefield is used to design deconvolution operators that will attempt to shape the source seismic wavelet into a spike (Hardage, 1985). Again, the first downgoing P wavelets are used to calculate the deconvolution filters. The idea is to take the first P wavelets $x(t)$ (n elements), the input signal, and design a filter $f(t)$ (m elements) which will attempt to shape $x(t)$ into a desired output $z(t)$ - a spike in our case. The filters are designed by minimizing the square of the difference (J) between $z(t)$ and $y(t)$, the actual output obtained by convolving $x(t)$ with $f(t)$, in a least-square sense (Robinson and Treitel, 1980). The error J will depend on where the spike is located in $z(t)$. In attempting to estimate the optimum spike position that will give the minimum error, certain rules can be followed with the provision of sufficiently long filters (Robinson and Treitel, 1980).

1. The optimum spike position for a minimum-phase input signal $x(t)$ is the smallest possible delay, namely 0.
2. The optimum spike position for a maximum-phase input signal $x(t)$ is the largest possible delay, namely $m+n+1$.
3. The optimum spike position for a mixed phase input signal $x(t)$ is intermediate between the smallest and the largest possible delays.

This spiking deconvolution operation was performed on the vertical and radial components of the Rolling Hills data set using a subroutine from Robinson (1967). In order to minimize the calculation time of the deconvolution filters, the lag of the spike position in the desired output was set equal to the length of the input signal, namely, n elements. By doing so, the input signals were assumed to be mixed phase. The filters were designed using a time window that include the vector addition of the enhanced, first downgoing P waves (input signal) on the vertical and radial components in Figures 2.25 and 2.26. These filters were then applied to the upgoing wavefield traces shown in Figures 2.27 and 2.28. After testing for the optimal design and filter lengths, the filter length used was 0.120 s, and the input signal length was 0.3 s. The results are shown in Figures 2.30 and 2.31. The data are of higher frequency content as expected. Trace editing has also been carried out at this point to eliminate noisy traces. Traces belonging to the 520 to 580 m and 1820 to 1840 m depth levels have been filled with zeroes to nullify the high-amplitude, low-frequency noise present in these traces.

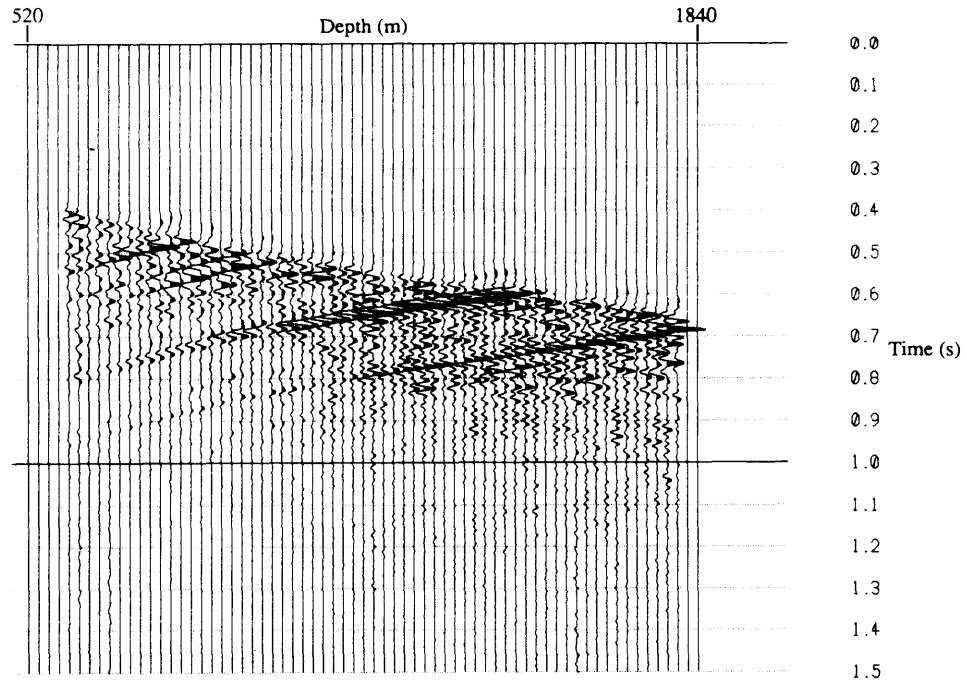


Figure 2.30 Deconvolved vertical component of the upgoing wavefield for the Rolling Hills data set.

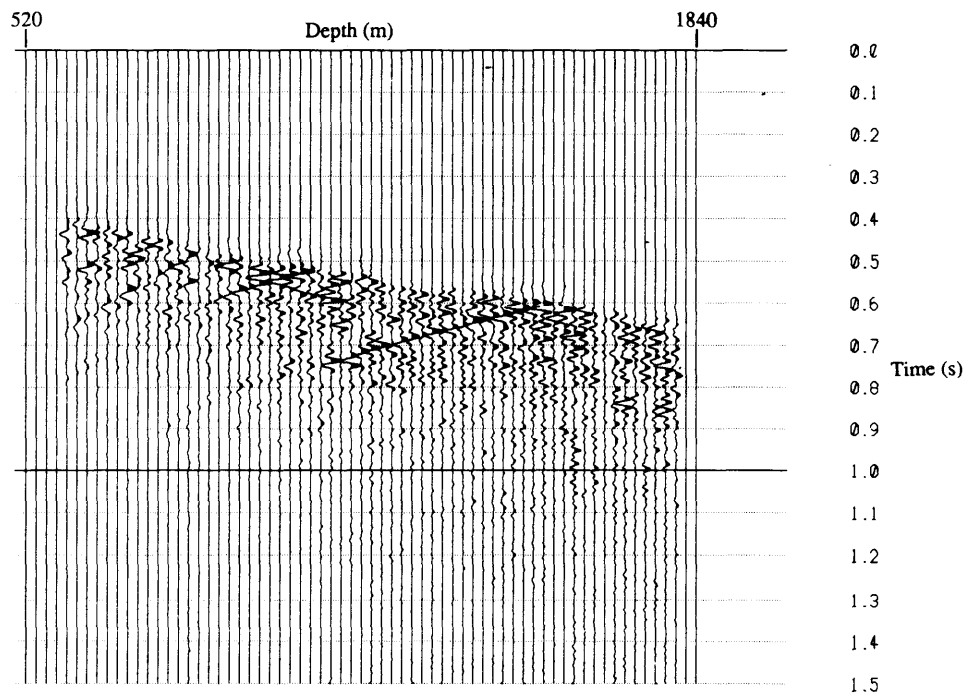


Figure 2.31 Deconvolved radial component of the upgoing wavefield for the Rolling Hills data set.

2.8 Time-variant exponential gain

As mentioned before, several physical processes have a major impact on the amplitude of a propagating wavefield and the amplitude must be compensated by the application of gain to the VSP data. Some of the physical processes that affect the amplitude of the propagating wavefield include spherical divergence or geometrical spreading (Newman, 1973), transmission losses, scattering and absorption caused by the removal of energy from the wavefield by frictional losses (Hardage, 1985). All of the processes affecting the amplitude of the propagating wavefield are compensated for in two steps; the first is trace equalization on the downgoing first breaks (Section 2.3), and the second is the time-variant exponential gain on the upgoing wavefield (Hardage, 1985).

The second step in gain recovery gives a time-variant gain of the exponential type starting at the first break of each trace. Again, in order to keep the polarization-angle relationship, the same gain must be applied to both vertical and radial components. The gain, $G(t)$, is applied to the raw amplitudes, $U(t)$, to produce their gained equivalents:

$$U_{\text{gained}}(t) = G(t) U(t), \quad 2.14$$

where $G(t)$ has the form:

$$G(t) = e^{\gamma t}, \quad 2.15$$

where γ is a constant. Since the data have already been trace-equalized on the first breaks, the starting time of the gain is always at the first breaks.

This idea was coded and, after testing, a value of $\gamma = 2.15$ was found to equalize the amplitude adequately in time. The optimal γ value was found by simply 'eye balling' the results obtained through different values of γ . The time-variant gain was applied to the deconvolved upgoing wavefields with the results shown in Figure 2.32 for the vertical component and Figure 2.33 for the radial component. The data, plotted with true relative amplitude, are now seen as having constant energy in time, and some downgoing energy can be seen as having leaked through the downgoing wavefield removal process. All the effects contributing to amplitude loss of the propagating wavefield have been removed by the application of the time-variant gain so that the final processes, such as modal separation, mapping and S-wave velocity inversion, can be applied to the data.

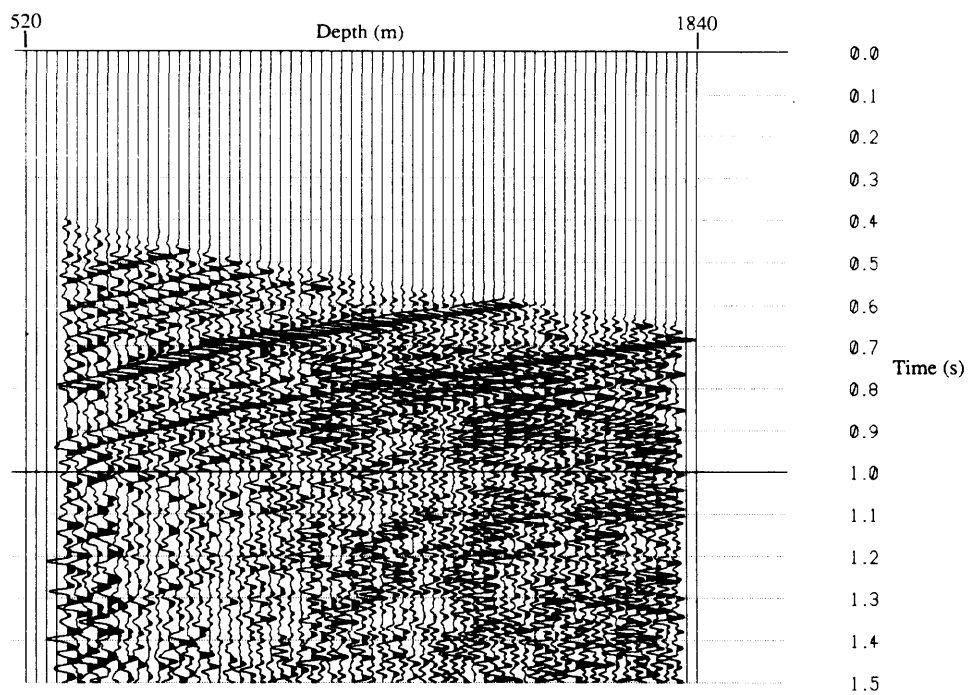


Figure 2.32 Deconvolved vertical component for the Rolling Hills data set (Figure 2.30) with time-variant gain applied.

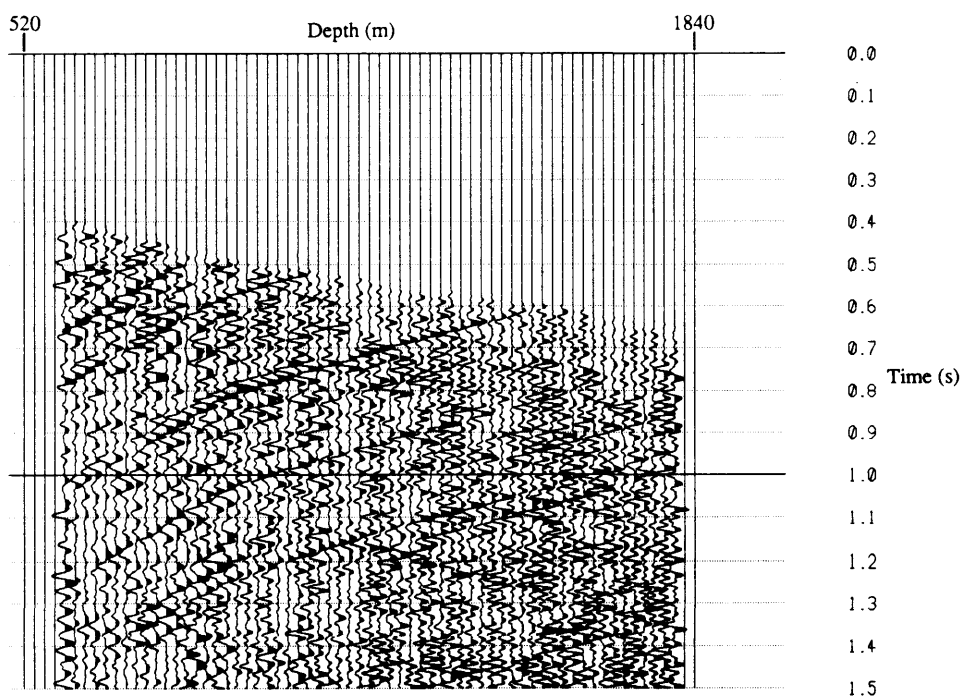


Figure 2.33 Deconvolved radial component for the Rolling Hills data set (Figure 2.31) with time-variant gain applied.

Chapter 3 - P-S wave mode separation

3.1 Introduction

The seismic wavefield recorded at the geophone contains a considerable amount of P and SV waves arriving at angles of incidence which may vary considerably in time and in depth (Chapter 1). Once the data have been processed up to the point where the gained, deconvolved upgoing wavefield has been obtained, the P-P and P-SV waves must be separated from the vertical and radial components to produce total P-P and total P-SV sections that can be used to map P-P and P-SV reflection points.

3.2 Theory

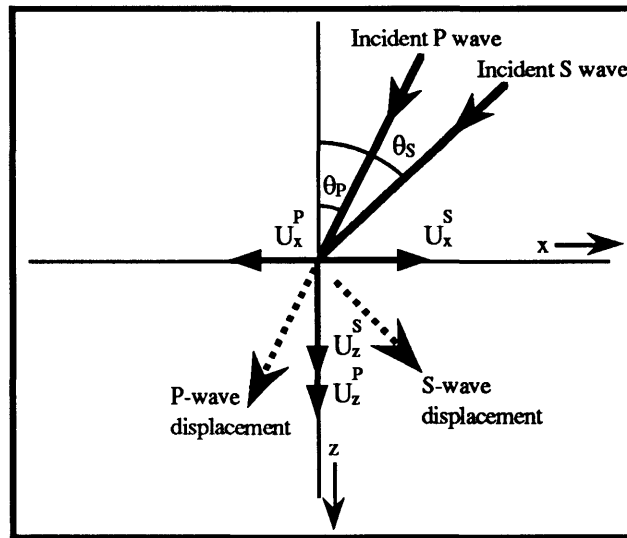


Figure 3.1 Particle displacement of an incident P or S wave (after Dankbaar, 1987).

Figure 3.1 shows the particle displacement of an incident P or S wave incident upon a vertical borehole - the z axis (after Dankbaar, 1987). From this diagram, the total displacement on the vertical ($U_z(t)$) and radial ($U_x(t)$) channels are

$$U_z(t) = U^P(t) \cos \theta_P(t) + U^S(t) \sin \theta_S(t),$$

$$U_x(t) = -U^P(t) \sin \theta_P(t) + U^S(t) \cos \theta_S(t),$$

3.1

where $U^P(t)$ and $U^S(t)$ are the P and SV wavefields respectively. These equations can be solved for $U^P(t)$ and $U^S(t)$ yielding

$$U^P(t) = \frac{U_z(t) \cos \theta_S(t) - U_x(t) \sin \theta_S(t)}{\sin \theta_P(t) \sin \theta_S(t) + \cos \theta_P(t) \cos \theta_S(t)},$$

$$U^S(t) = \frac{U_z(t) \sin \theta_P(t) + U_x(t) \cos \theta_P(t)}{\sin \theta_P(t) \sin \theta_S(t) + \cos \theta_P(t) \cos \theta_S(t)}.$$
3.2

Equations 3.2 could be used to separate P and SV waves in the depth-time domain (see Section 3.5.1) but this would involve calculating the angle of incidence of P and SV waves at each time point on the VSP traces. Instead, the plane-wave decomposition approach is used. Figure 3.2 pictures a plane wave incident upon a borehole. The

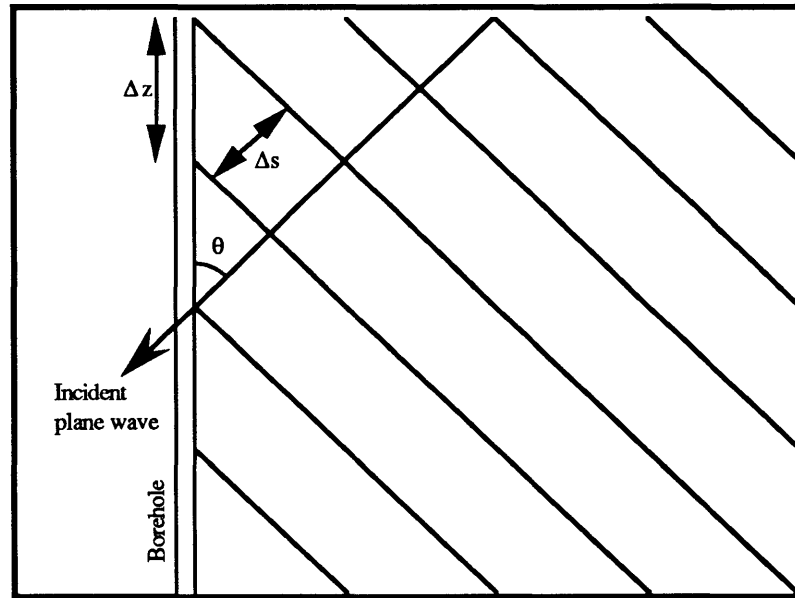


Figure 3.2 Plane wave incident upon a borehole.

wave travels a distance Δs in its direction of propagation in the same time period (Δt) that it travels a distance Δz along the vertical borehole. The apparent velocity of the plane wave along the borehole is $V_{ap} = \Delta z / \Delta t$ while the true velocity of the plane wave is $V_{tr} = \Delta s / \Delta t$. The angle of incidence of the plane wave (θ) is related to the true and apparent velocities by

$$\cos \theta = \frac{\Delta s}{\Delta z} = \frac{\Delta t V_{tr}}{\Delta t V_{ap}},$$

or

$$\cos \theta = \frac{V_{tr}}{V_{ap}}. \quad 3.3$$

Defining the vertical slowness as $p_z = 1 / V_{ap}$ and substituting into 3.3

$$\cos \theta = p_z V_{tr}. \quad 3.4$$

For the case of true P- and S-wave velocities (V_P and V_S), and letting $p \equiv p_z$ we get:

$$\begin{aligned} \cos \theta_P &= p V_P, \\ \cos \theta_S &= p V_S. \end{aligned} \quad 3.5$$

But then

$$\begin{aligned} \sin \theta_P &= \sqrt{1 - (p V_P)^2}, \\ \sin \theta_S &= \sqrt{1 - (p V_S)^2}. \end{aligned} \quad 3.6$$

Substituting equations 3.5 and 3.6 into equation 3.2 gives

$$U^P = U_z \left(\frac{p V_S}{Q} \right) + U_x \left(- \frac{\sqrt{1 - (p V_S)^2}}{Q} \right), \quad 3.7a$$

$$U^S = U_z \left(\frac{\sqrt{1 - (p V_P)^2}}{Q} \right) + U_x \left(\frac{p V_P}{Q} \right), \quad 3.7b$$

$$\text{where } Q = (p V_P) (p V_S) + \sqrt{1 - (p V_P)^2} \sqrt{1 - (p V_S)^2}.$$

Equations 3.7a and 3.7b give the separated P and S waves as a function of the vertical and radial components (U_z and U_x), the vertical slowness (p), and the P- and S-wave velocities (V_P and V_S). Equations 3.7a and 3.7b are equivalent to equations 3.2 when the filtering process is applied in the slowness domain, that is, when the vertical and radial components have previously been submitted to a plane-wave decomposition algorithm such as the two-dimensional Fourier transform or the τ - p transform.

3.3 Filter coefficients

In practice, the filtering operation is performed by transforming the vertical and radial components into the slowness domain (e.g. p-t domain or frequency-wavenumber domain) and applying the filter coefficients to each component. In the "pass-P" mode the decomposed vertical and radial components are filtered using 3.7a, stacked and inverse transformed back to the depth-time (z,t) domain. Similarly, in the "pass-S" mode, the decomposed components are filtered according to 3.7b, stacked and inverse transformed back to the z,t domain. The amplitude of the filter coefficients are determined by the vertical slowness p and the P and S velocities (V_P and V_S).

3.3.1 Raw filter coefficients

The raw filter coefficients (equations 3.7a-3.7b) are plotted as a function of vertical slowness in Figures 3.3 to 3.6 for an arbitrary set of velocities, namely, $V_P = 3000$ m/s and $V_S = 1500$ m/s. The vertical lines correspond to vertical slownesses of $|p| = 1/V_P$ and $|p| = 1/V_S$. For a P wave, a slowness of $1/V_P$ corresponds to a plane wave with an angle of incidence $\theta_P = 0^\circ$; similarly, for an S wave, a slowness of $1/V_S$ corresponds to a plane wave with an angle of incidence of $\theta_S = 0^\circ$. Therefore, the vertical lines in Figures 3.3 to 3.6 indicate the maximum slownesses of incident P and S waves.

Downgoing waves have, by definition, a positive slope on the VSP section (see Section 1.1) and thus will have positive vertical slownesses in the slowness domain. Similarly, upgoing reflected waves have a negative slope on the VSP section and will have negative slownesses in the slowness domain. For a deep reflector, the angle of incidence of the reflected wave will be near -180° and the reflection energy will be concentrated near the maximum slownesses, $-1/V_P$ for P waves and $-1/V_S$ for S waves.

The filter coefficients operate on the vertical and radial components by taking into account both the amplitude and the polarity (phase) of the P and S waves. Figure 3.1 shows the components of displacement of a downgoing P or S wave. A downgoing P wave will have displacements on the vertical and radial components that are opposite in polarity. By investigating the filter coefficients for the pass-P mode (Figures 3.3 and 3.4), it becomes clear that the same downgoing P wave, having a positive slowness, is reconstructed by multiplying the two components with coefficients of opposite signs and summing them. In this fashion, the full P-wave displacement is recovered by constructive

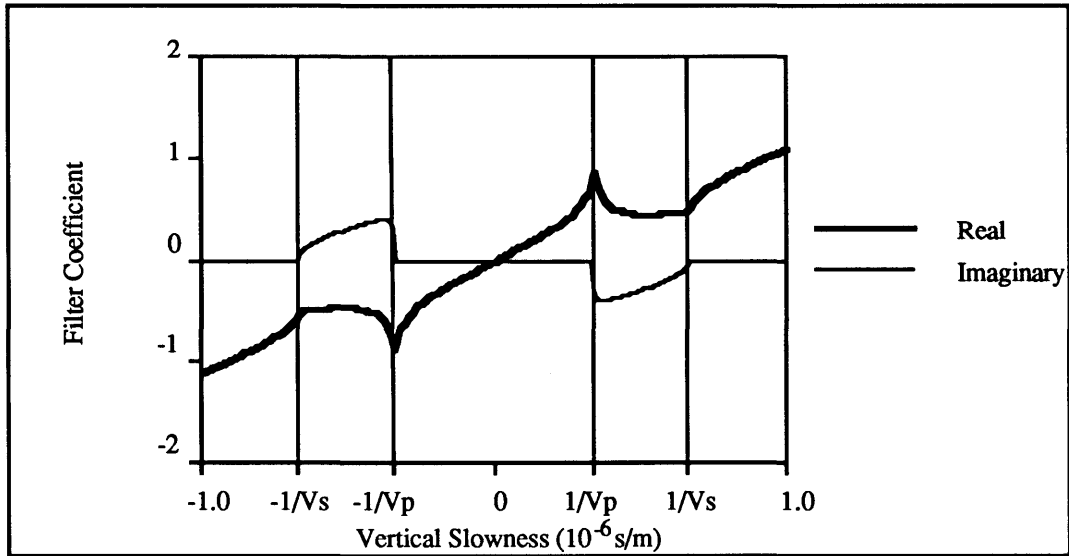


Figure 3.3 Filter coefficient for pass-P mode, vertical component.

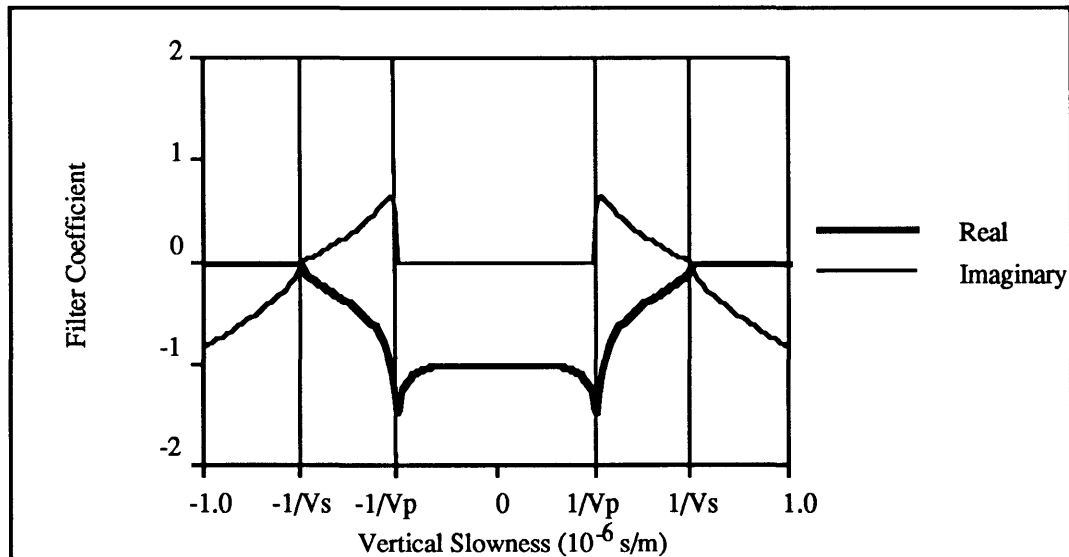


Figure 3.4 Filter coefficient for pass-P mode, radial component.

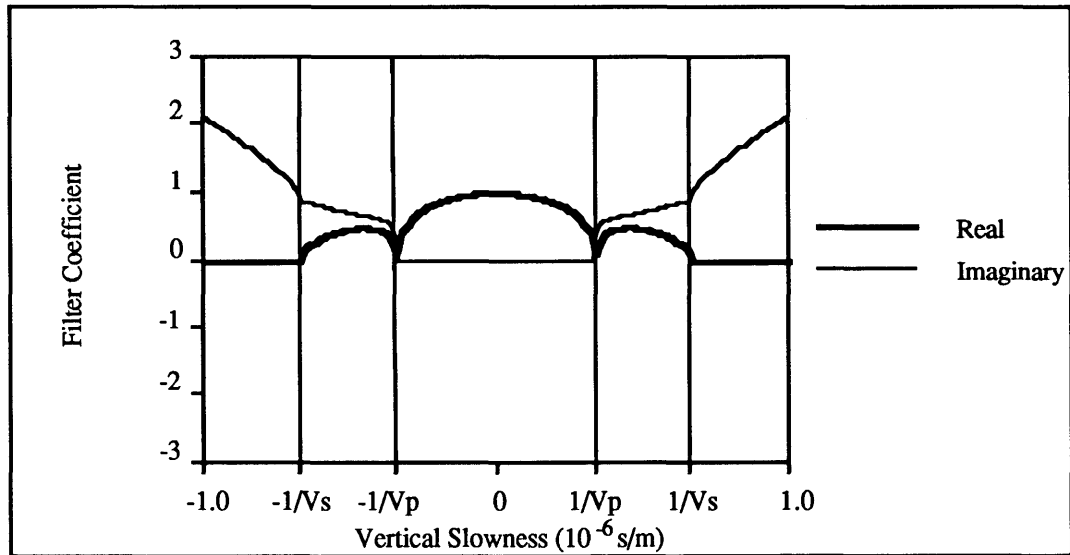


Figure 3.5 Filter coefficient for pass-S mode, vertical component.

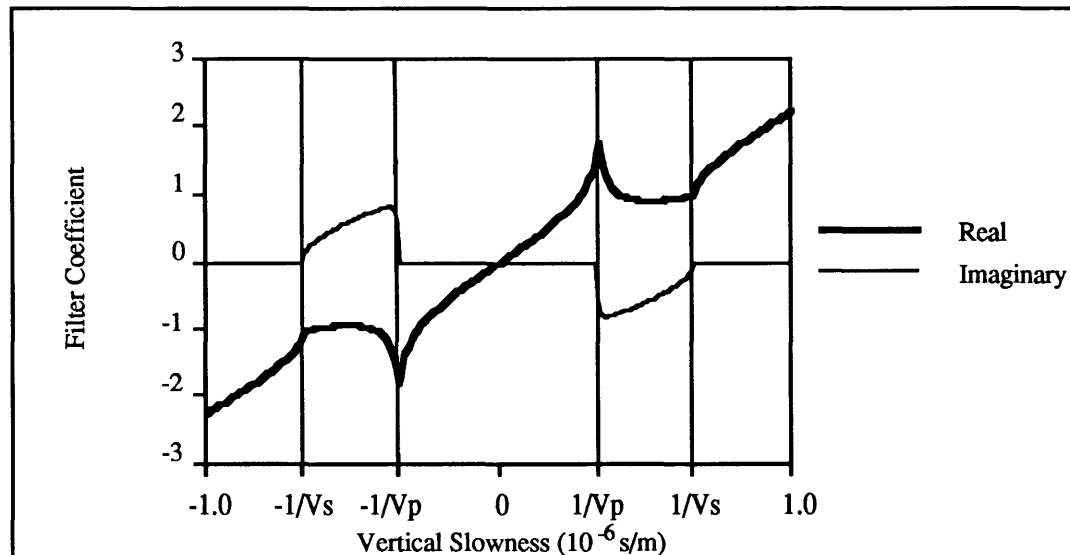


Figure 3.6 Filter coefficient for pass-S mode, radial component.

interference of the P-wave components on the vertical and radial channels. In a similar way, a downgoing S wave, whose displacements have the same sign on the vertical and radial channels, can be reconstructed by multiplying the two components with coefficients (Figures 3.5 and 3.6) of similar signs. This will not only enhance the downgoing S wave through constructive interference but will also tend to reject the downgoing P wave through destructive interference.

3.3.2 Instabilities

A few features of the filter coefficients in Figures 3.3 to 3.6 are notable. In the pass-P mode, the filter coefficients peak at slowness $|p| = 1/V_P$. This is not a problem since the intent is to pass P waves and reject S waves. In the pass-S mode on the vertical component, the filter coefficients go to zero at $|p| = 1/V_P$. This is no problem since the intent is to suppress P waves and pass S waves. In the pass-S mode mode on the radial component, the filter coefficients peak at $|p| = 1/V_P$. This is not seen as a serious problem and has shown (from observation) not to cause any serious instabilities in testing the algorithm.

The filter coefficients tend to reach rather high values at $|p| > 1/V_S$. This can be seen in the pass-P mode for the real part of the filter coefficients on the vertical component, and the imaginary part of the filter coefficients on the radial component. In the pass-S mode, this 'blowing up' of the filter coefficients can be observed on the imaginary part of the coefficients on the vertical component, and on the real part of the coefficients on the radial component. However, no P waves are expected for slownesses with $|p| > 1/V_P$, and the filter coefficients can be tapered to zero for $|p| > 1/V_P$ in the pass-P mode. Similarly, since no S waves are expected beyond slownesses $|p| > 1/V_S$, the filter coefficients can be tapered to zero for $|p| > 1/V_S$ in the pass-S mode in order to prevent the occurrence of instabilities for those slownesses.

3.3.3 Tapered filter coefficients

The raw filter coefficients were tapered to zero for $|p| > 1/V_P$ in the pass-P mode and for $|p| > 1/V_S$ in the pass-S mode as depicted in Figures 3.7 to 3.10. The tapering function used was a cosine function:

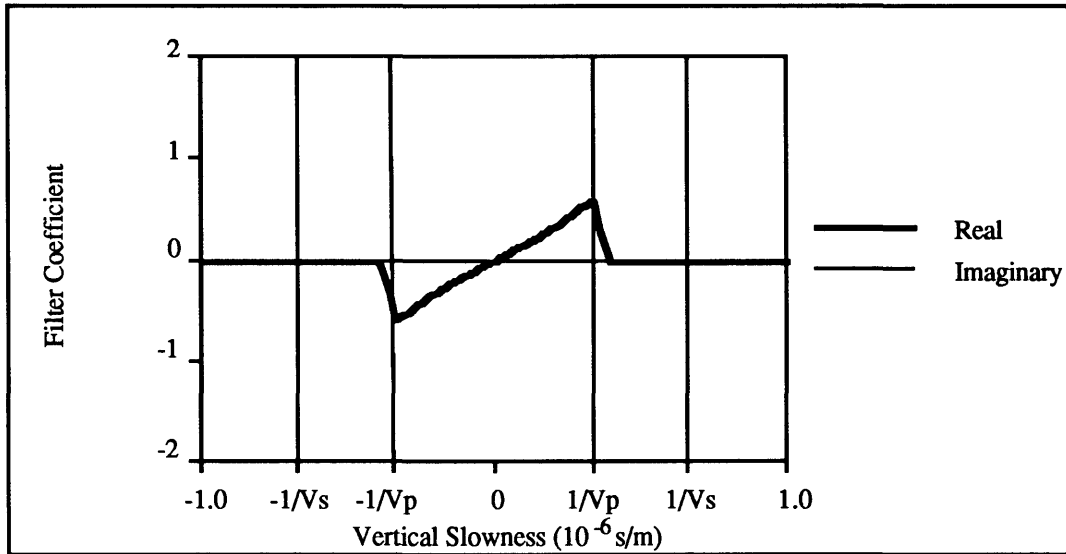


Figure 3.7 Tapered filter coefficient for pass-P mode, vertical component.

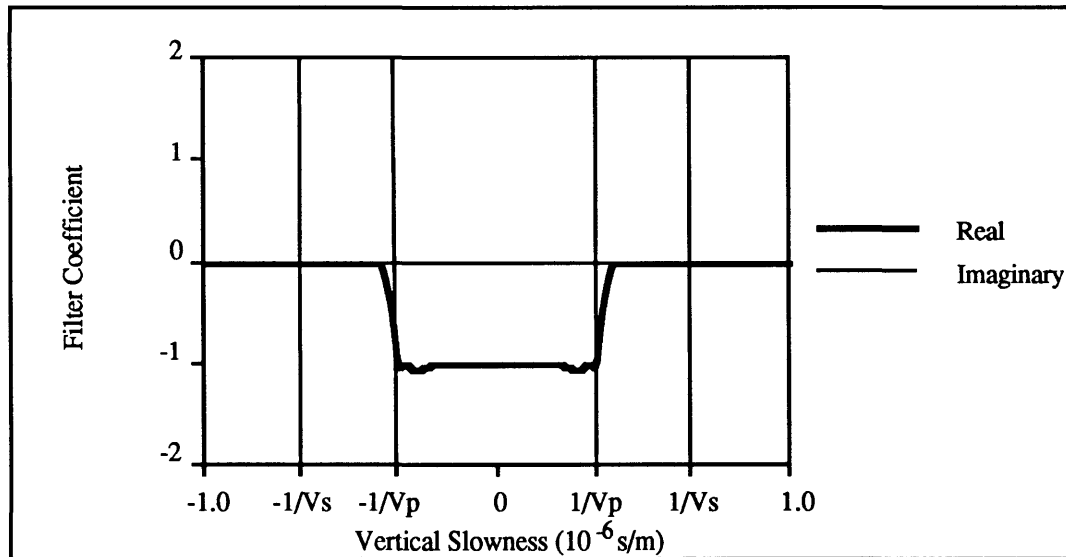


Figure 3.8 Tapered filter coefficient for pass-P mode, radial component.

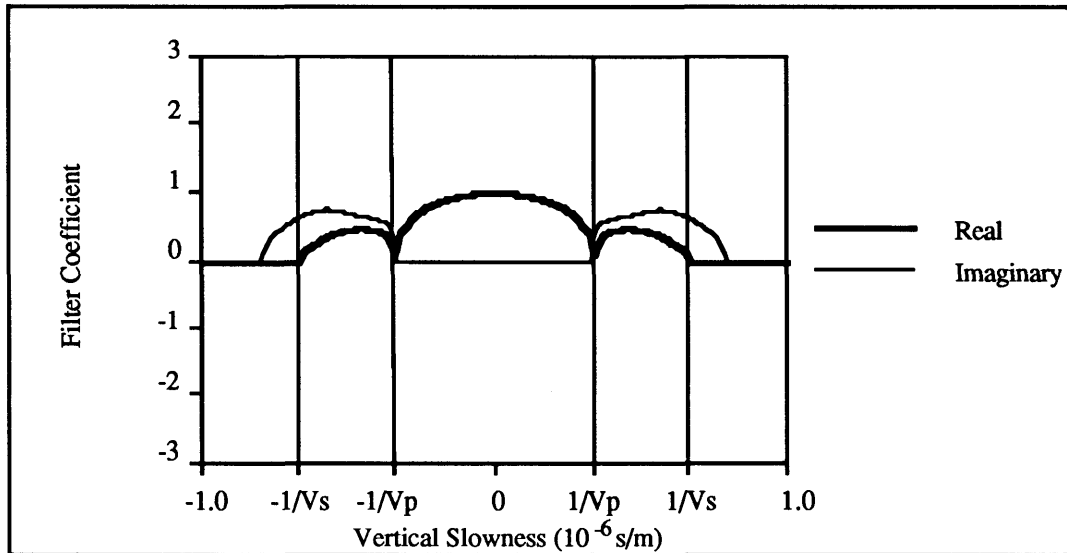


Figure 3.9 Tapered filter coefficient for pass-S mode, vertical component.

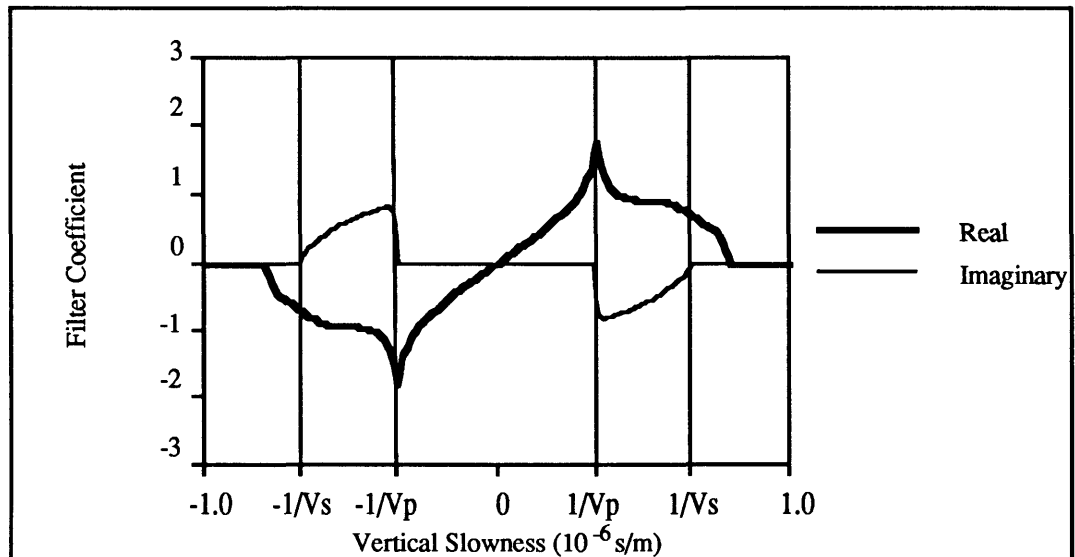


Figure 3.10 Tapered filter coefficient for pass-S mode, radial component.

$$\cos \left[\frac{(|p| - a) \pi}{(b - a) 2} \right] \quad a \leq |p| \leq b, \quad 3.8$$

where $a = \frac{0.8}{V_P}$, $b = \frac{1.2}{V_P}$ in the pass P mode,

and $a = \frac{0.8}{V_S}$, $b = \frac{1.2}{V_S}$ in the pass S mode.

3.3.4 Polarity consideration

The filter coefficients derived above were generated assuming the geophone configuration shown in Figure 3.1, namely, that the vertical and radial geophones are oriented such that a downgoing compressional wave gets recorded as a positive particle displacement on the vertical geophone and as a negative particle displacement on the radial geophone. This is not the case of the field VSP, as shown in Figures 2.25 and 2.26, where the initial particle displacement is negative on the vertical component and positive on the radial component. In fact, the first arrival wavelet on the above two figures is not zero-phase as expected of Vibroseis data but resembles more a 90° wavelet with the energy more or less equally partitioned between a peak and its associated trough. This is in contrast with the downgoing wave on the synthetic data, Figures 2.17 and 2.18, which is observed to be zero-phase; its maximum particle displacement, however, is definitely negative, a trough, on the vertical component and positive, a peak, on the radial component. These observations indicate that the geophone orientation for both the field and synthetic data is opposite to the one shown in Figure 3.1, and that is: the vertical and radial geophones are oriented such that a downgoing compressional wave gets recorded as a negative particle displacement on the vertical geophone and as a positive particle displacement on the radial geophone.

The above observation merely changes the sign of every term on the right-hand side of equations 3.1, 3.2, 3.7a and 3.7b which, in turn, changes the sign of the real and imaginary parts of each filter coefficients shown in Figures 3.3 to 3.10. For instance, a downgoing P wave, positive in slowness, is reconstructed by taking its vertical component, negative in polarity, and multiplying it with the filter coefficients shown in Figure 3.7 with their signs reversed, negative in sign. This multiplication would yield a wavelet of positive polarity. This same exercise is performed for the radial component of the downgoing P wave and the filter coefficients shown in Figure 3.8 reversed in sign yielding also a wavelet of positive polarity. The two filtered components are then stacked

to produce the reconstructed downgoing P wave with its correct positive polarity. This polarity convention is taken into consideration whenever references are made to equations 3.1, 3.2, 3.7a and 3.7b and Figures 3.3 to 3.10 in future sections of this thesis.

3.4 Assumptions

It is important to note that a few assumptions have been made for the application of the P-S separation operation. First, it has been assumed that the radial component lies in the sagittal plane. This is realistic for the synthetic case where the geological interfaces are horizontal and where the ray-tracing program automatically makes the radial component such that it is oriented in the sagittal plane. In the real VSP case however, the horizontal rotation algorithm (Section 2.2) assumes that the vertical source-receiver plane and the sagittal plane are identical. This is only true if the geological interfaces are horizontal or dipping in the source-receiver direction, and the material through which the wavefield is propagating is isotropic, namely that there are no anisotropic layers that may rotate the polarization vector of the propagating P- and SV-waves. These conditions are assumed to be met in the Rolling Hills case (Geis et al., 1989).

In deriving the filter coefficients for the modal separation process, the actual displacement vectors of the P and S waves were considered at the geophone's location. In doing so, it has been assumed that the interference between the propagating wavefield and the recording surface (the borehole) is insignificant. Lee (1987) showed that in order for this to be true for elastic waves, the relation

$$\frac{2a}{\lambda} < 0.025 \quad 3.9$$

must be satisfied, where a is the diameter of the borehole and λ is the shortest wavelength of interest in the data. The highest frequency present in the data is 100 Hz (Section 1.4.2) and the lowest velocity present is the S-wave velocity $V_S = 1500$ m/s above the 935 m depth (Section 2.6), yielding a minimum wavelength of $\lambda = 15$ m. This yields a maximum borehole diameter of $a = 0.1875$ m. This is above the 0.1 m standard for borehole diameter and, therefore, the interference between the propagating wavefield and the borehole can be neglected.

V_P and V_S are also assumed to be constant over the region of transformation during the filtering process. In the global case, that is when all the VSP traces are used in the slowness decomposition process, this assumption is not generally true as large variations of P- and S-wave velocities along the borehole are often the case in VSP. However, in the local case, that is when only a few traces at a time (local window) are used in the slowness decomposition and when the filtering process is performed separately for each local window, a different set of velocities can be used for each local window. This is a definite advantage over the global method as, again, in situ velocity will often vary.

The coupling of the geophone with the borehole is assumed not to vary with depth. Strong amplitude variations between adjacent traces in a VSP section may cause a smearing of energy when a slowness decomposition is performed. To prevent this, the traces should be equalized as was done in Section 2.3.

The vertical and radial components should also be calibrated. This can be checked by calculating the angles of incidence of the downgoing P wave at each geophone location from the first P breaks on the vertical and radial components, and comparing them with some previously calculated model-based (ray-traced) angles of incidence. If the two angles do not match, a constant factor can be calculated and applied to either the vertical or radial VSP section to account for the lack of calibration between the two components.

3.5 Generalized application possibilities

The P-S separation process can be performed in several domains. The actual theoretical and practical details of the filtering operation were first presented by Dankbaar (1985) for the surface seismic case. Foster and Gaiser (1986) performed the separation on VSP data using the generalized Radon transform (τ - p) as a mean of slowness decomposition. Dankbaar (1987) performed the same operation in the frequency-wavenumber (f - k) domain using the two-dimensional Fourier transform. Dillon et al. (1988) separated the P and S waves using a localized frequency-slowness (f - p) approach. In all three of these cases, the filter coefficients discussed in Section 3.3 were used in the separation process. The filtering operation can also be performed in the depth-time (z - t) domain as will be discussed shortly. In this thesis however, a slowness-time (p - t) decomposition was used to transform the VSP data into the slowness domain and the results are compared with the results obtained when a two-dimensional Fourier transform is

used for plane-wave decomposition. The following four sections give a brief overview of the four methods of application of the P-S wave separation of VSP data.

3.5.1 Application in the z-t domain

As mentioned in Section 3.2, the filter coefficients in equations 3.2, which give the separated P and S waves as a function of angles of incidence, could be used to perform the separation operation in the z -t domain. In doing so, the angles of incidence of P and SV waves (θ_P and θ_S) would have to be calculated at each time point for every depth level (trace) on the VSP section. This would involve building a model approximating the geology in the area of the VSP and ray-tracing through it to calculate θ_P and θ_S for each time point on every VSP trace.

The filter coefficients in equations 3.7a and 3.7b, which give the separated P and S waves as a function of V_P , V_S and vertical slowness, could also be used to perform the separation of P and S waves in the z-t domain. Again, a model would have to be constructed and ray-traced to calculate the P- and S-wave slownesses (apparent velocities on the vertical borehole) at each time point on the VSP traces. These two rather tedious processes are not very attractive mainly because of the lengthy amount of work involved in calculating the angles of incidence or vertical slownesses at each time point on the VSP traces.

3.5.2 Application in the τ -p domain

The P-S filtering operation can be performed on VSP data that have been transformed into the τ -p domain. First the vertical and radial components, $U_z(z,t)$ and $U_x(z,t)$, are forward transformed in the τ -p domain (Claerbout, 1985)

$$U(\tau,p) = \int_{z_0}^{z_1} U(z,\tau+pz) dz, \quad 3.10$$

where p is the vertical slowness - or slope - (see Sections 2.4.1 and 2.5.1), τ is the time at which a given slope p projects to zero depth, and z_0 and z_1 are the lower and upper limits of the range of geophone depth levels present in the VSP. The τ -p transform maps an event with a given slope in the z-t domain to a point at that slope (p) and at a time (τ) where

the event projects at depth $z = 0$. In practice, dipping events are not constrained to a single point in the τ - p domain but rather appear for a range of time and slowness values because of the wave nature of the propagating seismic wavefield. Because of this, a given event on a VSP section will be smeared in the τ - p domain over a range of slownesses (p) and times (τ).

Once the vertical and radial components have been transformed into the τ - p domain, they are filtered using the real parts of the complex filter coefficients discussed in Section 3.3.3 to produce total P- and total S-wave sections, $U^P(\tau,p)$ and $U^S(\tau,p)$. These are then transformed back into the z - t domain, using the inverse τ - p transform

$$U(z,t) = \int_{p_0}^{p_1} \frac{d}{dt} H \{U(\tau-pz,p)\} dp, \quad 3.11$$

where a time derivative (d/dt) and a Hilbert transform (H) have to be included in the inverse transform to make it exact (Foster and Gaiser, 1986), and p_0 and p_1 is the range of slownesses used in the forward transform.

The filtering operation discussed above is a global approach to the problem, that is, the whole VSP sections are transformed into the τ - p domain before being filtered. The main disadvantage to this global approach lies in the fact that the data have to be filtered using a constant set of P and S velocities. Foster and Gaiser (1986) solve this problem by separating the P and S waves as the vertical and radial components are being forward transformed into the τ - p domain:

$$\psi(\tau,p) = \int_{z_0}^{z_1} A W(z,t+pz) dz, \quad 3.12$$

where

$$\psi(\tau,p) = \begin{bmatrix} U^P(\tau,p) \\ U^S(\tau,p) \end{bmatrix} \quad 3.13$$

is the vector containing the slant-stacked separated P and S wavefields,

$$W = \begin{bmatrix} U_z(z,t) \\ U_x(z,t) \end{bmatrix} \quad 3.14$$

is the originally recorded data,

$$A = \begin{bmatrix} V_P(z_i) p & \sqrt{1 - (V_S(z_i) p)^2} \\ -\sqrt{1 - (V_P(z_i) p)^2} & V_S(z_i) p \end{bmatrix} \quad 3.15$$

is the rotation matrix that performs the P-S separation as the data are being slant-stacked, and z_0 and z_1 are as in equation 3.10. The matrix A is thought of as a rotation matrix because it rotates the data to their proper polarization angle at the receiver location as the data are being slant-stacked across a depth z_i (Foster and Gaiser, 1986). In this fashion, a different set of P and S velocities can be used for each depth level (trace) in the VSP section. The data are then inverse-transformed

$$Q(z,t) = \int_{p_0}^{p_1} \frac{d}{dt} H \{ \psi(\tau - pz, p) \} dp, \quad 3.16$$

where

$$Q(z,t) = \begin{bmatrix} U^P(z,t) \\ U^S(z,t) \end{bmatrix} \quad 3.17$$

is the vector containing the separated seismic wavefield, and p_0 , p_1 , $\frac{d}{dt}$ and H are as in equation 3.11.

3.5.3 Application in the f-k domain

Dankbaar (1987) performs the P-S separation in the f-k domain. The vertical and radial components are first transformed into the f-k domain using the forward two-dimensional (2-D) Fourier transform, for example

$$U_x(f,k) = \int_0^{t_0} \int_{z_0}^{z_1} U_x(z,t) e^{2\pi i(ft - kz)} dz dt, \quad 3.18$$

where z_0 and z_1 are the lower and upper limits of the geophone depth levels in the VSP and t_0 is the maximum time. The filtering operation is then performed using the complex filter coefficients shown in Figures 3.7 to 3.10 where the vertical slowness $p = k/f$. The total P and S sections, $U^P(f,k)$ and $U^S(f,k)$, are then inverse transformed back into the z,t domain to give the total P and S wavefields in the $z-t$ domain e. g.,

$$U^P(z,t) = \int_{-f_N}^{f_N} \int_{-k_N}^{k_N} U^P(f,k) e^{-2\pi i(ft - kz)} dk df, \quad 3.19$$

where $k_N = \frac{1}{2 \Delta x}$ is the Nyquist wavenumber, Δx being the geophone spacing, and $f_N = \frac{1}{2 \Delta t}$ is the Nyquist frequency, Δt being the temporal sampling interval.

This is also a global approach to the separation process where a constant set of P and S velocities have to be used over the full depth range that was used in the 2-D Fourier transform. Dankbaar (1987) has found that variations of up to 25% between the P and S velocities used in the filtering process and the true P and S velocities along the borehole give acceptable results. Furthermore, if the P and S velocities vary by more than 25% over the depths of the geophone locations, the VSP sections can be split into regions or depth ranges within which the velocity variations are less than 25%. These depth ranges can then be filtered separately and later stacked together to produce a fully separated seismic wavefield.

3.5.4 Application in the f - p domain

Dillon et al. (1988) perform the same kind of P-S separation in the localized frequency-slowness (f - p) domain. The filtering operation is performed by partitioning the data into panels, each of which containing an odd number of traces equal to the window length used in the filtering process. The center of each panel corresponds to an input trace and there are as many panels as there are input traces. Each corresponding panel on the vertical and radial components is transformed into the f - p space in two steps: 1. In the z - t domain, the slant-stacks of the data are projected onto the center trace of the window; 2. Each of the slant-stacks are transformed into the frequency domain. Mathematically, for the continuous case, this takes the form

$$U(f,p) = \int_0^{t_0} \int_{z_0}^{z_1} U(z,t+zp) e^{2\pi i f t} dz dt, \quad 3.20$$

where z_0 and z_1 are the depth level limits of the panel being processed and t_0 is the maximum time.

The complex filter coefficients in equations 3.7 are then used to separate the P and S waves in f-p space, and these data are then inverse-transformed to a center trace estimate in the frequency domain by integrating over the range of slownesses p, namely p_0 and p_1

$$U'(f) = \int_{p_0}^{p_1} U(f,p) dp, \quad 3.21$$

where $U'(f)$ is the frequency equivalent of the center trace of the local window being filtered. Equation 3.21 is not an exact transform as was seen in Section 2.4.1 (Stewart, 1989a). The time domain filtered traces, $\tilde{U}(t)$, are obtained by inverse transforming the frequency traces into the time domain

$$\tilde{U}(t) = \frac{1}{2\pi} \int_{-f_N}^{f_N} U'(f) e^{-2\pi i f t} df, \quad 3.22$$

where f_N is the Nyquist frequency defined in equation 3.19. This process is repeated for each panel on the VSP section. The main advantage of this localized approach is that a different set of P and S velocities can be used for each panel, making the separation process more accurate than the global approach.

3.6 Application in the p-t domain

The P-S separation discussed in Sections 3.2 to 3.4 was applied to the synthetic and real VSP data sets using the p-t decomposition method (Cheadle, 1988). In each case the filtering process was performed by decomposing corresponding panels on the vertical and radial components into the p-t domain, applying the semblance weighting (Section 2.4.2) to each decomposition, applying the real part of the filter coefficients shown in Figures 3.7 to 3.10 to each semblance-weighted decomposition and stacking across the p range to produce a single set of pass-P and pass-S traces for each panel. This process was

repeated using different sets of panels (vertical and radial) for each depth level resulting in a total pass-P and a total pass-S section for each of the VSP data sets.

3.6.1 Synthetic application

Figures 2.19 and 2.20 show the vertical and radial components of the synthetic data set with the first breaks muted. P-P and P-SV reflections are present on both components for the three interfaces. The raw p-t decompositions for the 980-meter trace are shown in Figures 3.11 (vertical component) and 3.12 (radial component). Each event can be correlated to the events on the original sections. The P-P and P-SV events are separated in the p-t domain because they have two distinct, separate slownesses. However, the smearing of each event is serious; the P-P and P-SV events have a slowness range where they overlap. The semblance-weighted p-t decompositions are depicted in Figures 3.13 (vertical component) and 3.14 (radial component). The semblance weighting has enhanced the areas of high coherency in the p-t domain to the point where the P-P and P-SV events are well separated across the slowness range, i.e. there is no slowness overlap between the P-P and the P-SV events.

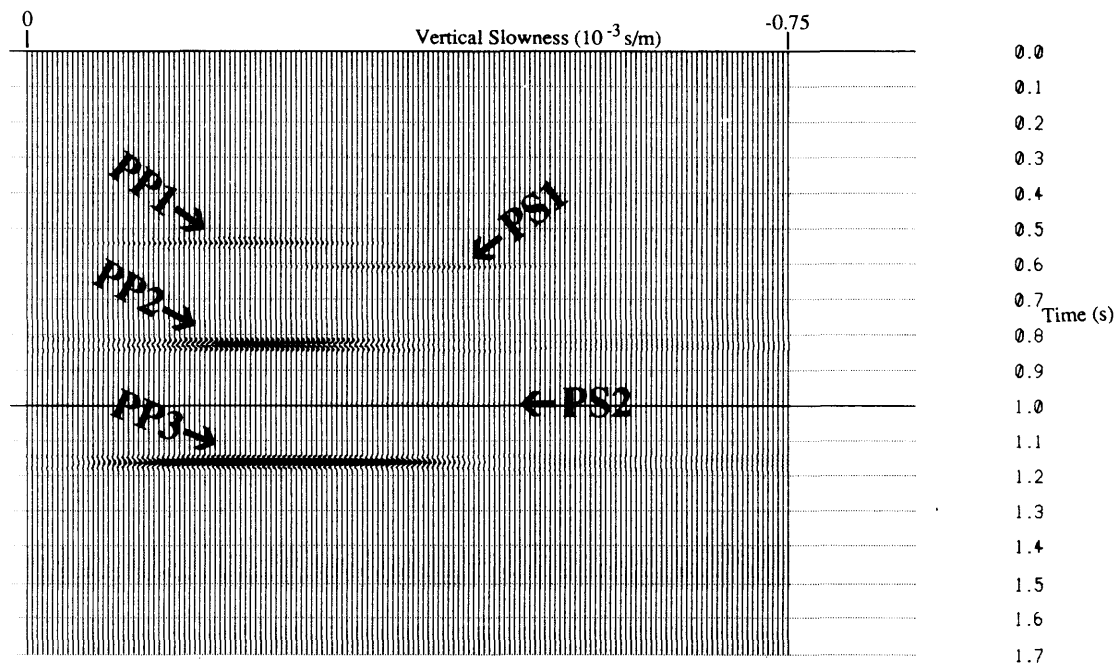


Figure 3.11 Raw p-t decomposition of the 9-trace local window centered on the 980-meter trace of the vertical component of the upgoing wavefield for the synthetic data set shown in Figure 2.19.

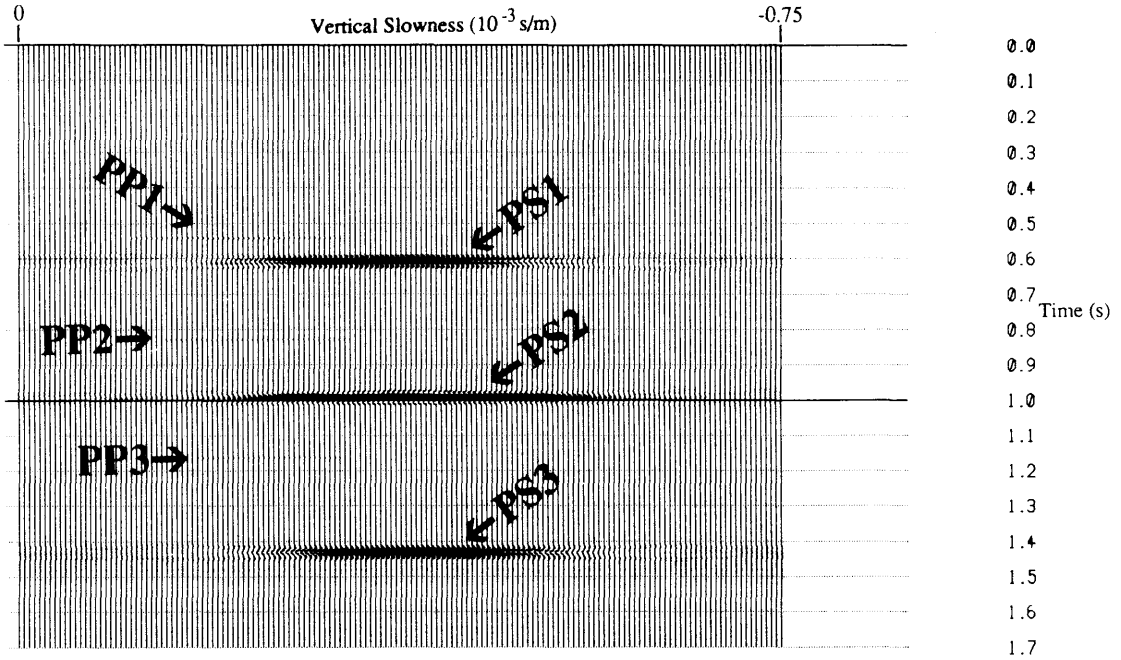


Figure 3.12 Raw p-t decomposition of the 9-trace local window centered on the 980-meter trace of the radial component of the upgoing wavefield for the synthetic data set shown in Figure 2.20.

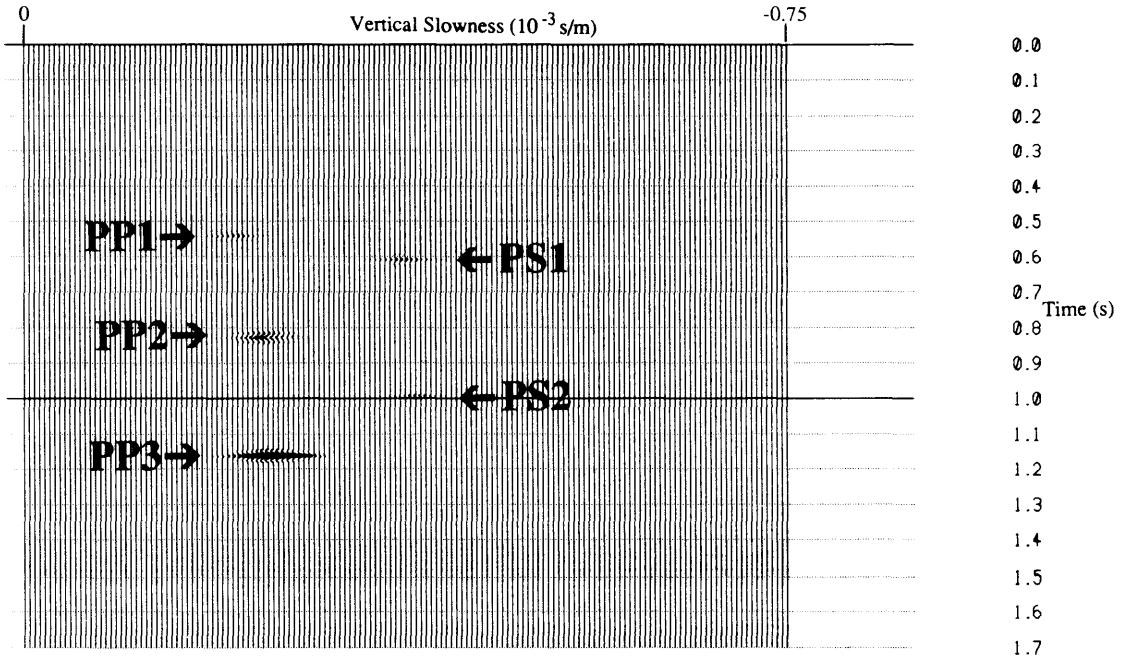


Figure 3.13 Semblance-weighted p-t decomposition of the 9-trace local window centered on the 980-meter trace of the vertical component of the upgoing wavefield for the synthetic data set shown in Figure 2.19.

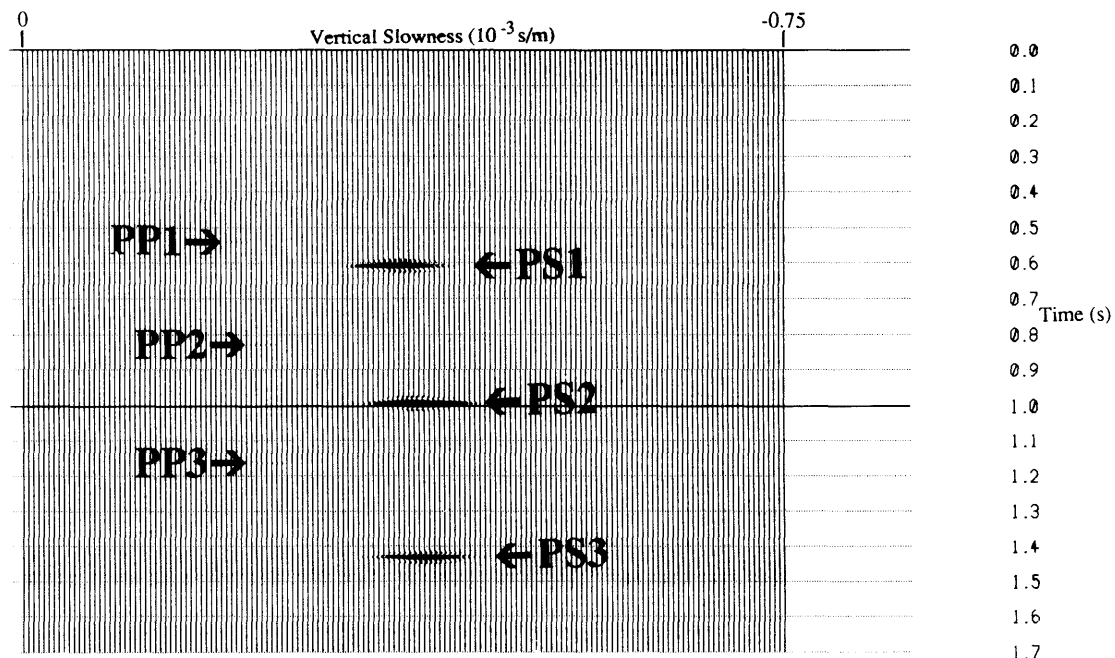


Figure 3.14 Semblance-weighted p-t decomposition of the 9-trace local window centered on the 980-meter trace of the radial component of the upgoing wavefield for the synthetic data set shown in Figure 2.20.

The semblance weighting has also sharpened the picture so that the slowness value for the maximum semblance for, say, the P-P reflections can be seen to increase with time. The maximum semblance for the third P-P reflector occurs at a slowness that is higher in absolute value than that of the first P-P reflector. A similar pattern can also be observed for the P-SV converted waves. This phenomenon is caused by the variation in apparent P and S velocities along the vertical borehole. The shallow reflectors produce reflected rays that have higher angles of incidence with the borehole than the deeper reflectors. Equation 3.3 can be used to verify that the higher the angle of incidence of a given wave on a vertical borehole, the higher the apparent velocity of that event will be, and, a higher apparent velocity means a lower vertical slowness. That is why the reflections coming from shallow interfaces with relatively high angles of incidence occur at a slightly lower vertical slowness in the p-t domain than the reflections from deeper interfaces.

The P-S separation was performed using the P and S velocities of the synthetic model and the results are shown in Figures 3.15 and 3.16 for the pass-P and pass-S VSP sections respectively. The full P and S wavefields have been recovered as expected from the algorithm.

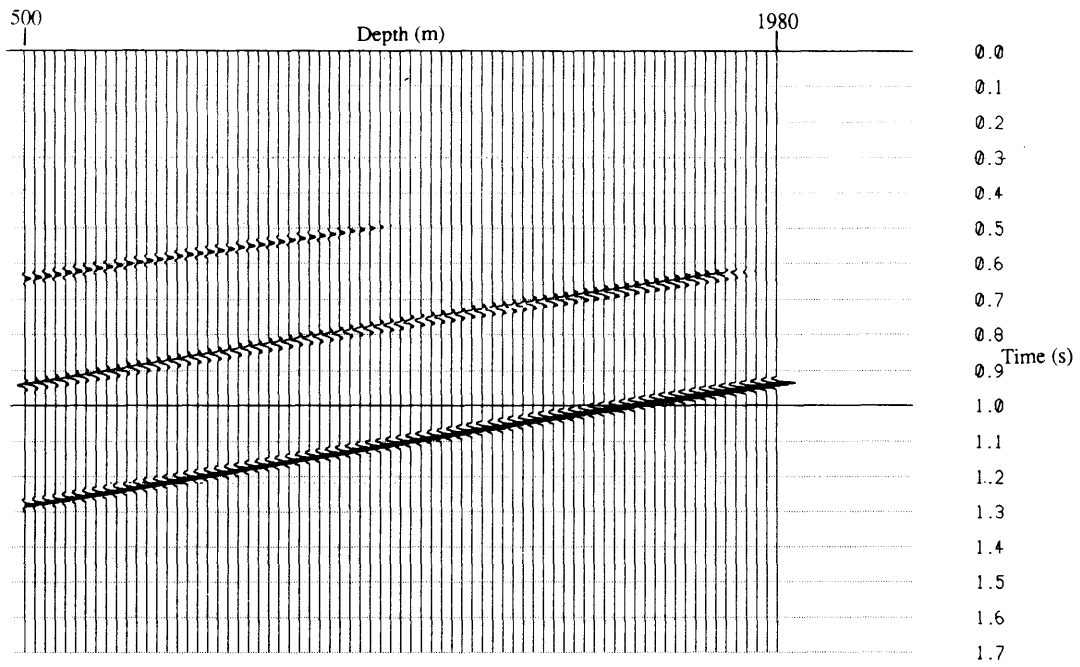


Figure 3.15 Pass-P wavefield for the synthetic data set.

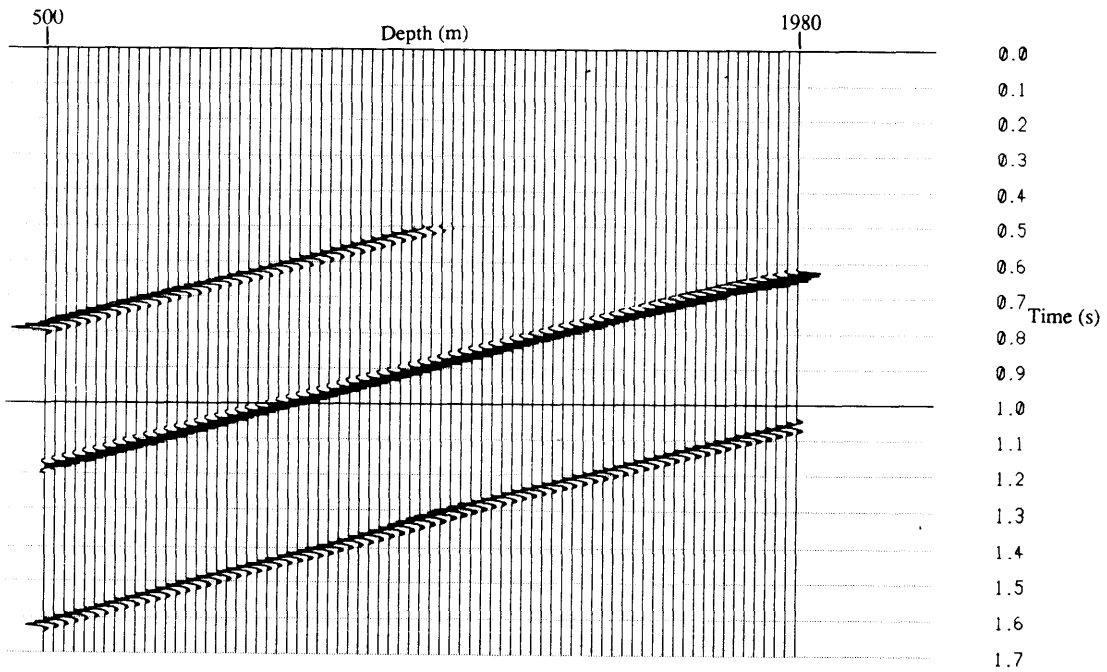


Figure 3.16 Pass-S wavefield for the synthetic data set.

3.6.2 Rolling Hills application

The vertical and radial components of the deconvolved and gained upgoing wavefields for the Rolling Hills data shown in Figures 2.32 and 2.33 were used in the P-S separation algorithm. A 9-trace local window was used for the p-t decompositions. The Rolling Hills VSP was recorded in an area where the P and S velocities vary considerably at the geophone locations along the borehole. As can be seen from Figure 2.29, the P and S velocities increase considerably at a depth of 935 meters. The two distinct velocity regions are also apparent on the vertical and radial components. The P and S events from the 540 m to the 920 m depth levels have a much greater slope than the events from the 940 m to 1840 m depth levels the larger slopes being associated with the lower velocity region. The velocities used in the filtering process (p-t method) were $V_P = 3000$ m/s and $V_S = 1500$ m/s for the 540 m to 920 m depth range, and $V_P = 5000$ m/s and $V_S = 2500$ m/s for the 940 m to 1840 m depth range. These approximated velocities (grossly averaged) were used to show that slight variations in velocities in the filtering process still produce acceptable results. The pass-P and pass-S sections are depicted in Figures 3.17 and 3.18 respectively.

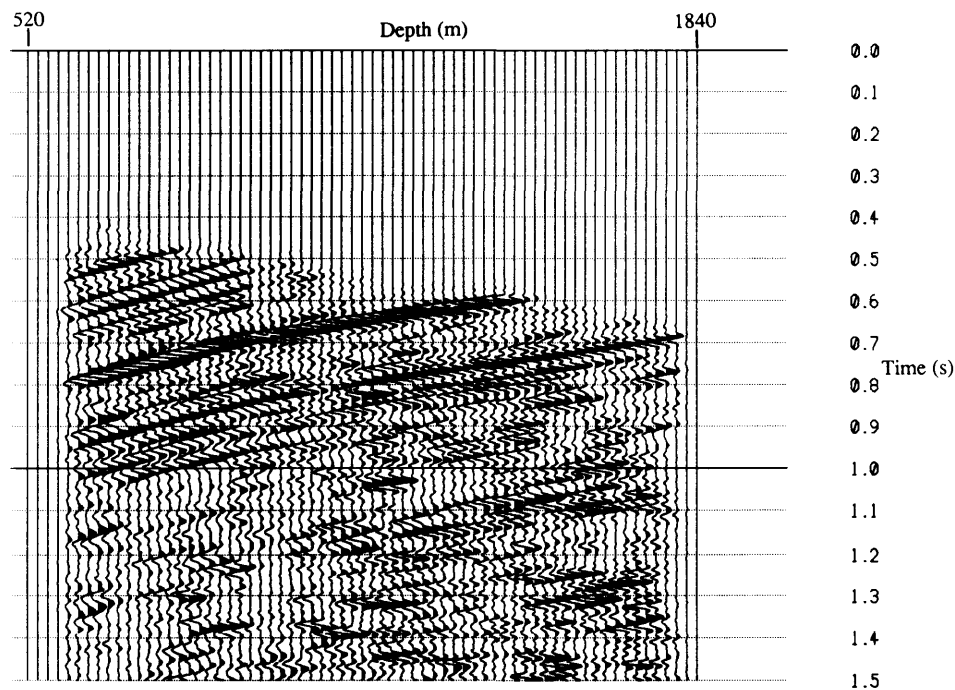


Figure 3.17 Pass-P wavefield for the Rolling Hills data set.

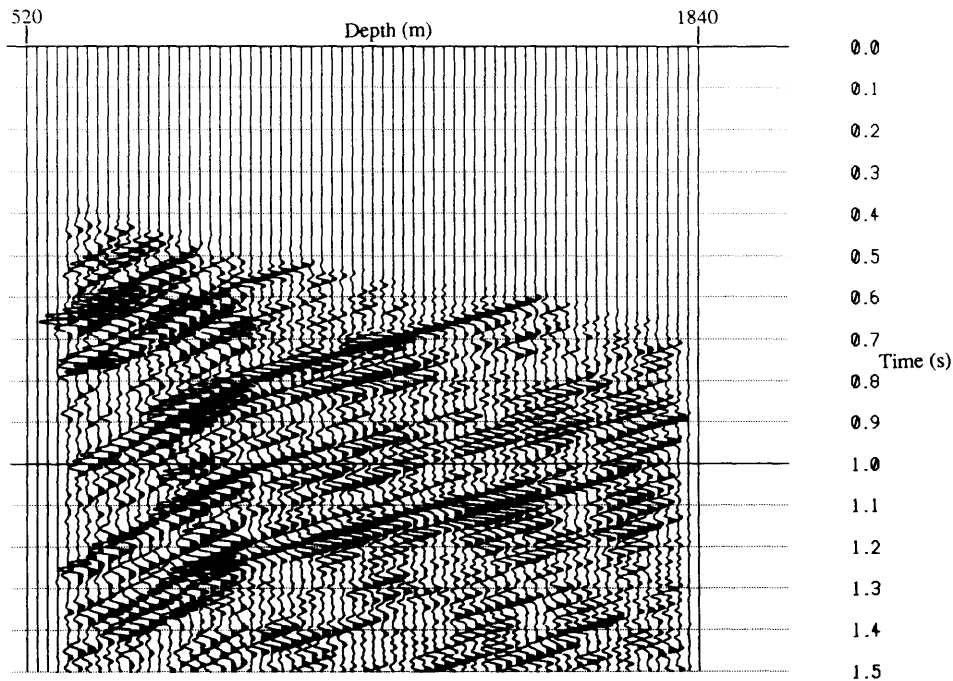


Figure 3.18 Pass-S wavefield for the Rolling Hills data set.

3.7 Application in the f-k domain

The same data sets were then filtered using the two-dimensional Fourier transform as a means of slowness decomposition (see Section 3.5.3). This was done in order to compare the p-t decomposition approach so that conclusions can be reached as to its effectiveness and performance. A cosine taper was applied to the edges of the data before the f-k filtering to minimize ringing effects inherent in the Fourier transform. The effect of the cosine function was removed after the data were inverse transformed back to the time domain by multiplying the same edges of the data by a secant function.

Spatial aliasing is a problem that needs to be considered when dealing with the Fourier transform. Spatial aliasing occurs when some event in a seismic section has an apparent velocity (V_{ap}) that is too low for the frequency content of the data. Mathematically, a data set is spatially aliased when the relation

$$V_{ap} k_N < f_{bp}$$

3.22

is satisfied, where k_N is the Nyquist wavenumber defined in equation 3.19 and f_{bp} is the bandpass frequency or the highest frequency content in the data (Yilmaz, 1987). To avoid the 'wrapping around' effect of spatially aliased data in the f - k domain, a bandpass filter must be applied to the data so that equation 3.22 is not satisfied.

3.7.1 Synthetic application

For the synthetic data used here, the lowest apparent velocity found in the data is 2500 m/s. With a spatial sampling interval of 20 m, the aliasing frequency, f_{bp} , is 62.5 Hz. A trapezoidal bandpass filter of 3/10 - 50/60 Hz was applied to both vertical and radial components to prevent spatial aliasing of the synthetic data. The filtering operation was performed on the vertical and radial components of the upgoing wavefield shown in Figures 2.19 and 2.20. The P-S separation was applied twice, once with $V_P = 4000$ m/s and $V_S = 2500$ m/s, and another time with $V_P = 4300$ m/s and $V_S = 2700$ m/s. The traces belonging to their corresponding velocity sets were then stacked together to produce the final pass-P and pass-S sections shown in Figures 3.19 and 3.20.

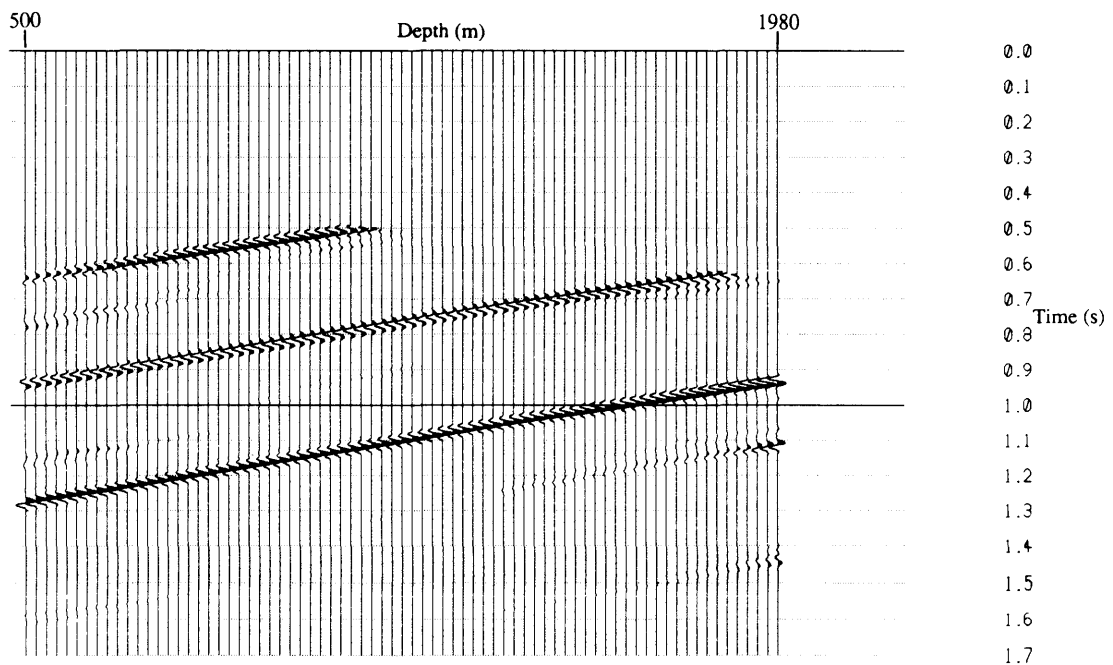


Figure 3.19 Pass-P wavefield for the synthetic data set obtained through the application of the P-S separation process in the f - k domain.

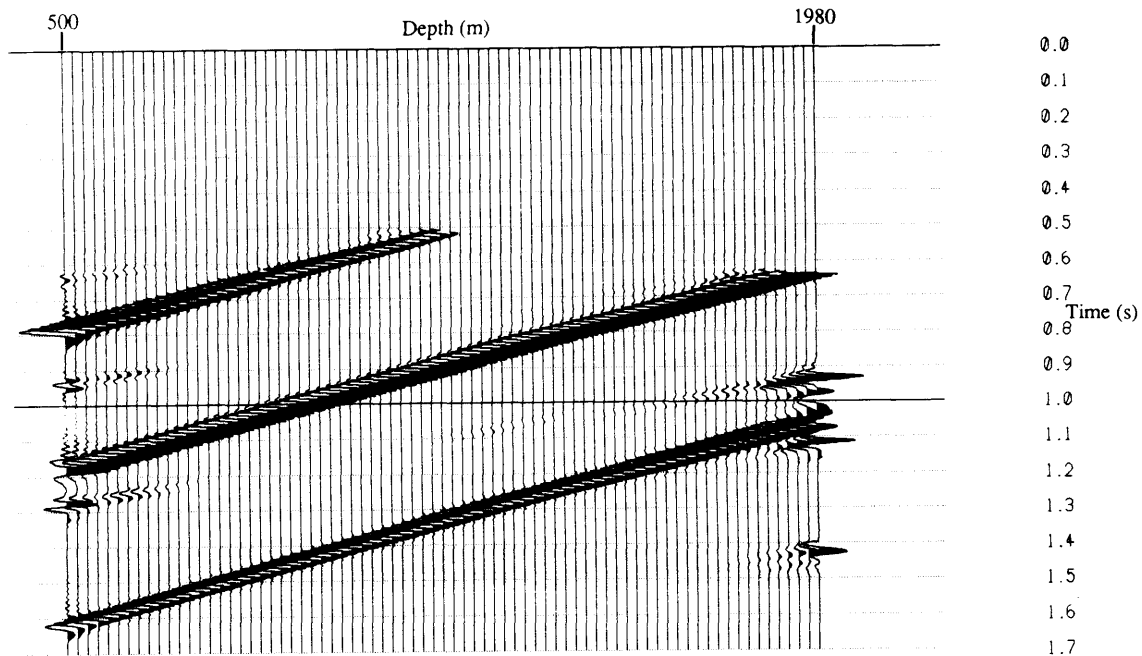


Figure 3.20 Pass-S wavefield for the synthetic data set obtained through the application of the P-S separation process in the f-k domain.

3.7.2 Rolling Hills application

Spatial aliasing is a problem in the Rolling Hills case. In the upper part of the VSP section, the S-wave apparent velocity reaches approximately 1500 m/s. Considering the 20 m sampling interval, this results in an aliasing frequency of 37.5 Hz. The lowest P-wave velocity, however, is 3000 m/s which results in a 75 Hz aliasing frequency. To account for this large discrepancy between the aliasing frequencies discussed above and the 100 Hz maximum frequency found in the Rolling Hills data as deduced from the input source frequency band (Section 1.4.2) or from spectral analysis (Geis et al., 1989), two different bandpasses were performed for each mode of the P-S separation. In the pass-P mode, a 3/10 - 60/75 Hz trapezoidal bandpass filter was applied, and in the pass-S mode, a 3/10 - 45/55 Hz trapezoidal bandpass filter was applied. The 55 Hz high cut frequency for the pass-S mode is still higher than the aliasing frequency, but, the author feels that too much signal would have been lost if the more drastic 37.5 Hz high cut had been applied. The filtering operation was performed on the vertical and radial components of the deconvolved, gained upgoing wavefield shown in Figures 2.32 and 2.33. The P-S

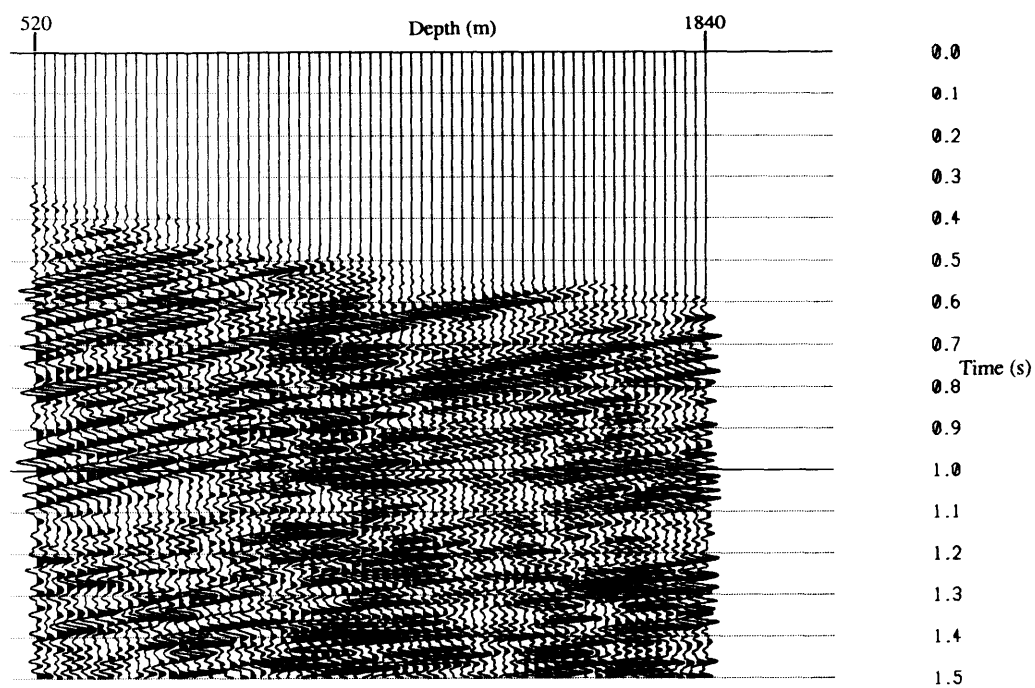


Figure 3.21 Pass-P wavefield for the Rolling Hills data set obtained through the application of the P-S separation process in the f-k domain.

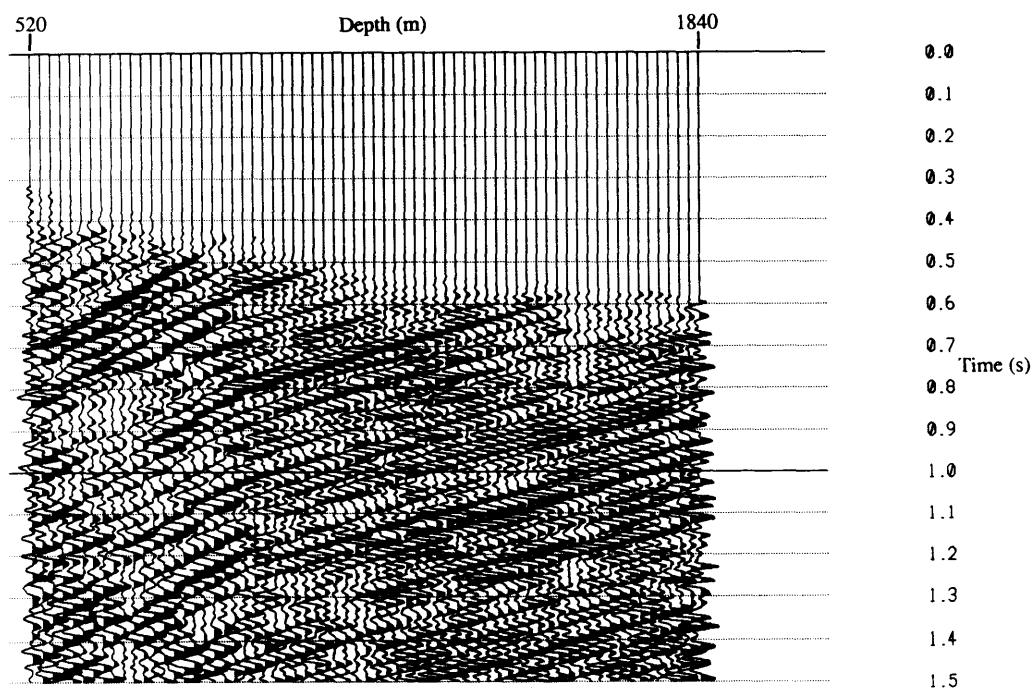


Figure 3.22 Pass-S wavefield for the Rolling Hills data set obtained through the application of the P-S separation process in the f-k domain.

separation was applied twice, once with $V_P = 5000$ m/s and $V_S = 2500$ m/s, and another time with $V_P = 3000$ m/s and $V_S = 1500$ m/s. The traces belonging to the corresponding velocity sets were then stacked together to produce the final pass-P and pass-S sections shown in Figures 3.21 and 3.22.

3.8 Discussion

The synthetic data are useful in evaluating new algorithms since they are free of noise. Any artifacts and by-products of the different processes can be readily identified. In the case of the P-S separation algorithm, many points are worth mentioning upon inspection of the pass-P and pass-S sections obtained through the p-t decomposition and f-k transform methods. The side effects of the Fourier transform are most noticeable in the results obtained through the f-k transform (Figures 3.19 and 3.20). The so called Gibb's phenomenon (Sheriff and Geldart, 1983), caused by the Fourier transformation of data with sharp discontinuities, is clearly identifiable at the edges of the data sets, more specifically for the 500 to 700 m and 1700 to 1980 m depth levels. This ringing effect seems to have been amplified by the fact that these sections were obtained by stacking the vertical and radial components in the f-k domain. If the two plots are mentally overlapped, one will notice that the side effects lie precisely on the regions where the opposite modes are present. On the pass-P section, the side effects lie where the S waves are present in the pass-S section; similarly, on the pass-S section, the side effects are present where the P waves reach the edges in the pass-P section. The events near the edges also seem to have been smeared in time. The pass-P and pass-S sections obtained through the p-t decomposition method (Figures 3.15 and 3.16) are better defined than their f-k equivalents: the events are well defined throughout the sections, even near the edges, and no smearing of energy in time or in space has been produced by the p-t decomposition method. The relative amplitudes of the P-P and P-SV reflections discussed in Section 2.5.1 have been preserved by both the f-k and the p-t decomposition methods as expected of the algorithms.

In the Rolling Hills case, the presence of noise inherent in real data makes it more difficult to identify the side effects of the Fourier transform. However, one can notice that the zero traces that were killed after deconvolution have been filled with data in the results obtained through the f-k transform (Figures 3.21 and 3.22). This again is an artifact of the Fourier transform which tends to smear energy across zero traces (Yilmaz, 1987). This smearing of energy over zero traces is still present when the p-t decomposition is used (Figures 3.17 and 3.18) but to a lesser degree. One can picture that a p-t decomposition for

a local window centered on a zero trace would still contain some energy belonging to the data traces present in the local window; the reconstructed trace obtained by stacking across the range of slownesses would create some data at the depth level of the trace that was previously filled with zeros. This smearing of energy, however, only occurs (or is only apparent) on the one trace closest to the non-zero filled data as compared to all the zero traces in the f-k case. Finally, comparing the pass-P and pass-S sections of the field data set obtained through both methods, one can see that a definite ringing in time is present in the results obtained through the f-k method, especially in the pass-P mode.

Chapter 4 - Subsurface mapping of VSP data

When the seismic source used in VSP is offset a certain distance from the borehole, the reflected waves received at the geophone originate from reflection points which are laterally offset from the borehole. In this chapter, a method of mapping the P-P and P-SV reflections is derived for a flat-layered medium with different source and receiver elevations. The method is applied to the P and SV wavefields of the synthetic and Rolling Hills data cases. The separated waves are used.

The concept used for mapping P-P reflected waves from an offset VSP was outlined by Dillon and Thompson (1984) and Wyatt and Wyatt (1984). A P-SV mapping technique for surface seismic data using the ray parameter was discussed by Chung and Corrigan (1985) and McCormack and Tatham (1988). Stewart (1988) extended the converted wave mapping idea using the ray parameter to VSP data. Stewart and Labonté (1989) go through the details of P-P and P-SV mapping of offset VSP data using the ray parameter approach.

4.1 P-P wave case

For a horizontally layered medium, the horizontal slowness p_x is defined as

$$p \equiv p_x = \frac{\sin \theta_i}{\alpha_i}, \quad 4.1$$

where θ_i is the angle of incidence of the P wave in layer i and α_i is the P-wave velocity in layer i (Figure 4.1).

From Figure 4.1, the distance covered by the reflected wave is given by

$$X_r = \sum_{i=N}^M Z_i \tan \theta_i, \quad 4.2$$

$$X_r = \sum_{i=N}^M \frac{Z_i p \alpha_i}{\sqrt{1 - p^2 \alpha_i^2}}. \quad 4.3$$

The total horizontal distance traversed can be written as

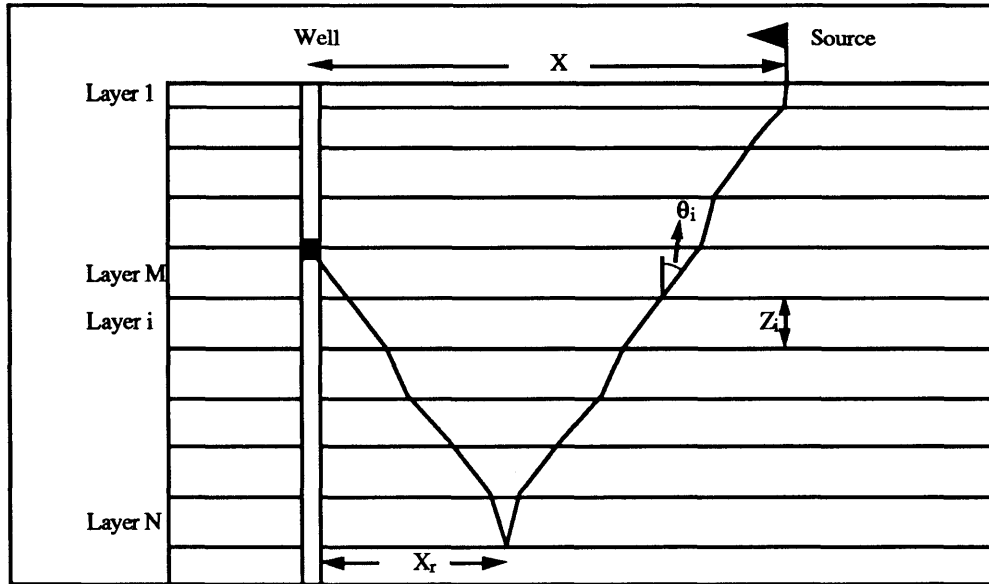


Figure 4.1 VSP ray geometry for a flat multilayered medium.

$$X = X_r + \sum_{i=1}^N Z_i \tan \theta_i, \quad 4.4$$

$$X = X_r + \sum_{i=1}^N \frac{Z_i p \alpha_i}{\sqrt{1 - p^2 \alpha_i^2}}. \quad 4.5$$

If $p\alpha_i (\sin \theta_i)$ is small, then X_r and X can be written as

$$X = X_r + \sum_{i=1}^N Z_i p \alpha_i \left[1 + \frac{p^2 \alpha_i^2}{2} \right], \quad 4.6$$

$$X_r = \sum_{i=N}^M Z_i p \alpha_i \left[1 + \frac{p^2 \alpha_i^2}{2} \right]. \quad 4.7$$

Still more approximately, to first order in p ,

$$X_r = p \sum_{i=N}^M Z_i \alpha_i, \quad 4.8$$

$$X = p \left[\sum_{i=N}^M Z_i \alpha_i + \sum_{i=1}^N Z_i \alpha_i \right], \quad 4.9$$

and eliminating p in equations 4.8 and 4.9

$$X_r = \frac{X \left[\sum_{i=N}^M Z_i \alpha_i \right]}{\left[\sum_{i=N}^M Z_i \alpha_i + \sum_{i=1}^N Z_i \alpha_i \right]}, \quad 4.10$$

or

$$X_r = \frac{X}{1 + \frac{\tilde{V}_N^2 T_N}{\tilde{V}_{NM}^2 T_{NM}}}, \quad 4.11$$

with the RMS velocities \tilde{V}_N and \tilde{V}_{NM} for the downgoing and upgoing raypaths given by

$$\tilde{V}_N^2 T_N = \sum_{i=1}^N Z_i \alpha_i, \quad 4.12$$

$$\tilde{V}_{NM}^2 T_{NM} = \sum_{i=N}^M Z_i \alpha_i, \quad 4.13$$

and the zero-offset traveltimes expressed as

$$T_N = \sum_{i=1}^N \frac{Z_i}{\alpha_i}, \quad 4.14$$

$$T_{NM} = \sum_{i=N}^M \frac{Z_i}{\alpha_i}. \quad 4.15$$

Equation 4.11 gives the offset of the reflection point at a given depth (layer N).

Now, the traveltime of that same raypath also needs to be calculated to find the time sample

on the VSP trace corresponding to the reflection event at layer N. The traveltime of the P-P reflected wave from the source to the receiver is written as

$$t = \sum_{i=1}^N \frac{Z_i}{\alpha_i} \sec \theta_i + \sum_{i=N}^M \frac{Z_i}{\alpha_i} \sec \theta_i, \quad 4.16$$

$$t = \sum_{i=1}^N \frac{Z_i}{\alpha_i \sqrt{1 - p^2 \alpha_i^2}} + \sum_{i=N}^M \frac{Z_i}{\alpha_i \sqrt{1 - p^2 \alpha_i^2}}, \quad 4.17$$

and for small $p\alpha_i$ ($\sin \theta_i$)

$$t = \sum_{i=1}^N \frac{Z_i}{\alpha_i} + \sum_{i=N}^M \frac{Z_i}{\alpha_i} + p^2 \left[\sum_{i=1}^N \frac{Z_i \alpha_i}{2} + \sum_{i=N}^M \frac{Z_i \alpha_i}{2} \right]. \quad 4.18$$

But from 4.9

$$X^2 = p^2 \left[\sum_{i=N}^M Z_i \alpha_i + \sum_{i=1}^N Z_i \alpha_i \right]^2, \quad 4.19$$

so 4.18 can be expressed as

$$t = \sum_{i=1}^N \frac{Z_i}{\alpha_i} + \sum_{i=N}^M \frac{Z_i}{\alpha_i} + \frac{X^2}{2 \left[\sum_{i=1}^N Z_i \alpha_i + \sum_{i=N}^M Z_i \alpha_i \right]}, \quad 4.20$$

or

$$t = T_N + T_{NM} + \frac{X^2}{2 \left[\tilde{V}_N^2 T_N + \tilde{V}_{NM}^2 T_{NM} \right]}, \quad 4.21$$

where \tilde{V}_N , \tilde{V}_{NM} , T_N and T_{NM} are defined as in equations 4.12 to 4.15.

Equations 4.11 and 4.21 provide the mapping between the P-P reflected wave data and an offset section mapped in two-way normal incidence P time ($2 T_N$). In practice, for a

given depth below the depth level of the trace being mapped, equation 4.21 is evaluated giving the raw time (t_i) on the VSP trace corresponding to the depth being mapped. The amplitude of the seismic wavefield at t_i is then mapped to a two-way normal incidence P time, $2 T_N$ for the depth being mapped, and an offset position X_r as evaluated by equation 4.11. An output common reflection point (CRP) bin width has to be specified so that each mapped point can be placed into its appropriate CRP bin.

This P-P mapping was performed on the synthetic data using the pass-P section shown in Figure 3.15, the original P-wave velocities and a bin width of 20 m. The output mapped section is shown on Figure 4.2. The three reflections have been mapped to their horizontal locations. The two shallow reflections show a dip going up toward the borehole; this is due to the small-angle approximations made in the derivation of equations 4.11 and 4.21. The angles of incidence of reflected waves recorded in the borehole at reflectors near the borehole are always larger than the ones further away from the borehole which is why the mapped events do not stay flat at short offset locations for shallow reflectors. The third reflector, however, is mapped horizontally as the angles of incidence of reflected waves from deep reflectors tend to be smaller than rays coming from shallow reflector.

This P-P mapping was also performed on the pass-P section of the Rolling Hills data (Figure 3.17) using the velocities obtained by Geis et al. (1989) shown in Figure 2.29. A bin width of 5 m was chosen in order to yield a reasonable amount of traces in the mapped VSP section. The results are shown in Figure 4.3 yielding a series of flat reflectors as expected from the Rolling Hills area (Geis et al., 1989).

4.2 P-SV wave case

The method used for mapping P-SV reflected waves from an offset VSP is similar to the one derived in the previous Section; the difference being that the upward path of the ray is treated as an S wave. For a horizontally layered medium, the horizontal slowness p_x is defined as

$$p \equiv p_x = \frac{\sin \theta_i}{\alpha_i} = \frac{\sin \phi_i}{\beta_i}, \quad 4.22$$

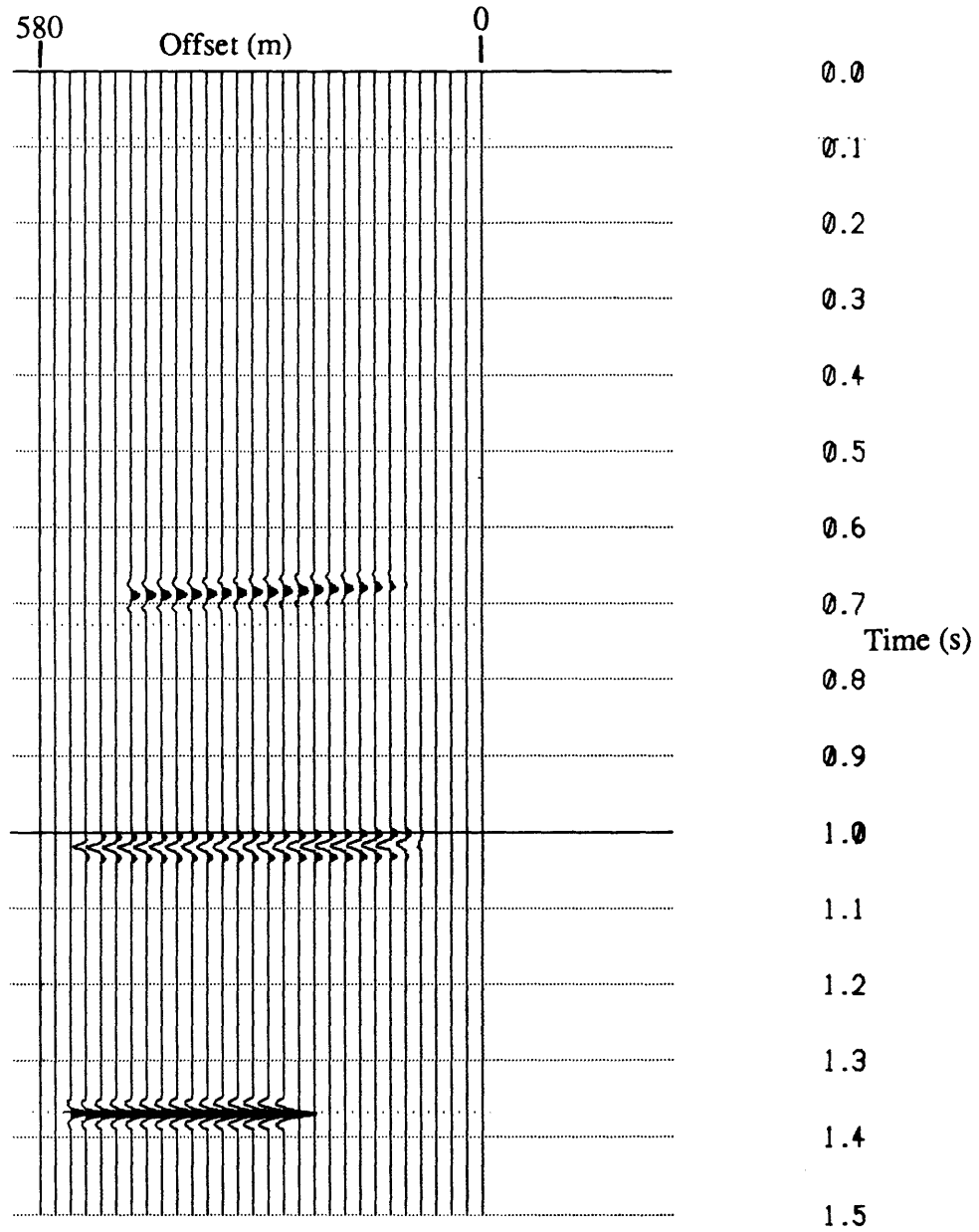


Figure 4.2 P-wave CRP map for the synthetic data.

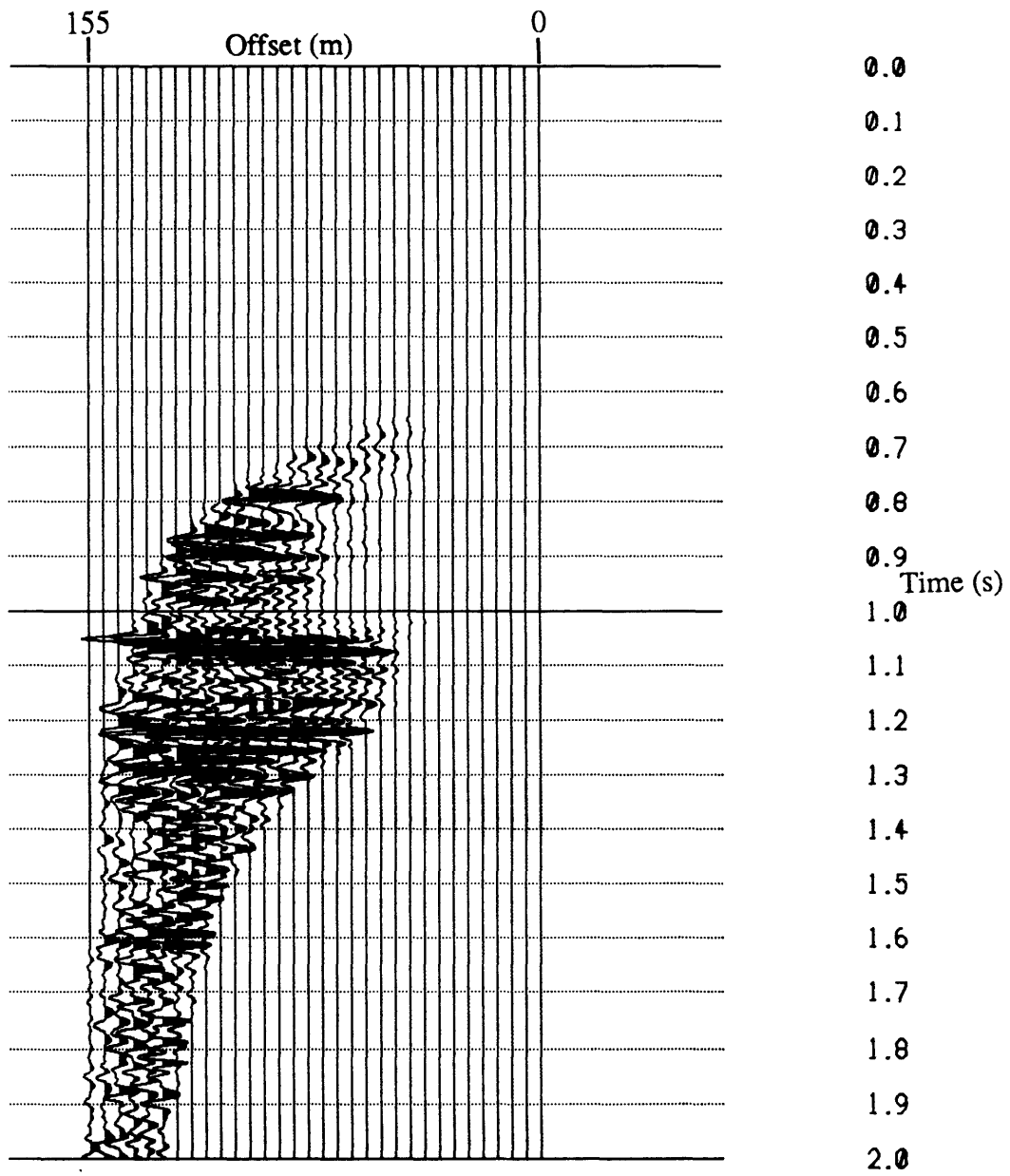


Figure 4.3 P-wave CRP map for the Rolling Hills data.

where θ_i is the angle of incidence of the P wave in layer i , ϕ_i is the angle of incidence of the S wave in layer i and α_i and β_i are the P and S-wave velocities respectively in layer i .

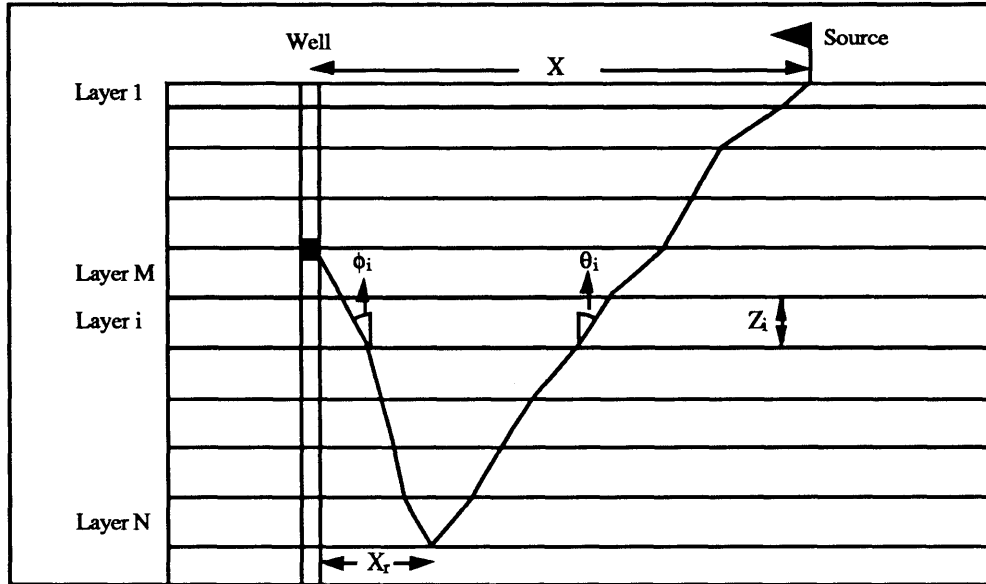


Figure 4.4 VSP ray geometry for P-SV reflections in a flat multilayered medium.

From Figure 4.4, the distance covered by the reflected wave is given by

$$X_r = \sum_{i=N}^M Z_i \tan \theta_i, \quad 4.23$$

$$X_r = \sum_{i=N}^M \frac{Z_i p \beta_i}{\sqrt{1 - p^2 \beta_i^2}}. \quad 4.24$$

The total horizontal distance traversed can be written as

$$X = X_r + \sum_{i=1}^N Z_i \tan \theta_i, \quad 4.25$$

$$X = X_r + \sum_{i=1}^N \frac{Z_i p \alpha_i}{\sqrt{1 - p^2 \alpha_i^2}}. \quad 4.26$$

If $p\alpha_i$ and $p\beta_i$ ($\sin \theta_i$ and $\sin \beta_i$) are small, then X_r and X can be written as

$$X = X_r + \sum_{i=1}^N Z_i p \alpha_i \left[1 + \frac{p^2 \alpha_i^2}{2} \right], \quad 4.27$$

$$X_r = \sum_{i=N}^M Z_i p \beta_i \left[1 + \frac{p^2 \beta_i^2}{2} \right]. \quad 4.28$$

Still more approximately, to first order in p ,

$$X_r = p \sum_{i=N}^M Z_i \beta_i, \quad 4.29$$

$$X = p \left[\sum_{i=N}^M Z_i \beta_i + \sum_{i=1}^N Z_i \alpha_i \right], \quad 4.30$$

and eliminating p in equations 4.8 and 4.9

$$X_r = \frac{X \left[\sum_{i=N}^M Z_i \beta_i \right]}{\left[\sum_{i=N}^M Z_i \beta_i + \sum_{i=1}^N Z_i \alpha_i \right]}, \quad 4.31$$

or

$$X_r = \frac{X}{1 + \frac{\tilde{V}_{PN}^2 T_{PN}}{\tilde{V}_{SNM}^2 T_{SNM}}}, \quad 4.32$$

with the RMS velocities \tilde{V}_{PN} and \tilde{V}_{SNM} for the downgoing and upgoing raypaths given by

$$\tilde{V}_{PN}^2 T_{PN} = \sum_{i=1}^N Z_i \alpha_i, \quad 4.33$$

$$\tilde{V}_{\text{SNM}}^2 T_{\text{SNM}} = \sum_{i=N}^M Z_i \beta_i, \quad 4.34$$

and the zero-offset traveltimes expressed as

$$T_{\text{PN}} = \sum_{i=1}^N \frac{Z_i}{\alpha_i}, \quad 4.35$$

$$T_{\text{SNM}} = \sum_{i=N}^M \frac{Z_i}{\beta_i}. \quad 4.36$$

Equation 4.32 gives the offset of the reflection point at a given depth (layer N). Now, the traveltime of that same raypath also needs to be calculated to find the time sample on the VSP trace corresponding to the reflection event at layer N. The traveltime of the P-P reflected wave from the source to the receiver is written as

$$t = \sum_{i=1}^N \frac{Z_i}{\alpha_i} \sec \theta_i + \sum_{i=N}^M \frac{Z_i}{\beta_i} \sec \theta_i, \quad 4.37$$

$$t = \sum_{i=1}^N \frac{Z_i}{\alpha_i \sqrt{1 - p^2 \alpha_i^2}} + \sum_{i=N}^M \frac{Z_i}{\beta_i \sqrt{1 - p^2 \beta_i^2}}, \quad 4.38$$

and for small $p\alpha_i$ and $p\beta_i$ ($\sin \theta_i$ and $\sin \phi_i$)

$$t = \sum_{i=1}^N \frac{Z_i}{\alpha_i} + \sum_{i=N}^M \frac{Z_i}{\beta_i} + p^2 \left[\sum_{i=1}^N \frac{Z_i \alpha_i}{2} + \sum_{i=N}^M \frac{Z_i \beta_i}{2} \right]. \quad 4.39$$

But from 4.30

$$X^2 = p^2 \left[\sum_{i=N}^M Z_i \beta_i + \sum_{i=1}^N Z_i \alpha_i \right]^2, \quad 4.40$$

so 4.39 can be expressed as

$$t = \sum_{i=1}^N \frac{Z_i}{\alpha_i} + \sum_{i=N}^M \frac{Z_i}{\beta_i} + \frac{X^2}{2 \left[\sum_{i=1}^N Z_i \alpha_i + \sum_{i=N}^M Z_i \beta_i \right]}, \quad 4.41$$

or

$$t = T_{PN} + T_{SNM} + \frac{X^2}{2 \left[\tilde{V}_{PN}^2 T_{PN} + \tilde{V}_{SNM}^2 T_{SNM} \right]}, \quad 4.42$$

where \tilde{V}_{PN} , \tilde{V}_{SNM} , T_{PN} and T_{SNM} are defined as in equations 4.33 to 4.36.

Equations 4.32 and 4.42 provide the mapping between the P-SV converted wave data and an offset section mapped in two-way normal incidence P time ($2 T_N$). In practice, for a given depth below the depth level of the trace being mapped, equation 4.42 is evaluated giving the raw time (t_i) on the VSP trace corresponding to the depth being mapped. The amplitude of the seismic wavefield at t_i is then mapped to a two-way normal incidence P time, $2 T_N$ for the depth being mapped, and an offset position X_r as evaluated by equation 4.32. An output common conversion point (CCP) bin width has to be specified so that each mapped point can be placed into its appropriate CCP bin.

This P-SV mapping was performed on the synthetic data using pass-S section (Figure 3.16), the original P- and S-wave velocities and a bin width of 20 m. The output mapped section is shown on Figure 4.5. The three reflections have been mapped to their horizontal locations. The two shallow reflections show a dip going up toward the borehole; this is due to the small angle approximations made in the derivation of equations 4.32 and 4.42. The incident and reflected angles of the rays near the borehole will always be larger than the ones further away from the borehole which is why the mapped event does not stay flat at short offset locations for shallow reflectors. The third reflector, however, is mapped horizontally as the incident and reflected angles for the rays coming from deep reflectors tend to be smaller than for rays coming from shallow reflector.

This P-SV mapping was also performed on the pass-P sections of the Rolling Hills data (Figure 3.18) using the velocities in Figure 2.29 and a bin width of 5 m. The results are shown in Figure 4.6 yielding a series of flat reflectors as expected from the Rolling Hills area (Geis et al., 1989).

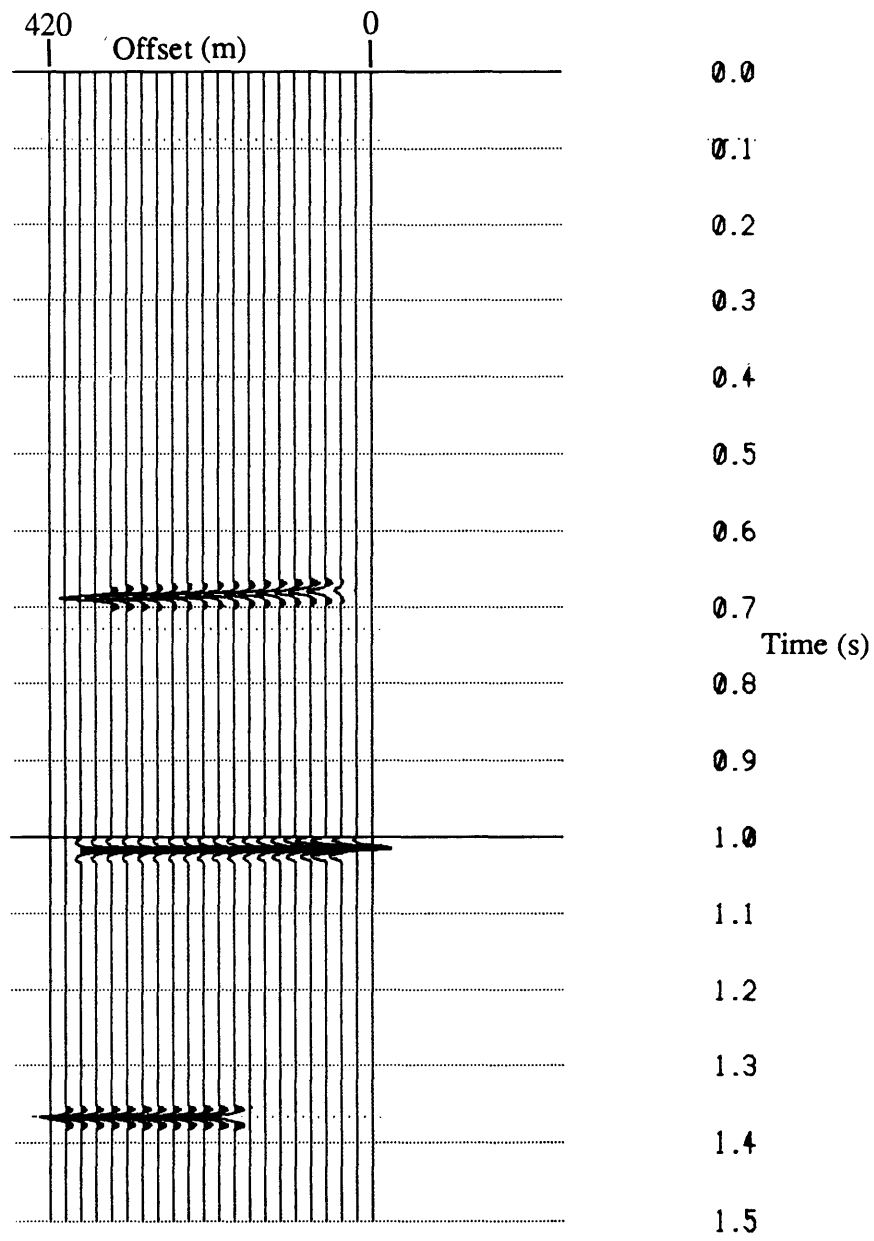


Figure 4.5 Converted SV-wave CCP map for the synthetic data.

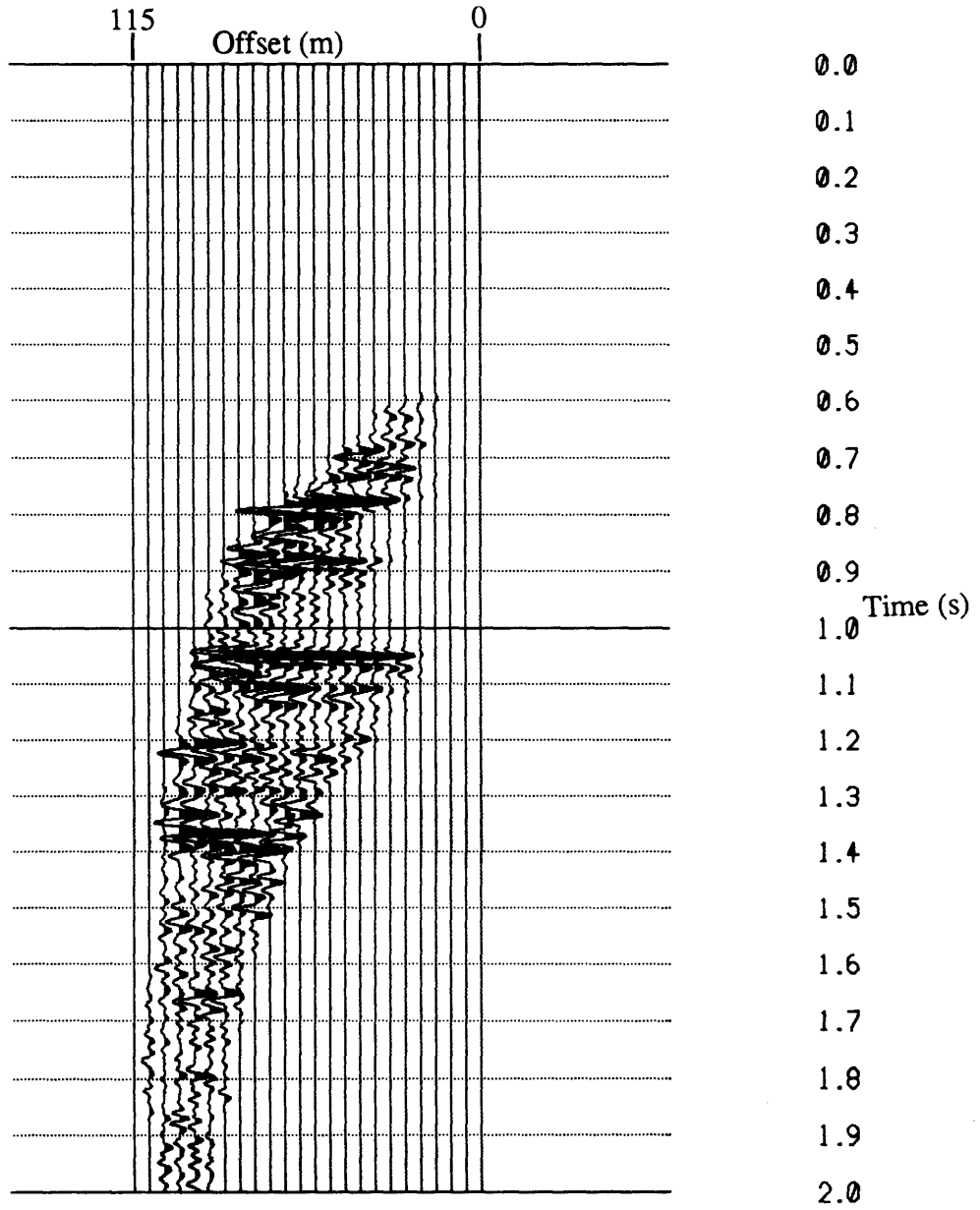


Figure 4.6 Converted SV-wave CCP map for the Rolling Hills data.

4.3 Discussion

The polarity convention used for the P-P and P-SV reflections is similar to the one used by Geis et al. (1989) as explained below. An increase in P-wave velocity across an interface represents a positive impedance contrast and results in a positive P-P reflection coefficient. However, an increase in P- and S-wave velocity across an interface also represents a positive impedance contrast, but, results in a negative P-SV reflection coefficient. These results are the ones obtained for P-P and P-SV reflection coefficients by Aki and Richards (1980) for pre-critical angles of incidence. A negative P- and S-wave impedance contrast across an interface results in a negative P-P and positive P-SV pre-critical reflection coefficient. This polarity convention can be observed on the synthetic maps. For the P-wave case, the first and third interfaces have positive P-wave impedance contrasts and, therefore, show up as peaks on Figure 4.2; the second interface, on the other hand, has a negative P-wave impedance contrast and is depicted as a trough in Figure 4.2. For the S-wave case, the first and third interfaces, having positive S-wave impedance contrasts, show as troughs on Figure 4.5 while the second interface, having a negative impedance contrast, shows up as a peak on Figure 4.5.

The accuracy of the mapping algorithms can be evaluated by comparing the mapped offsets and times of the three reflectors of the synthetic data obtained through the mapping process and their expected values as calculated by the ray-tracing program. Figure 4.7 depicts the mapped region (shaded area) for P-P reflections of the synthetic as calculated by the ray tracer. The points 1a, 1b, 2a, 2b, 3a and 3b point to the outer limits of the mapped area at the three reflectors' depths. Figure 4.8 depicts the same scenario but for the P-SV reflections of the synthetic data.

Table 4.1 shows the values of the outer limit points for the P-P and P-SV mapping case obtained through the ray tracer (true reflection points). These values are compared to the actual values obtained upon inspection of the P-P and P-SV maps of the synthetic data. In inspecting the synthetic maps, the outer limits of the mapped area are identified by looking for the first and last traces with seismic energy for a given reflector. For example, for the P-P case in Figure 4.2, the first trace with considerable seismic energy for the second reflector (point 2a) occurs at trace #5 which, with a bin width of 20 m, corresponds to an offset region of 80 to 100 m, the center of which is 90 m (center of mapped bin location). Similarly for the P-SV case in Figure 4.5, the outer limit of the mapped area for the third reflector (point 3b) occurs at the 21st trace which corresponds to an offset region

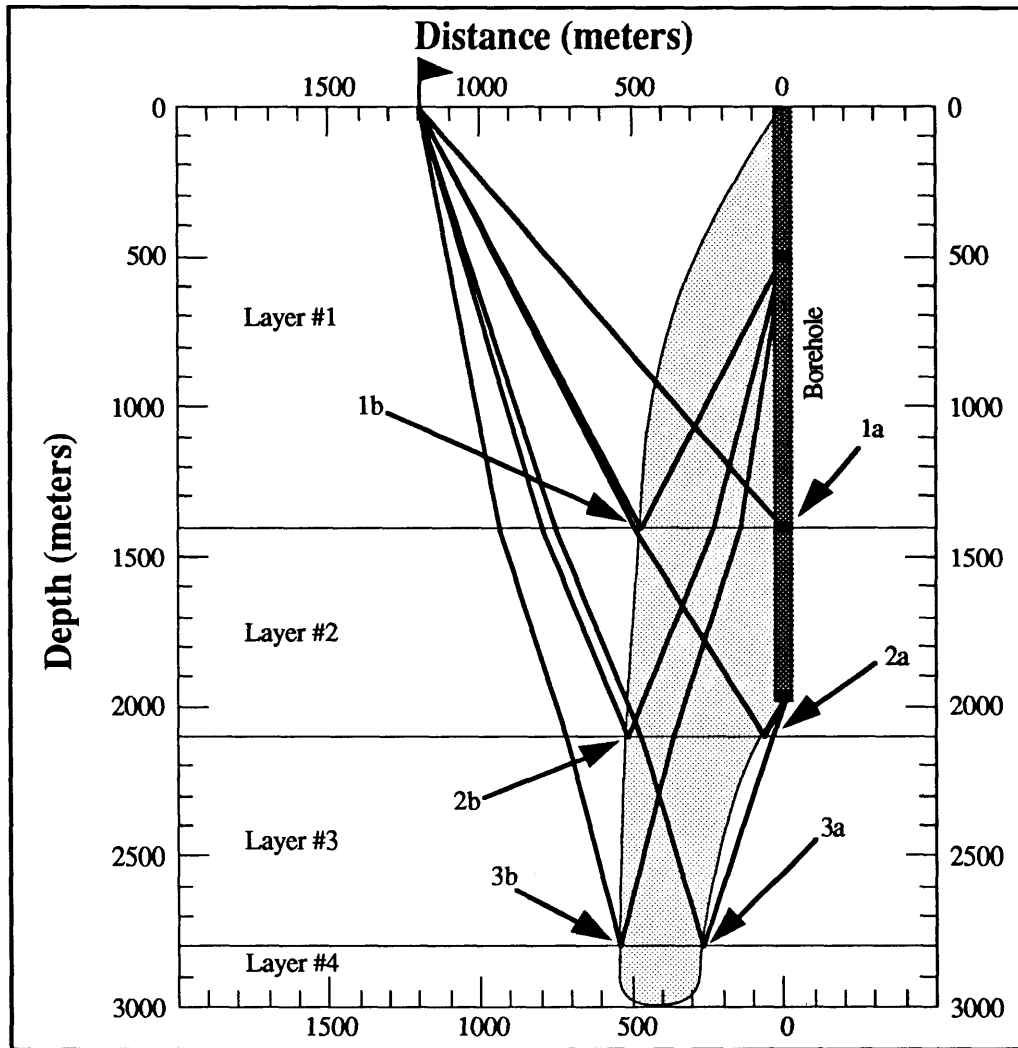


Figure 4.7 Mapped region (shaded area) for P-P reflections of the synthetic as calculated by the ray tracer. The points 1a, 1b, 2a, 2b, 3a and 3b point to the outer limits of the mapped area at the three reflectors' depths.

of 400 to 420 m giving a center of mapped bin location of 410 m.

The centers of mapped bin locations for points 1a for the P-P and P-SV reflectors do not apply in the comparison since the first reflector's inner mapped limits were truncated by the muting process applied to remove the downgoing wavefield in Section 2.5.1. This is because the reflections that occur at or near the first breaks happen to map at very short offset points from the borehole (Wyatt and Wyatt, 1984). The muting has also affected the second P-P reflection at point 2a. This event was truncated by the muting even though its P-SV equivalent was not affected by the muting. This is because the P-P reflection has an

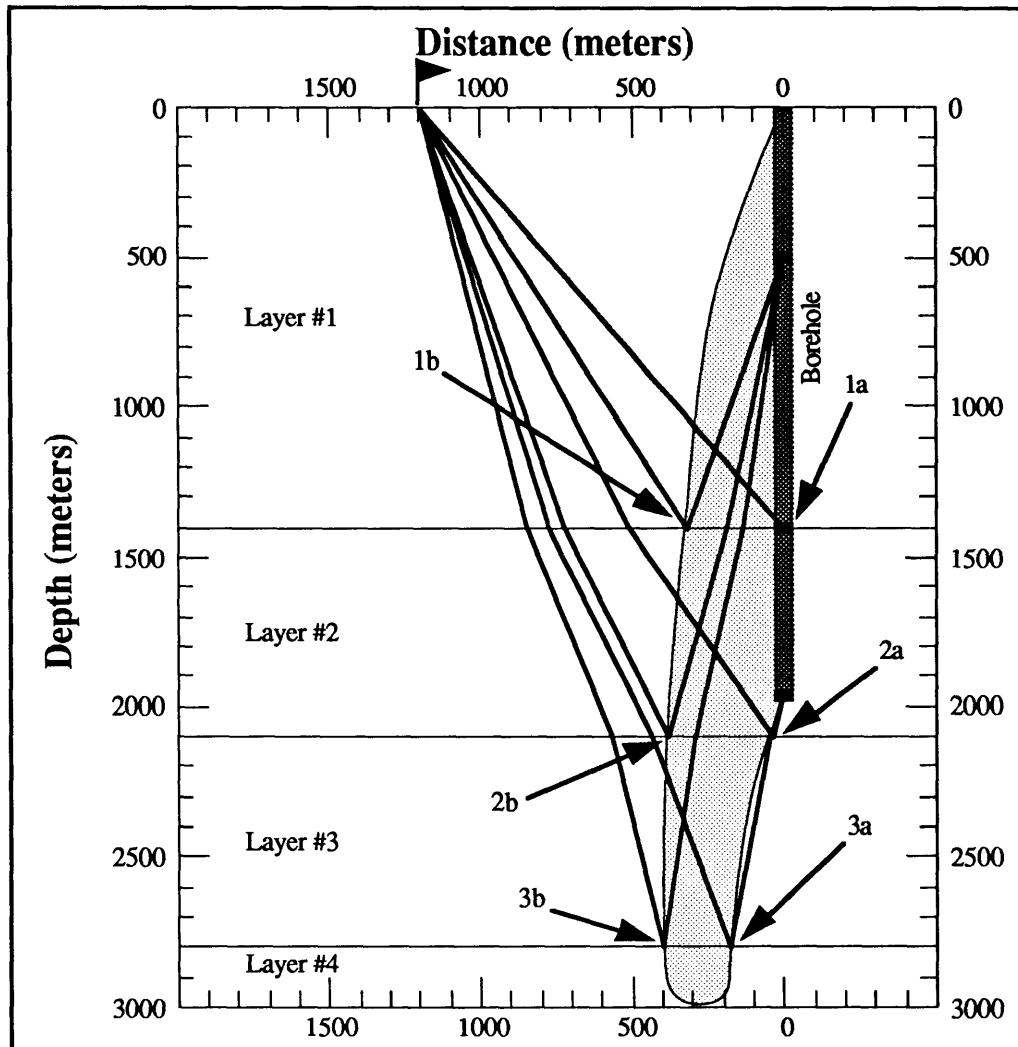


Figure 4.8 Mapped region (shaded area) for P-SV reflections of the synthetic as calculated by the ray tracer. The points 1a, 1b, 2a, 2b, 3a and 3b point to the outer limits of the mapped area at the three reflectors' depths.

apparent velocity that is higher than its P-SV counterpart on the original VSP section seen on Figures 2.19 and 2.20. One can actually see on those two figures that the P-P reflection from the second reflector (PP2) has been truncated more than its P-SV equivalent (PS2). This explains the large difference between the true reflection point at location 2a for the P-P case. Considering that the bin width is 20 m, variation of ± 10 m from the center of the mapped bin location are acceptable. Points 1b, 3a and 3b for the P-P case and points 2a and 3a for the P-SV case have true reflection points that fall within the right bin width. All the other points, namely point 2b for the P-P case and points 1b, 2b and 3b for the P-SV case do not fall within their right bin location. This difference is due to the approximations

Reflector	P - P reflections		P - SV reflections	
	True reflection point (m)	Center of mapped bin location (m)	True reflection point (m)	Center of mapped bin location (m)
1a	0	n/a	0	n/a
1b	469	470	318	350
2a	64	90	38	30
2b	516	530	378	390
3a	265	270	174	170
3b	543	550	397	410

Table 4.1 Values of the true reflection point offsets as calculated by the ray-tracing program and the center of mapped bin location obtained by inspection of the synthetic maps for each of the P-P and P-SV reflections. The reflector identifiers are as in Figures 4.7 and 4.8.

Reflector	P - P time (10^{-3} s)	P - SV time (10^{-3} s)	Actual time (10^{-3} s)
1a	690	680	700
1b	675	690	700
2a	1020	1020	1026
2b	1020	1020	1026
3a	1370	1370	1376
3b	1370	1370	1376

Table 4.2 Values of the arrival times for the three reflectors of the synthetic data as observed on the P-P and P-SV maps of the synthetic data. The reflector identifiers are as in Figures 4.7 and 4.8. Note that the P-SV reflections were mapped to two-way normal incidence P-wave times.

made in equations 4.6 - 4.9 and 4.18 for the P-P wave case and equations 4.27 - 4.30 and 4.39 in the P-SV wave case. The maximum discrepancy occurs for the P-SV reflection at point 1b where it reaches 6.9% of the true reflection point value. At that point, the angle of incidence of the compressional wave reaches 60° . The mapped location used in the percentage difference calculation is the mapped location that is closest to the true reflection point within the bin width, 340 m in the case of the P-SV reflection at point 1b. All the other true reflection point values fall within 0.8% of their closest mapped values.

The arrival times of the outer edge limits of the reflection points for both the P-P and P-SV reflections of the synthetic data are shown in Table 4.2. The discrepancies between the observed times and the expected actual times is due to the approximations made in equations 4.6 - 4.9 and 4.18 in the P-P wave case and equations 4.27 - 4.30 and 4.39 in the P-SV wave case. The largest differences between the observed times and the expected time are for the P-P case at 1b where the measured time is 3.6% off the actual time and for the P-SV case at 1a where the measured time is 2.9% off the actual time. All the other values fall within 1.4% of their respective expected values.

Chapter 5 - Reflectivity inversion of P-SV converted waves

Mapping the converted wave data as in Section 4.2 provides a section which can be interpreted in structural and perhaps in stratigraphic terms. However, if the actual rock properties are to be analyzed, such as density and velocity, then the inverse problem must be considered. The inverse problem for this case may be stated as: given the converted-wave reflectivity, find the shear-wave velocity.

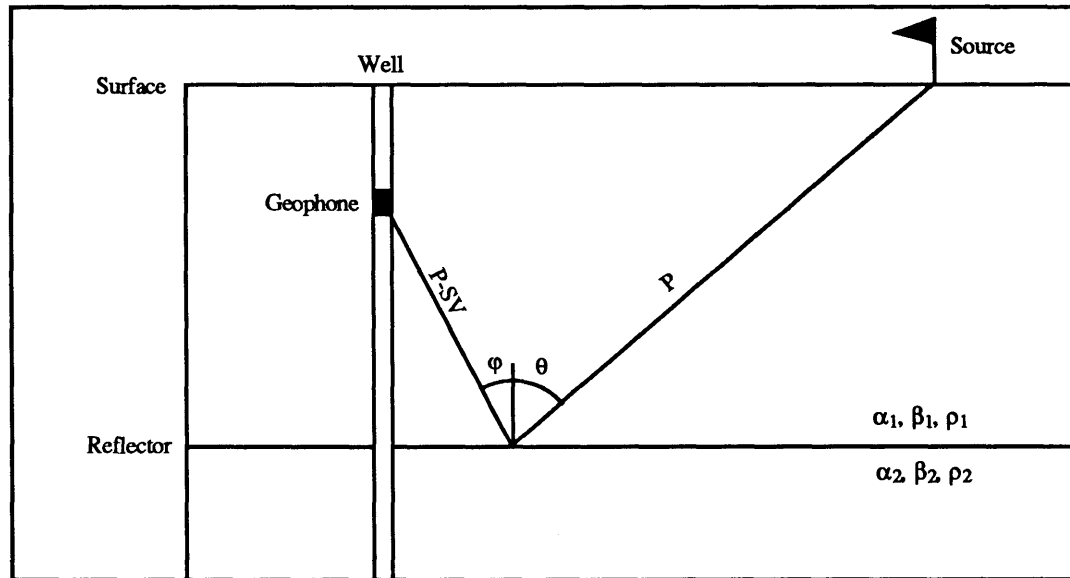


Figure 5.1 Converted wave reflectivity geometry.

This problem was first approached by Stewart (1989b) by starting with the expression defining the converted wave (P-SV) reflection coefficient for two half-spaces with only small differences in rock properties. The mathematical details of the derivation can be found in Stewart and Labonté (1989) and are followed here. With geometry as shown in Figure 5.1, Aki and Richards (1980) write the displacement reflection coefficient R as

$$R \equiv R_{PS} = \frac{-p\alpha}{2 \cos \varphi} \left[\left(1 - 2\beta^2 p^2 + 2\beta^2 \frac{\cos \theta}{\alpha} \frac{\cos \varphi}{\beta} \right) \frac{\Delta\rho}{\rho} - \left(4\beta^2 p^2 - 4\beta^2 \frac{\cos \theta}{\alpha} \frac{\cos \varphi}{\beta} \right) \frac{\Delta\beta}{\beta} \right], \quad 5.1$$

where $p = \frac{\sin \theta_1}{\alpha_1}$,

$$\alpha = \frac{\alpha_1 + \alpha_2}{2}, \Delta\alpha = \alpha_2 - \alpha_1,$$

$$\beta = \frac{\beta_1 + \beta_2}{2}, \Delta\beta = \beta_2 - \beta_1,$$

$$\rho = \frac{\rho_1 + \rho_2}{2}, \Delta\rho = \rho_2 - \rho_1.$$

Also, to first order $\frac{\sin \theta_1}{\alpha_1} = \frac{\sin \theta}{\alpha} = \frac{\sin \varphi}{\beta}$, and letting $\gamma = \beta/\alpha$ then

$$R = -\frac{\tan \varphi}{2\gamma} \left[\left(1 - 2\gamma^2 \sin^2 \theta + 2\gamma \cos \theta \cos \varphi \right) \frac{\Delta\rho}{\rho} - \left(4\gamma^2 \sin^2 \theta - 4\gamma \cos \theta \cos \varphi \right) \frac{\Delta\beta}{\beta} \right], \quad 5.2$$

or more simply

$$R = -k \left[\left(1 + \delta \right) \frac{\Delta\rho}{\rho} + 2\delta \frac{\Delta\beta}{\beta} \right], \quad 5.3$$

with $k = \frac{\tan \varphi}{2\gamma}$ and $\delta = -2\gamma^2 \sin^2 \theta + 2\gamma \cos \theta \cos \varphi$.

The problem is to find β or ρ from the reflectivity R . Some direction can be found from the conventional P-wave reflectivity inversion. The normal incidence P-wave reflection coefficient R_P , for small parameter changes, can be written as

$$R_P = \frac{1}{2} \left(\frac{\Delta\rho}{\rho} + \frac{\Delta\alpha}{\alpha} \right), \quad 5.4$$

and for the i^{th} interface, using the logarithmic derivative (after Sheriff and Geldart, 1983)

$$R_P = \frac{1}{2} \Delta \ln \rho \alpha, \quad 5.5$$

$$R_P^i = \frac{1}{2} \ln \frac{\rho_{i+1} \alpha_{i+1}}{\rho_i \alpha_i}. \quad 5.6$$

So, 5.6 can be written as

$$\rho_{i+1} \alpha_{i+1} = \rho_i \alpha_i \exp\left(2 R_P^i\right), \quad 5.7$$

and rearranging we get

$$\alpha_{i+1} = \frac{\rho_i}{\rho_{i+1}} \alpha_i \exp\left(2 R_P^i\right). \quad 5.8$$

A similar operation can be performed on the converted wave reflectivity

$$R^i = -k \ln \left[\left(\frac{\rho_{i+1}}{\rho_i} \right)^{1+\delta} \left(\frac{\beta_{i+1}}{\beta_i} \right)^{2\delta} \right], \quad 5.9$$

and for the i^{th} interface

$$\beta_{i+1} = \beta_i \left(\frac{\rho_i}{\rho_{i+1}} \right)^{\frac{1+\delta}{2\delta}} \exp\left(-\frac{R^i}{2\delta k}\right). \quad 5.10$$

Assuming that the density is constant

$$\beta_{i+1} = \beta_i \exp\left(-\frac{R^i}{2\delta k}\right). \quad 5.11$$

Simplifying the denominator of the exponential term

$$\beta_{i+1} = \beta_i \exp\left(-\frac{R^i}{2 \sin \varphi_i (\cos \theta_i - \sin \theta_i \tan \varphi_i)}\right). \quad 5.12$$

With N interfaces, equation 5.12 can be written as

$$\beta_{N+1} = \beta_1 \exp\left(-\sum_{i=1}^N \frac{R^i}{2 \sin \varphi_i (\cos \theta_i - \sin \theta_i \tan \varphi_i)}\right). \quad 5.13$$

In practice, an average of the reflection and incidence angles must be obtained in order to carry out equation 5.13. This is done by evaluating equation 4.32 for each time point at every depth level in the pass-S VSP section and using X_r and the depth of the reflector being mapped to come up with θ_i and φ_i . These angles are averaged at each time point within every bin location.

This inversion was performed on the P-SV map of the synthetic data for the seven traces belonging to the 240 to 360 m offset range. A value of $\beta_1 = 2500$ m/s was used, and the results are shown in figure 5.2. The actual values of the S-wave velocities obtained through the inversion are within 1% of the true S-wave velocities used in the model; at least this is true in the regions away from the interfaces where the seismic wavelet introduces artefacts. These will be discussed shortly.

The inversion was also performed on the Rolling Hills P-SV map. However, as with most recursive inversion schemes that operate on real data, a low-frequency velocity constraint is needed to provide realistic velocity values (Lindseth, 1979). This constraint is found from first break traveltimes inversion (from Geis et al., 1989). The integrated S-wave velocities shown in Figure 5.3(a) were bandpass filtered using a 0/0 - 10/15 Hz trapezoidal filter to give the low-frequency background velocity needed in the inversion (Figure 5.3(b)). Nine traces, belonging to the 45 to 90 m offset range of the P-SV map of the Rolling Hills data, were inverted as in equation 5.13 with $\beta = 0$ m/s. These results are shown in Figure 5.3(c). These inverted traces were then bandpass filtered with a 10/15 - 60/75 Hz trapezoidal filter, then added to the low-frequency background velocity in Figure 5.3(b) to yield the final inverted traces shown in Figure 5.3(d).

The top of the Wabamun (an increase in S velocity) and the top of the Beaverhill Lake salt (a decrease in S velocity) are used to analyze the inversion results. The top of the Wabamun is seen on Figure 5.3(a) as the large velocity increase at approximately 0.77 s and on Figure 5.3(c)-(d) as a peak shifted to about 0.8 s. The time shift in the data may be

caused by different datum points, replacement velocities or residual wavelet effects. This wavelet effect is the reason for the oscillatory signature of the top of the Wabamun. This is observed to occur over a time range equal to the period T of the wavelet, namely $T = 0.03$ s for this case. The same phenomenon can be observed for the top of the Beaverhill Lake salt which is seen at approximately 1.025 s in Figure 5.3(a). This same event is again shifted in time on Figures 5.3(c) and (d) to 1.055 s. The wavelength of the wavelet in this case is about the same as the Wabamun case, namely $T = 0.03$ s. The wavelet effect is also present in the synthetic data as no deconvolution was performed on the synthetic data set. The wavelength of the wavelet in the synthetic data case is of the order of $T = 0.02$ s.

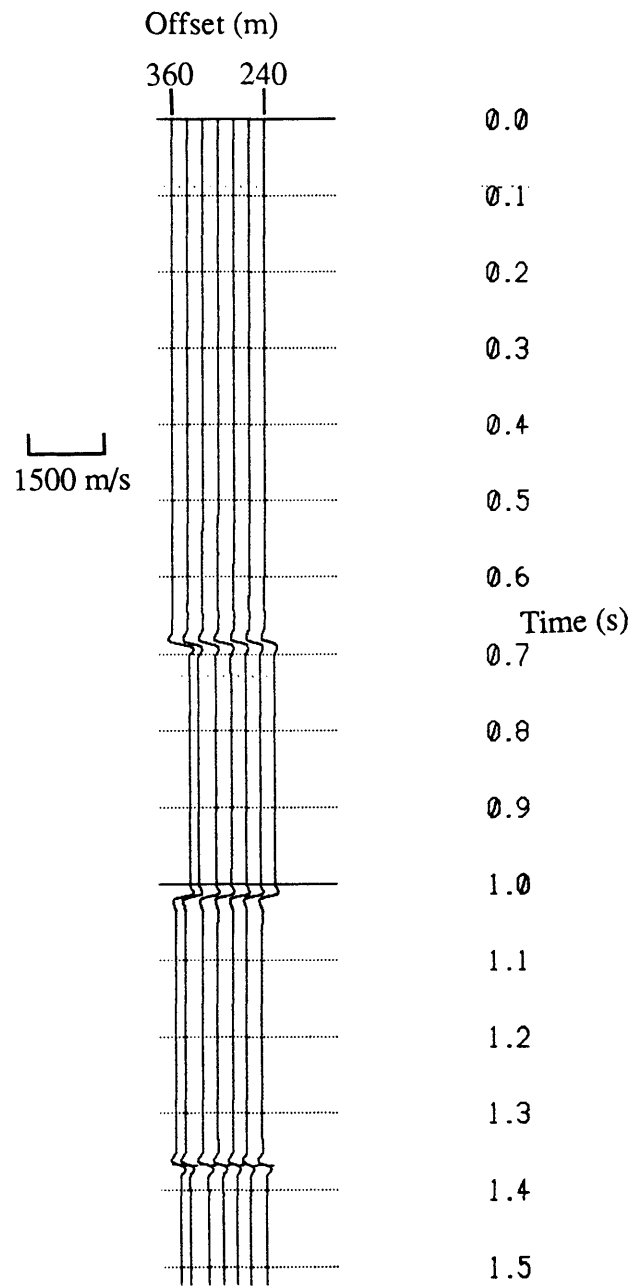


Figure 5.2 Traces belonging to the 240 to 360 m range of the P-SV map of the synthetic data of Figure 4.5 inverted using equation 5.13.

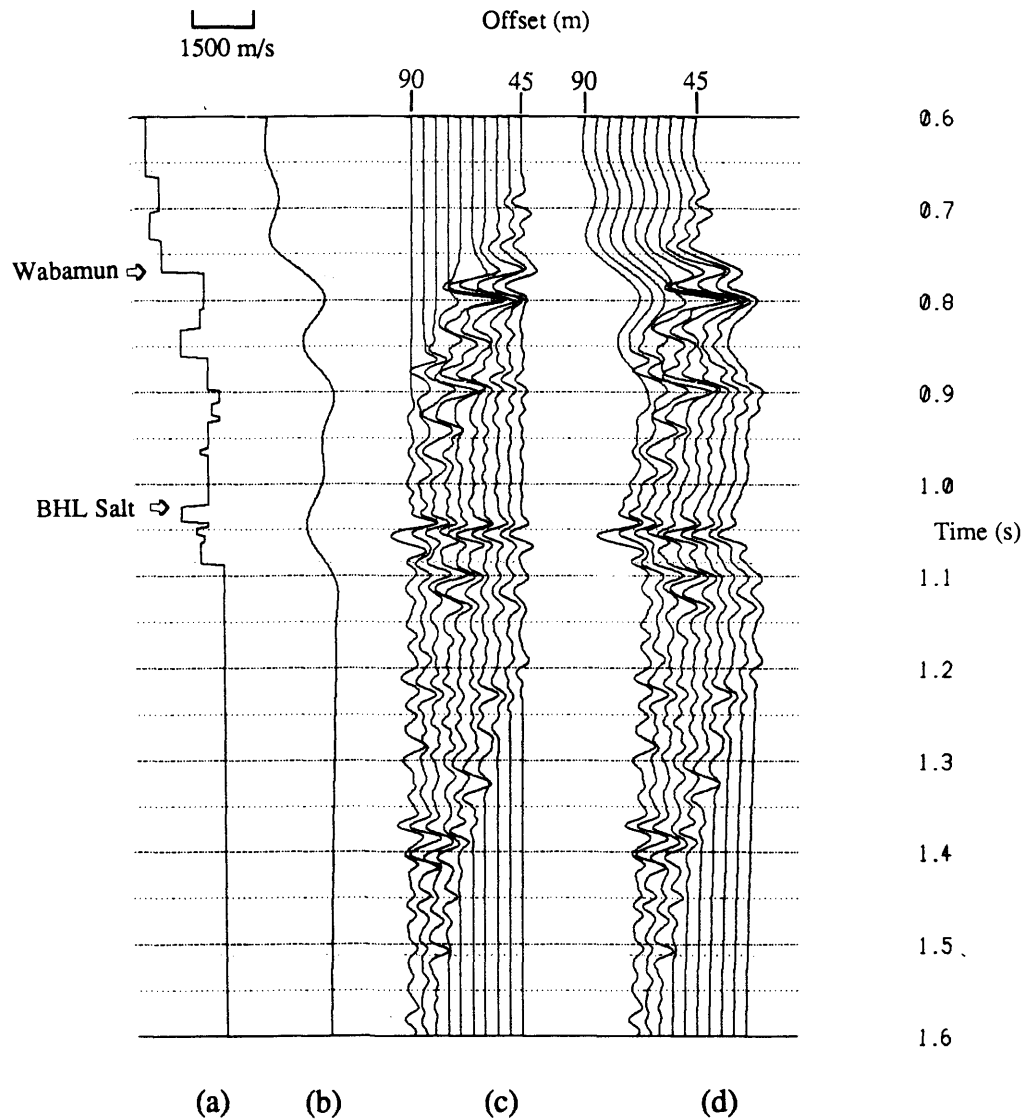


Figure 5.3 (a) Integrated S-wave velocity from Geis et al. (1989). (b) 0/0 - 10/15 Hz trapezoidal bandpass filtered version of (a). (c) 45 to 90 m offset traces from the P-SV map of Figure 4.6 inverted using equation 5.13. (d) Final inverted traces obtained by adding (b) with a 10/15 - 60/75 Hz trapezoidal bandpass filtered version of (c).

Chapter 6 - Conclusions

The thesis has discussed the processing of synthetic and field multi-component vertical seismic profiles (VSP). The randomly oriented horizontal components of the field VSP are rotated so that one of the two is always oriented in the sagittal plane (radial component) and the other is always oriented perpendicular to the sagittal plane (transverse component). The radial and vertical components are then used to equalize the energy present on both components in a time window centered on the first breaks. This is done as a first step in amplitude recovery and also to assure that there will not be any strong amplitude variations between adjacent traces in the VSP sections caused by coupling variations of the geophone between depth levels or by source amplitude variations between shots. The downgoing wavefield is then removed to yield to the more important upgoing wavefield. This is done by enhancing the downgoing wavefield using the p-t decomposition, in which the whole wavefield is transformed into the slowness domain and only the positive slownesses are used in the reconstruction. The enhanced wavefield is then subtracted from the total wavefield to yield the upgoing wavefield. This is done on both the radial and vertical components. For the synthetic case, the downgoing wavefield is removed by muting the first breaks. A velocity inversion is then performed on the data using the first downgoing P and S arrivals to give a P- and S-wave interval velocity function that will later be used for separating and mapping the P and S waves and inverting the S-wave map. A spiking deconvolution is performed on the field VSP. The filters are designed on a time series obtained by the vector addition of the first P breaks on the vertical and radial components of the enhanced downgoing wavefield for each trace. These filters are then applied to the vertical and radial components of the upgoing wavefield. The second step in amplitude recovery is then taken by applying a time-variant exponential gain to the data. The same gain is applied to the vertical and radial components so that polarization angle information is not lost.

The P-S wave mode separation is performed on the vertical and radial components of the deconvolved, gained, upgoing wavefield. The filter coefficients are derived by considering the displacement of incident P and S waves at the geophone location. Instabilities at slownesses $|p| > 1/V_P$ and $|p| > 1/V_S$ are eliminated by tapering the coefficients to zero at these slownesses. The separation is performed on the synthetic and field data in the p-t and f-k domains. The ringing and smearing of energy is noticeable on the results obtained through the f-k domain for both the synthetic and real data cases. The

results obtained through the p-t decomposition method do not show any smearing or ringing.

The mapping of the P-P and P-SV reflections is performed on the pass-P and pass-S sections for the synthetic and field cases from the P-S wave mode separation results obtained through the p-t decomposition method. Both the P-P and P-SV reflections are mapped to a two-way normal-incidence P-wave time. The errors in the mapping, caused amongst other things by small angle approximations in the derivation of the mapping algorithm, are assessed by inspection of the synthetic maps. The maximum error in offset mapping reaches 7% of the true offset location when the angle of incidence is 60° and the maximum error in time mapping is 4% of the true time location of the event.

The S-wave velocity inversion gives results that are within 1% of the true S-wave velocity for the synthetic case. However, in the field case, the inversion is strongly affected by the deconvolution used on the data. If the deconvolution performed perfectly so that the events are spiked, the inversion would perform much better. The wave character of the input data leaves an undesirable artefact in the resulting velocity. This so called wavelet effect is observed on both the synthetic and real data cases. The exponential gain applied to the field VSP traces also has a strong effect on the inversion results. Too large or too small values of the constants in the exponent would introduce a low frequency trend in the inverted traces making the calculated velocities either increase or decrease in time. This low frequency trend is eliminated when the low cut bandpass is applied to the inverted traces.

Chapter 7 - Future work

In Section 3.6, the P-S wave mode separation is applied in the p-t domain using the real part of the tapered complex filter coefficients derived in Section 3.3. However, the complex nature of the filter coefficients indicates that a phase shift must be applied to the data for slownesses where the imaginary parts of the filter coefficients are not equal to zero. This is not a problem for the pass-P case where the coefficients are tapered to zero for $|p| > 1/V_P$ and the imaginary parts of the filter coefficients end up being equal to zero. For the pass-S case, however, the imaginary parts of the filter coefficients are non-zero for $|p| > 1/V_P$. In this case, the modulus of the filter coefficients should be applied to the data at each slowness, and, a phase shift equal to the principal value of the argument of the filter coefficients at each slowness should also be applied. The above step could be easily achieved by taking a one-dimensional Fourier transform of the p-t decompositions in time, therefore taking the decompositions in the frequency-time (f-p) domain, applying the complex filter coefficients, stacking across the range of slownesses and inverse Fourier transform the stacked trace to yield the middle trace estimate of the local window being filtered. The complex multiplication of the filter coefficients and the complex traces in the f-p domain would perform the necessary amplitude and phase shift filtering discussed above. This implementation in the f-p domain was performed by Dillon et al. (1988). However, the P-S separation results obtained in this thesis do not display, at a glance, any phase deficiencies. The phase of the three events in the pass-S section of the synthetic data and of the field data are quite stable. From these observations, we can conclude that the use of the full complex filter coefficients, as compared to only using the real part of the filter coefficients, would have a minimal effect on the separation of S waves.

References

- Aki, K. and Richards, P. G., 1980, Quantitative seismology: Theory and methods, v. 1: W. H. Freeman and Co.
- Balch, A. H., Lee, M. W., Miller, J. J. and Ryder, R. T., 1982, The use of vertical seismic profiles in seismic investigations of the earth: *Geophys.*, 47, 6, 906-918.
- Cheadle, S. P., 1988, Applications of physical modeling and localized slant stacking to a seismic study of subsea permafrost: Ph.D. Thesis, The University of Calgary, Calgary, Alberta, Canada.
- Christie, P. A. F., Hughes, V.J., and Kennett, B. L. N., 1983, Velocity filtering of seismic reflection data: *First Break*, 1, 3, 9-24.
- Chung, W. Y., and Corrigan, D., 1985, Gathering mode-converted shear waves: A model study: *Soc. of Expl. Geophys. Ann. Mtg, Expanded Abstracts*, 602-604.
- Claerbout, J. F., 1985, *Imaging the earth's interior*: Blackwell Scientific Publications.
- Dankbaar, J. W. M. 1985, Separation of P- and S-Waves: *Geophys. Prosp.* 33, 970-986.
- Dankbaar, J. W. M., 1987, Vertical seismic profiling - Separation of P- and S-waves: *Geophys. Prosp.*, 35, 803-814.
- Dillon, P. B. and Thompson, R. C., 1984, Offset source VSP surveys and their image reconstruction: *Geophys. Prosp.*, 32, 5, 790-811.
- Dillon, P. B., Ahmed, H. and Roberts, T., 1988, Migration of mixed-mode VSP wavefields: *Geophys. Prosp.*, 36, 825-846.
- DiSiena, J. P., Gaiser, J. E. and Corrigan, D., 1984, Horizontal components and shear wave analysis of three-component data, in Toksöz, M .N. and Stewart, R. R., Eds., *Vertical seismic profiling, Part B: Advanced concepts*: Geophysical Press.

- Embree, P., Burg, J. P. and Backus, M. M., 1963, Wide-band velocity filtering - The pie slice process: *Geophys.*, 28, 948-974.
- Foster, D. J. and Gaiser, J. E., 1986, Elastic wave field decomposition of offset VSP data: *Soc. of Expl. Geophys. Ann. Mtg, Expanded Abstracts*, 563-565.
- Gal'perin, E. I., 1974, Vertical seismic profiling: *Society of Exploration Geophysicists*.
- Geis, W. T., Stewart, R. R., Jones, M. and Katapodis, P., 1989, An integrated P-SV study: Rolling Hills, Southern Alberta: submitted to *Geophysics*.
- Hardage, B. A., 1985, Vertical seismic profiling, Part A: Principles: *Geophysical Press*.
- Lee, M. W., 1987, Particle displacements of the wall of a borehole from incident plane waves: *Geophys.*, 52, 9, 1290-1296.
- Lindseth, R. O., 1979, Synthetic sonic logs - A process for stratigraphic interpretation: *Geophys.*, 44, 1, 3-26.
- Mammo, T., 1987, Wavefield separation methods in VSP: A review: *Bolletino di geofisica teorica ed applicata*, 29, 116, 275-307.
- Martin, M. A. and Davis, T. L., 1987, Shear wave birefringence: A new tool for evaluating fractured reservoirs: *The Leading Edge*, 6, 10, 22-28.
- McCormack, M. D., and Tatham, R. H., 1988, Shear wave exploration seismology: *Soc. of Expl. Geophys. continuing education course notes*.
- Moon, W., Carswell, A., Tang, R., and Dilliston, C., 1986, Radon transform wavefield separation for vertical seismic profiling data: *Geophys.*, 51, 4, 940-947.
- Newman, P., 1973, Divergence effects in a layered earth: *Geophys.*, 38, 481-488.
- Oristaglio, M. L., 1985, A guide to current uses of vertical seismic profiles: *Geophys.*, 50, 12, 2473-2479.

- Robinson, E. A., 1967, Multichannel time series analysis with digital computer programs: Holden-Day.
- Robinson, E. A. and Treitel, S., 1980, Geophysical signal analysis: Prentice-Hall Inc.
- Sheriff, R. E. and Geldart, L. P., 1983, Exploration seismology: Data processing and interpretation, v. 1: Cambridge University Press.
- Stewart, R. R., 1984, VSP interval velocities from travelttime inversion: *Geophys. Prosp.*, 32, 608-628.
- Stewart R. R., 1985, Median filtering: Review and a new f/k analogue design: *J. Can. Soc. Expl. Geophys.*, 21, 54-63.
- Stewart, R. R., 1988, VSP imaging using converted waves: 15th Ann. Nat. Mtg., Can Soc. Expl. Geophys., Abstracts, 29.
- Stewart, R. R., 1989a, Exploration seismic tomography: fundamentals: Society of Exploration Geophysicists.
- Stewart R. R., 1989b, VSPCCP map and AVO inversion for P-SV waves: Proc. Curr. Res. Symposium, Dept. Geol. Geophys., University of Calgary, 22.
- Stewart, R. R. and Labonté, S., 1989, VSPCCP map and AVO inversion for P-SV waves: in preparation.
- Toksöz, M .N. and Stewart, R. R., Eds., 1984, Vertical seismic profiling, Part B: Advanced concepts: Geophysical Press.
- Wyatt, K. D. and Wyatt, S. B., 1984, Determining subsurface structure using the vertical seismic profile, in Toksöz, M. N. and Stewart, R. R., Eds., Vertical seismic profiling, Part B: Advanced concepts: Geophysical Press.
- Yilmaz, O., 1987, Seismic Data Processing: Society of Exploration Geophysicists.